APPENDIX A: WESTERGAARD SOLUTIONS

APPENDIX A: WESTERGAARD SOLUTIONS

A.1 ACKNOWLEDGEMENT

Ioannides et al (1985a) published the results of a study, during which a thorough re-examination of the Westergaard solutions was conducted, using the tool of finite element analysis (Tabatabaie and Barenberg, 1980). They discussed the form, theoretical background, limitations and applicability of Westergaard's equations, and presented what are considered to be the most accurate versions of his formulae.

In view of the fact that these equations are also largely applicable to this thesis, they are reproduced here for clarity with recognition of the work of Ioannides et al (1985a).

A.2 INTRODUCTION

The pioneering analytical work of Harald Malcolm Westergaard (1888 -- 1950) has been at the heart of slab-on-grade pavement design since the 1920's. Every code of practice since then makes reference to the "Westergaard solutions". These solutions are only available for three particular loading conditions (interior, edge and corner) and assume a slab of infinite or semi-infinite dimensions (Ioannides et al, 1985a).

Westergaard equations have often been misquoted or misapplied. To remedy this situation a re-examination of these solutions using the finite element method has been conducted. The Winkler type subgrade assumed by Westergaard is modelled as a uniform, distributed subgrade through an equivalent mass formation.

A.3 INTERIOR LOADING

This is the case of a wheel load at a "considerable distance from the edges", with pressure "assumed to be uniformly distributed over the area of a small circle with radius a".

Maximum bending stress, σ_i

Ordinary theory $$BSIOT = \{[3P(1+\mu)]/2\pi h^2\}[\ln(2l/a) + 0{,}5 - \gamma] + BSI2OT \quad (1a)$$

Special theory $$BSIST = \{[3P(1+\mu)]/2\pi h^2\}[\ln(2l/b) + 0{,}5 - \gamma] + BSI2ST \quad (1b)$$

For square $$BSISQ = \{[3P(1+\mu)]/2\pi h^2\}[\ln(2l/c') + 0{,}5 - \gamma] + BSI2SQ \quad (1c)$$

Supplementary, σ_2 (ordinary theory) $$BSI2OT = \{[3P(1+\mu)]/64h^2\}[(a/l)^2] \quad (1d)$$

Supplementary, σ_2 (special theory) $$BSI2ST = \{[3P(1+\mu)]/64h^2\}[(b/l)^2] \quad (1e)$$

Supplementary, σ_2 (for square) $$BSI2SQ = \{[3P(1+\mu)]/64h^2\}[(c'/l)^2] \quad (1f)$$

Maximum deflection, δ_i

Circle $$DEFIC = (P/8kl^2)\{1 + (1/2\pi)[\ln(a/2l) + \gamma - 5/4](a/l)^2\} \quad (1g)$$

Where:

P	=	total applied load;
E	=	slab Young's modulus;
μ	=	slab Poisson's ratio;
h	=	slab thickness;
k	=	modulus of subgrade reaction;
a	=	radius of circular load;
c	=	side length of square load;

$l^4 = \{Eh^3/[12(1-\mu^2)k]\}$ which is radius of relative stiffness;

$b = [(1{,}6a^2 + h^2)^{1/2}] - 0{,}675h$ if a < 1,724h

= a if a > 1,724h;

$c' = (e^{\pi/4 - 1}/2^{1/2})c$; and

γ = Euler's constant (= 0,577 215 664 90).

Equation 1b employs Westergaard's "special theory" in which radius b replaces the true radius, a, of the loaded area. This was introduced to account for the effect of shear stresses in the vicinity of the load, which was neglected in the "ordinary theory" of medium-thick plates.

To obtain the interior stress in the case of a square loaded area, radius a is replaced in equation 1c by a constant c', related to the length of the side of the square, c, as follows:

$$c' = \left(e^{\pi/4-1}/2^{1/2}\right)c = 0{,}573804c$$

Westergaard stress values (Equation 1a) agree with finite element results for a loaded area whose side length, c (if square), is about 0,2 times the radius of the relative stiffness, *l*; if the load is circular, its radius, a, must be about 0,1*l*. As (c/*l*) or (a/*l*) increase, finite element stresses become progressively higher than Westergaard's.

A.4 EDGE LOADING

Edge loading is the case in which "the wheel load is at the edge, but at a considerable distance from any corner". The pressure is assumed to be distributed uniformly over the area of a small semi-circle with the centre at the edge".

Maximum bending stress, σ_e

Ordinary theory (semicircle)
$$BSEWOT = 0{,}529(1+0{,}54\mu)(P/h^2)[\log_{10}(Eh^3/ka_2^4) - 0{,}71] \quad (2a)$$

Special theory (semicircle)
$$BSEWST = 0{,}529(1+0{,}54\mu)(P/h^2)[\log_{10}(Eh^3/kb_2^4) - 0{,}71] \quad (2b)$$

"New" formula (circle)
$$BSEIC = [3(1+\mu)P/\pi(3+\mu)h^2]x \{\ln(Eh^3/100ka^4) + 1{,}84 - 4\mu/3 + [(1-\mu)/2] + 1{,}18(1+2\mu)(a/l)\} \quad (2c)$$

"New" formula (semi-circle)
$$BSEIS = [3(1+\mu)P/\pi(3+\mu)h^2]x \{\ln(Eh^3/100ka_2^4) + 3{,}84 - 4\mu/3 + 0{,}5(1+2\mu)(a_2/l)\} \quad (2d)$$

Simplified "new" formula (semi-circle)
$$BSELS = (-6P/h^2)(1+0{,}5\mu)[0{,}489\log_{10}(a_2/l) - 0{,}091 - 0.027(a_2/l)] \quad (2e)$$

Simplified "new" formula (circle)
$$BSELC = (-6P/h^2)(1+0{,}5\mu)[0{,}489\log_{10}(a/l) - 0{,}012 - 0.063(a/l)] \quad (2f)$$

Maximum deflection, δ_e

Original formula $DEFEW = (1/6^{1/2})(1+0,4\mu)(P/kl^2)$ (2g)

"New" formula $DEFEIC = (\{P[(2+1,2\mu)^{1/2}]\}/[(Eh^3k)^{1/2}])[1-(0,76+0,4\mu)(a/l)]$ (2h)
(circle)

"New" formula $DEFEIS = (\{P[(2+1,2\mu)^{1/2}]\}/[(Eh^3k)^{1/2}])[1-(0,323+0,17\mu)(a_2/l)]$ (2i)
(semi-circle)

Simplified "new" $DEFELS = (1/6^{1/2})(1+0,4\mu)(P/kl^2)[1-0,323(1+0,5\mu)(a_2/l)]$ (2j)
formula (semi-circle)

Simplified "new" $DEFELC = (1/6^{1/2})(1+0,4\mu)(P/kl^2)[1-0,76(1+0,5\mu)(a/l)]$ (2k)
formula (circle)

Where:

a_2 = radius of semi-circle

b_2 = $[(1,6a_2+h^2)^{1/2}]-0,675h$ if $a_2 < 1,724h$

= a_2 if $a_2 > 1,724h$ and other symbols are as defined for Equations 1.

Edge stresses calculated from the "new" formula are considerably different from those computed using the original formula. The "new" formulas typically lead to stresses 55% higher and deflections 8% lower than the values obtained using the original formulas. The semi-circular load is more severe than the circular load, because the centre of gravity of the circle is further toward the interior of the slab than is that of the semi-circle.

A.5 CORNER LOADING

Of the three fundamental cases of loading investigated by Westergaard, corner loading is undoubtedly the most obscure and debatable.

Deflection

$\delta_c = (P/kl^2)[1,1-0,88(a_1/l)]$ *Westergaard, 1926* (3a)

Stress

$$\delta_c = (3P/h^2) \qquad \textit{Goldbeck, Older} \qquad (3b)$$

$$\delta_c = (3P/h^2)[1-(a_1/l)^{0,6}] \qquad \textit{Westergaard} \qquad (3c)$$

$$\delta_c = (3P/h^2)[1-(a/l)^{0,6}] \qquad \textit{Bradbury} \qquad (3d)$$

$$\delta_c = (3P/h^2)[1-(a_1/l)^{1,2}] \qquad \textit{Kelly, Teller and Sutherland} \qquad (3e)$$

$$\delta_c = (3{,}2P/h^2)[1-(a_1/l)] \qquad \textit{Spangler} \qquad (3f)$$

$$\delta c = (4{,}2P/h2)(1-\{[(a/l)^{1/2}]/[0{,}925+0{,}22(a/l)]\}) \qquad \textit{Pickett} \qquad (3g)$$

Distance to point of maximum stress along corner bisector

$$X_1 = 2[(a_1/l)^{1/2}] \qquad \textit{Westergaard, 1926} \qquad (3h)$$

Where:

a = radius of circular load tangent to both edges at corner and

a_l = distance to point of action resultant along corner angle bisector

= $(2^{1/2})$a. (See Equations 1 for other symbols)

A.5.1 EQUATIONS FOR THE CORNER LOADING CONDITION BASED ON THE FINITE ELEMENT METHOD

A straight line may be used to describe *corner deflections,* δ_c. This line has the following equation:

$$\delta_c = (P/kl^2)[1{,}205 - 0{,}69(c/l)] \qquad (4)$$

Where c is the side length of square loaded area. The finite element results obtained are typically 10% higher than those predicted by Westergaard.

The ILLI-SLAB maximum *corner stresses,* σ_C, curve fitting suggested the following equation:

$$\sigma_C = (3P/h^2)[1{,}0-(c/l)^{0,72}] \qquad (5)$$

A.5.2 LOCATION OF MAXIMUM STRESS

The curve fitting equation obtained by extrapolation of the results from a selected number of ILLI-SLAB runs for the location of the *maximum stress,* X_l, is as follows:

$$X_1 = 1{,}80c^{0{,}32}l^{0{,}59} \qquad (6)$$

This equation indicates that the influence of the radius of relative stiffness, l, is much greater than that of the size of the loaded area.

A.5.3 SLAB SIZE REQUIREMENTS FOR CORNER LOADING WESTERGAARD RESPONSES

Ioannides, Thompson and Barenberg (1985) determined the slab size requirements for Westergaard responses based on the finite element method, as summarised in Table A.1.

Table A.1: Slab size requirements for Westergaard responses based on the finite element method

Load Placement	(*L*/*l*) Values for	
	Maximum Deflection	Maximum Bending Stress
Interior	8,0	3,5
Edge	8,0	5,0
Corner	5,0	4,0

Note: L = least slab dimension and *l* = radius of relative stiffness

APPENDIX B: WESTERGAARD-TYPE SOLUTION FOR EDGE LOAD TRANSFER PROBLEM

APPENDIX B: WESTERGAARD-TYPE SOLUTION FOR EDGE LOAD TRANSFER PROBLEM

B.1 ACKNOWLEDGEMENT

During an examination of the archives of the U.S. Army Engineer Waterways Experiment Station, Ioannides and Hammons (1996) discovered a report that Westergaard submitted to the Corps of Engineers in 1949. This report contained a detailed examination of the edge load transfer problem, prepared by Westergaard's associate, M.S. Skarlatos. The result of an investigation that sought to extend and refine the edge load transfer solution by Skarlatos, using modern computational tools were presented by Ioannides and Hammons in 1996. They followed the same approach as Skarlatos and Westergaard, by deriving closed-form equations for the maximum deflection and bending stress occurring on the unloaded side of an edge capable of load transfer.

The general solution for edge load transfer formulas is reproduced here for clarity with recognition to Ioannides and Hammons (1996). To quote the authors: "the formulas derived in this study constitute a complete solution of the edge load transfer problem, recognised over the years as a critical consideration in the PCC pavement design."

B.2 GENERAL SOLUTION FOR EDGE LOAD TRANSFER

B.2.1 SKARLATOS FORMULAS

The deflection at the origin of the coordinates (0,0) on the unloaded side of a joint due to a point load, P, applied at (x, y) is given by:

$$\Delta_U^* = \frac{\Delta_U k l^2}{P} = \frac{4}{\pi}\int_0^\infty \frac{\gamma^2}{F(4\gamma + F/f)} \times \cos\frac{\alpha x}{l}\left(\cos\frac{\beta y}{l} + \kappa \sin\frac{\beta y}{l}\right) e^{-\gamma y/l} d\alpha \tag{B.1}$$

Where:

$$\kappa = (1-\mu)\alpha^2 \tag{B.2}$$

$$F = 1 + 4\kappa\gamma^2 - \kappa^2 \tag{B.3}$$

$$\beta = \sqrt{\frac{1}{2}\left(\sqrt{1+\alpha^4} - \alpha^2\right)} = \frac{1}{2\gamma} \tag{B.4}$$

$$\gamma = \sqrt{\frac{1}{2}\left(\sqrt{1+\alpha^4} + \alpha^2\right)} = \sqrt{\alpha^2 + \beta^2} \tag{B.5}$$

$$f = \frac{q_0}{kl} = \frac{AGG}{kl} \tag{B.6}$$

Equation B.6 defines a dimensionless joint stiffness, f, in terms of the slab-subgrade radius of relative stiffness, l; the subgrade modulus, k; and parameter q_0, referred to as spring constant AGG. Parameter q_0 has dimensions of FL^{-2} and represents the force transferred across a unit length of joint per unit differential deflection across the joint. The slab Poisson's ratio is denoted by μ. The x-axis runs along the joint, while the y-axis is perpendicular to the joint and is positive in the direction of the loaded slab. Accordingly, determination of the dimensionless deflection, Δ_U*, for a loaded area of finite size involves a triple integral in dx, dy and $d\alpha$, the latter being a dummy integration variable (see Figure B.1).

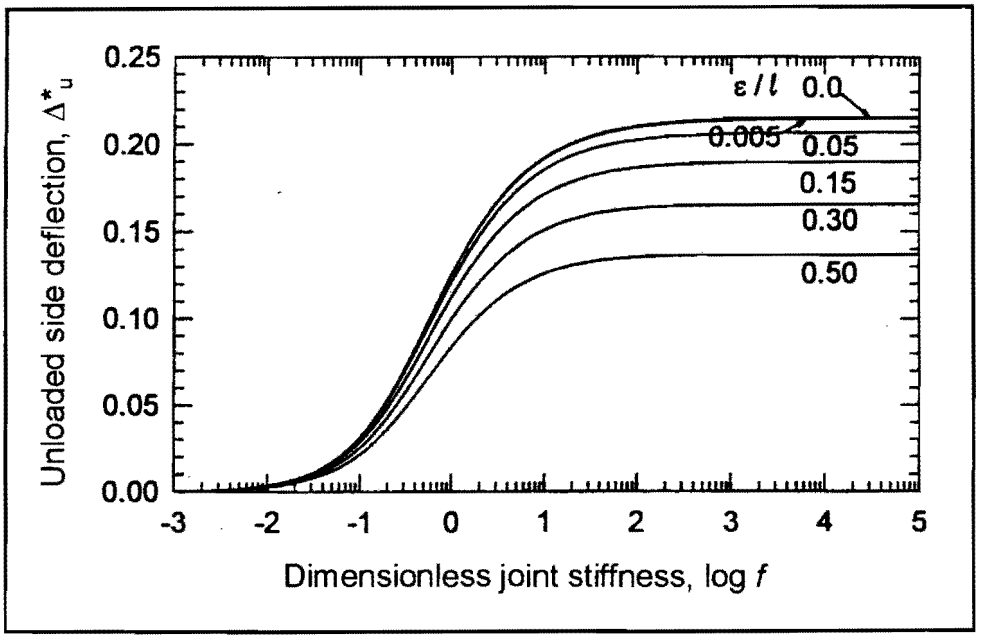

Figure B.1: Variation of maximum dimensionless deflection for unloaded side with dimensionless joint stiffness and dimensionless load size ratio

Similarly, according to Skarlatos, the bending stress at the origin of the coordinates (0,0) on the unloaded side of a joint due to a point load, P, applied at x, y is given by:

$$\sigma_{tl}^{*} = \frac{\sigma_{tl} h^2}{P} = \frac{24(1-\mu^2)}{\pi} \int_0^{\infty} \frac{\alpha^2 \gamma^2}{F(4\gamma + F/f)} \cos\frac{\alpha x}{l} \left(\cos\frac{\beta y}{l} + \kappa \sin\frac{\beta y}{l} \right) e^{-\gamma y/l} d\alpha \tag{B.7}$$

Here, h denotes the thickness of the slab. Proceeding as outlined above for the unloaded deflection, and setting the slab Poisson's ratio, μ, to 0,15, the curves in Figure B.2 were obtained.

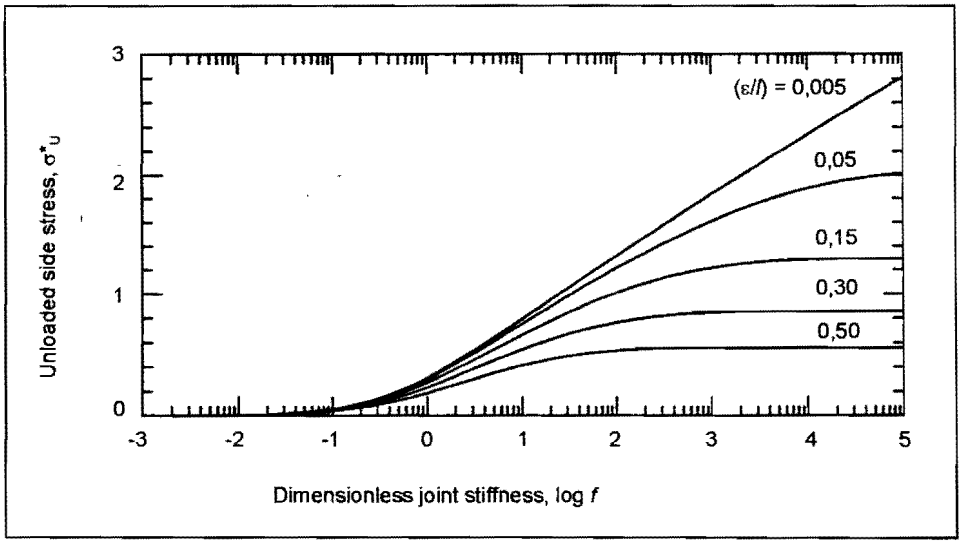

Figure B.2: Variation of maximum dimensionless bending stress for unloaded side with dimensionless joint stiffness and dimensionless load size ratio

For a slab resting on a dense liquid foundation and equipped with a pure-shear load transfer mechanism, the corresponding responses on the loaded side can be obtained as follows:

$$\Delta_L = \Delta_f - \Delta_U \tag{B.8}$$

and

$$\sigma_L = \sigma_f - \sigma_U \tag{B.9}$$

Where Δ_f and σ_f are the maximum responses of a free edge. Equations for the latter integral form were given by Westergaard (1947), as follows:

$$\Delta_f^* = \frac{\Delta_f k l^2}{P} = \frac{2}{\pi}\int_0^\infty \frac{\gamma}{F}\cos\frac{\alpha x}{l}\left(\cos\frac{\beta y}{l} + \kappa \sin\frac{\beta y}{l}\right)e^{-\gamma y/l}d\alpha \tag{B.10}$$

and

$$\sigma_f^* = \frac{\sigma_f h^2}{P} = \frac{12(1-\mu^2)}{\pi}\int_0^\infty \frac{\alpha^2\gamma}{F}\cos\frac{\alpha x}{l}\left(\cos\frac{\beta y}{l} + \kappa\sin\frac{\beta y}{l}\right)e^{-\gamma y/l}d\alpha \qquad \text{(B.11)}$$

In this case, the y-axis is perpendicular to the joint and is positive in the direction of the loaded slab. The results are shown in Figures B.3 and B.4, where they are compared to Westergaard's (1948) for a circular load, radius *a*. Such direct application of Westergaard's circular load formulas can lead to errors of up to 8 percent for the loaded area sizes considered.

B.2.2 INTERPOLATION FORMULAS

B.2.2.1 Free edge deflection

The Westergaard formula for the deflection at the origin of coordinates due to a distributed load placed tangentially to a free edge with its centroid located at a distance $\bar{y}$ from the free edge:

$$\Delta_f^* = \frac{\Delta_f k l^2}{P} = \left[B_3 - B_4\left(\frac{\bar{y}}{l}\right)\right] \qquad \text{(B.12)}$$

In this expression B_3 and B_4 are dimensionless constants dependent only on the value of the slab Poisson's ratio, μ. For a circular load, radius *a* simply replaces centroidal distance $\bar{y}$ (and by ε for a square load). Equation B.12 represents the Taylor series for the complete solution, with only the linear term retained. By considering the deflection and slope at the origin due to a point load at the same location, and setting μ = 0,15, Westergaard evaluated B_3 and B_4 as 0,4314 and 0,3510, respectively. For other values of μ, he provided the following interpolation formulas for the two constants:

$$B_3 = \frac{\sqrt{2+1{,}2\mu}}{\sqrt{12(1-\mu^2)}} \qquad \text{(B.13)}$$

$$\frac{B_4}{B_3} = 0{,}76 + 0{,}4\mu \qquad \text{(B.14)}$$

A better approximation to the complete solution for a square load may be obtained by adding a quadratic term to Equation B.12:

$$\Delta_f^* = \frac{\Delta_f k l^2}{P} = \left[B_3 - B_4\left(\frac{\varepsilon}{l}\right) + \frac{1}{2}B_6\left(\frac{\varepsilon}{l}\right)^2\right] \qquad \text{(B.15)}$$

With μ = 0,15, B_6 should be set to 0,1305.

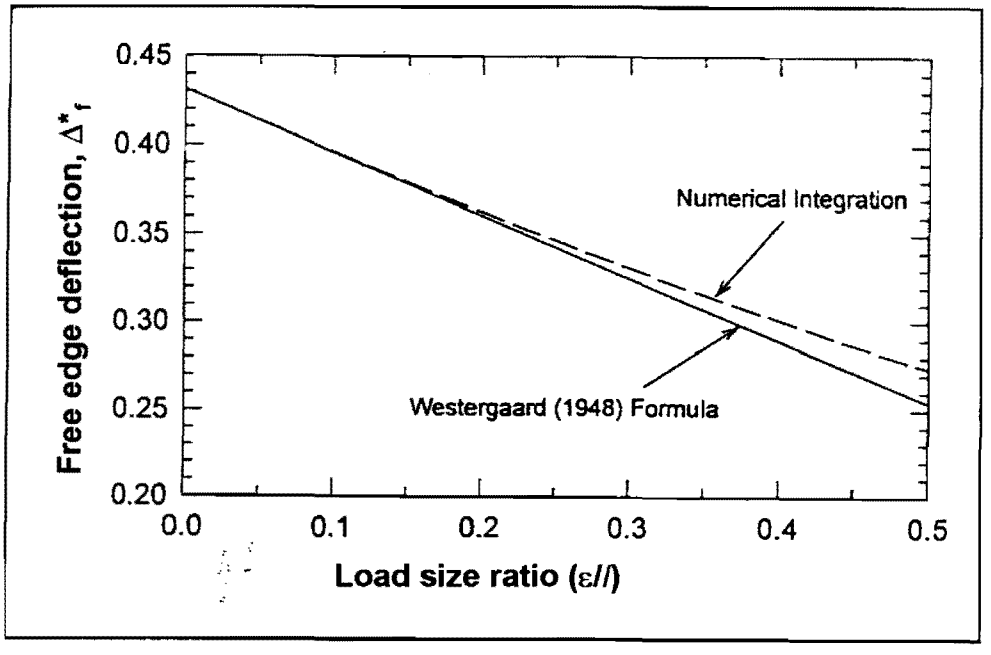

Figure B.3: Variation of maximum dimensionless deflection for free edge with dimensionless load size ratio

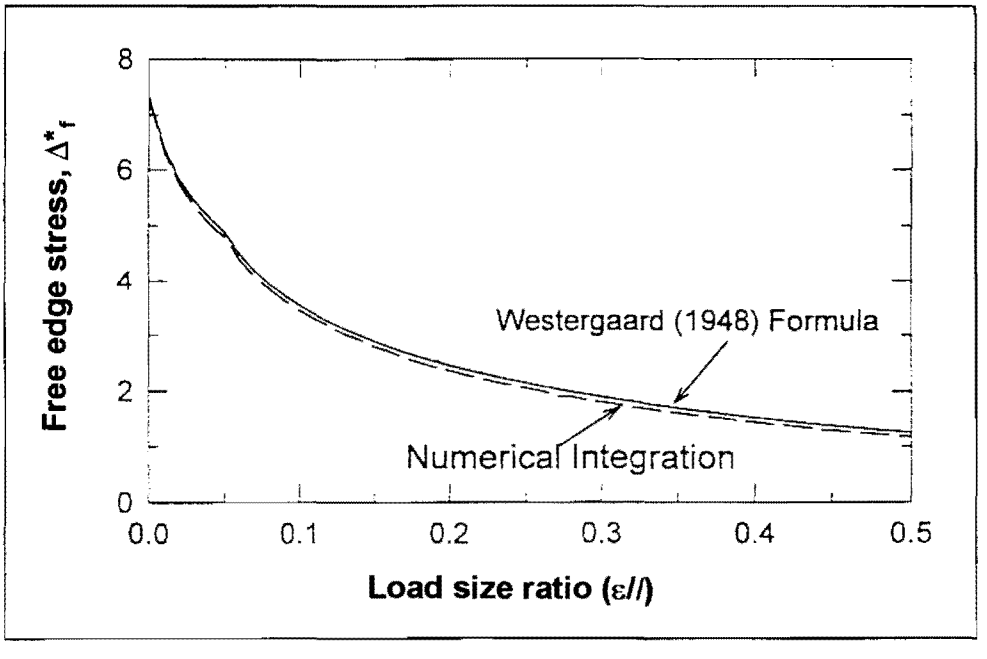

Figure B.4: Variation of maximum dimensionless bending stress for free edge with dimensionless load size ratio

B.2.2.2 Free edge bending stress

Because of a singularity in Equation B.11, Westergaard split into two parts the bending stress arising at the origin of coordinates under the action of a tangential distributed load area:

$$\sigma_f = \overline{\sigma} + \sigma_c \tag{B.16}$$

Westergaard wrote the first term in Equation B.16 as:

$$\overline{\sigma}^* = \frac{\overline{\sigma} h^2}{P} = \frac{12(1+\mu)}{\pi(3+\mu)}\left[0{,}1159 + K + \frac{1-\mu}{4}S\right] \tag{B.17}$$

For a circular load, radius a:

$$K = -\log_e\left(\frac{a}{l}\right) \tag{B.18}$$

and

$$S = \frac{1}{2} \tag{B.19}$$

As for the second term in equation B.16, Westergaard again expressed it in terms of a Taylor series, retaining only the linear term:

$$\sigma_c^* = \frac{\sigma_c h^2}{P} = \frac{12((1+\mu)}{\pi(3+\mu)}\left[\frac{3-\mu}{4} - B_1 + B_2\left(\frac{a}{l}\right)\right] \tag{B.20}$$

For $\mu = 0{,}15$, Westergaard obtained $B_1 = 0{,}9544$ and $B2 = 0{,}3822$. In adapting this solution for a square load, Westergaard's first term was retained (Equations B.17, B.18, and B.19, with a replaced by ε), but quadratic and cubic terms were added to Equation B.20.

$$\sigma_c^* = \frac{\sigma_c h^2}{P} = \frac{12((1+\mu)}{\pi(3+\mu)}\left[\frac{3-\mu}{4} - B_1 + B_2\left(\frac{a}{l}\right) + \frac{1}{2}B_9\left(\frac{\varepsilon}{l}\right)^2 + \frac{1}{6}B_{10}\left(\frac{\varepsilon}{l}\right)^3\right] \tag{B.21}$$

For $\mu = 0{,}15$, $B_9 = -4{,}225$ and $B_{10} = 24{,}12$.

B.2.2.3 Unloaded side deflection

The deflection of the unloaded side is as follows:

$$\Delta_U^* = \frac{\Delta_U k l^2}{P} = \left[B_3' - B_4' \left(\frac{\varepsilon}{l} \right) \right] \tag{B.22}$$

Where

$$B_3' = \frac{4}{\pi} \int_0^\infty \frac{\gamma^2}{F(4\gamma + F/f)} d\alpha \tag{B.23}$$

and

$$B_4' = \frac{2}{\pi} \int_0^\infty \frac{\gamma^2 (2\gamma^2 - \kappa))}{F(4\gamma + F/f)} d\alpha \tag{B.24}$$

The following regression equations were derived for the B coefficients, retaining the functional forms first suggested by Skarlatos:

$$B_3' = \frac{f - 0{,}6367 \log(1+f)}{4{,}6516 f + 1{,}8210} \tag{B.25}$$

and

$$\frac{B_4'}{B_3'} = 0{,}6984 + 0{,}0441 \log(1+f) - 0{,}0065 f^{0{,}24} \tag{B.26}$$

Substituting Equations B.25 and B.26 into Equation B.22 and rounding off the regression coefficient leads to:

$$\Delta_U^* = \frac{\Delta_U k l^2}{P} = 0{,}215 \left[\frac{f - 0{,}6 \log(1+f)}{f + 0{,}4} \right] * \left\{ 1 - 0{,}7 \left(\frac{\varepsilon}{l} \right) \left[1 + 0{,}06 \log(1+f) - 0{,}01 f^{0{,}2} \right] \right\} \tag{B.27}$$

The predictive ability of Equation B.27 deteriorates slightly as ε/l and f increase. For $\varepsilon/l = 0{,}5$, the ratio of the (predictive/exact) values of Δ_U ranges between 0,91 and 0,99 for log f values between –3 and 5. Equation B.27 affords approximately the same precision as direct application of the free edge deflection equation given by Westergaard. By analogy to Equation B.15, a quadratic term is added to Equation B.22 as follows:

$$\Delta_U^* = \frac{\Delta_U k l^2}{P} = \left[B_3' - B_4' \left(\frac{\varepsilon}{l} \right) + \frac{1}{2} B_6' \left(\frac{\varepsilon}{l} \right)^2 \right] \tag{B.28}$$

Where:

$$B_6' = \frac{1}{\pi} \int_0^\infty \frac{-1 + 4\gamma^4 - 4\gamma^2 \kappa}{F(4\gamma + F/f)} d\alpha \tag{B.29}$$

The integral in Equation B.29 was evaluated for $\mu = 0{,}15$ and for $\log f$ ranging between –3 and 5. Results were fitted with a regression algorithm. The choice of algorithm was guided by the desire to keep the number of regression coefficients to a minimum. The resulting relationship was:

$$\begin{aligned} B_6' = {} & (0{,}01945 + 0{,}009348 \log f - 0{,}002093 \log^2 f - 0{,}001086 \log^3 f) \\ & \div (1 - 0{,}1474 \log f + 0{,}2666 \log^2 f - 0{,}02004 \log^3 f) \end{aligned} \tag{B.30}$$

The functional form in Equation B.30 was then added to Equation B.27 as suggested by Equation B.28. In this manner the following simplified expression was obtained:

$$\Delta_U^* = \frac{1}{2} [0{,}015 + 0{,}005 \log f] \left(\frac{\varepsilon}{l} \right)^2 \tag{B.31}$$

B.2.2.4 Unloaded side bending stress

Retaining only the linear term in the Taylor series expansion for the unloaded side bending stress results in:

$$\sigma_U^* = \frac{\sigma_U h^2}{P} = \frac{24(1-\mu^2)}{\pi} \left[B_1' - B_2' \left(\frac{\varepsilon}{l} \right) \right] \tag{B.32}$$

Where:

$$B_1' = \int_0^\infty \frac{\alpha^2 \gamma^2}{F\left(4\gamma + \frac{F}{f}\right)} d\alpha \tag{B.33}$$

and

$$B_2' = \frac{1}{2} \int_0^\infty \frac{\alpha^2 \gamma (2\gamma^2 - \kappa)}{F\left(4\gamma + \frac{F}{f}\right)} d\alpha \tag{B.34}$$

The integrals in Equations B.33 and B.34 were evaluated for $\mu = 0,15$ and for values of $\log f$ ranging between –3 and 5. The following regression equations for the B coefficients in Equation B.32 were derived, retaining the functional forms first suggested by Skarlatos:

$$B_1' = 0,03316 + 0,07205\log(1+f) + \frac{0,00773\sqrt{f} - 0,03360}{f+1} \tag{B.35}$$

and

$$\frac{B_2'}{B_1'} = \left[0,08281f + 0,4790 - \frac{0,000149}{f}\right]^{\frac{1}{4,209}} \tag{B.36}$$

Substituting Equations B.35 and B.36 into Equation B.32 leads (upon rounding off the regression coefficients) to:

$$\sigma_U^* = \frac{\sigma_U h^2}{P} = 0,54\left[0,42 + \log(1+f) + 0,1\frac{\sqrt{f} - 4,2}{f+1}\right] * \left[1 - 0,54\left(\frac{\varepsilon}{l}\right)^{\sqrt[4,1]{f+5,0}}\right] \tag{B.37}$$

The predictive ability of Equation B.37 deteriorates rapidly as f increases to over 10, especially for $(\varepsilon/l) > 0,3$. To address this limitation, a second-order term in the Taylor expansion for σ_U^* was derived in the study, expanding Equation B.32 to:

$$\sigma_U^* = \frac{\sigma_U h^2}{P} = \frac{24(1-\mu^2)}{\pi}\left[B_1' - B_2'\left(\frac{\varepsilon}{l}\right) - \frac{1}{2}B_9'\left(\frac{\varepsilon}{l}\right)^2\right] \tag{B.38}$$

Where:

$$B_9' = \int_0^{\infty} \frac{\alpha^2\gamma^2(\gamma^2 - \beta^2 - \kappa)}{F\left(4\gamma + \frac{F}{f}\right)} d\alpha \tag{B.39}$$

The integral in Equation B.39 was evaluated for the case $\mu = 0,15$ and for values of $\log f$ ranging from –3 to 5. The following regression equation was derived for coefficient B_9':

$$B_9' = \log^{-1}[0,6671\log f - 1,6570] \tag{B.40}$$

Proceeding as outlined above for the unloaded side deflection, the following simplified equation is derived for the quadratic bending stress increment $\sigma_U^{*'}$ to be added to Equation B.37:

$$\sigma_U^{*'} = 7,5\log^{-1}[0,74\log f - 1,94] * \frac{1}{2}\left(\frac{\varepsilon}{l}\right)^2 \tag{B.41}$$

It is recommended that the increment in Equation B.41 be used for $f > 10$, subject to the constraint that the resulting unloaded side stress not exceed half the corresponding free edge stress for the case considered.

B.2.3 LOAD TRANSFER EFFICIENCY

Figures B.5 and B.6 illustrate the load transfer efficiencies with respect to deflection, LTE_{Δ}, and with respect to stress, LTE_{σ}, with the dimensionless joint stiffness, f or (AGG/kl), and the dimensionless loaded area size, ε/l The load transfer definitions for deflection and stress, respectively, are:

$$LTE_{\Delta} = \frac{\Delta_U}{\Delta_L} \tag{B.42}$$

and

$$LTE_{\sigma} = \frac{\sigma_U}{\sigma_L} \tag{B.43}$$

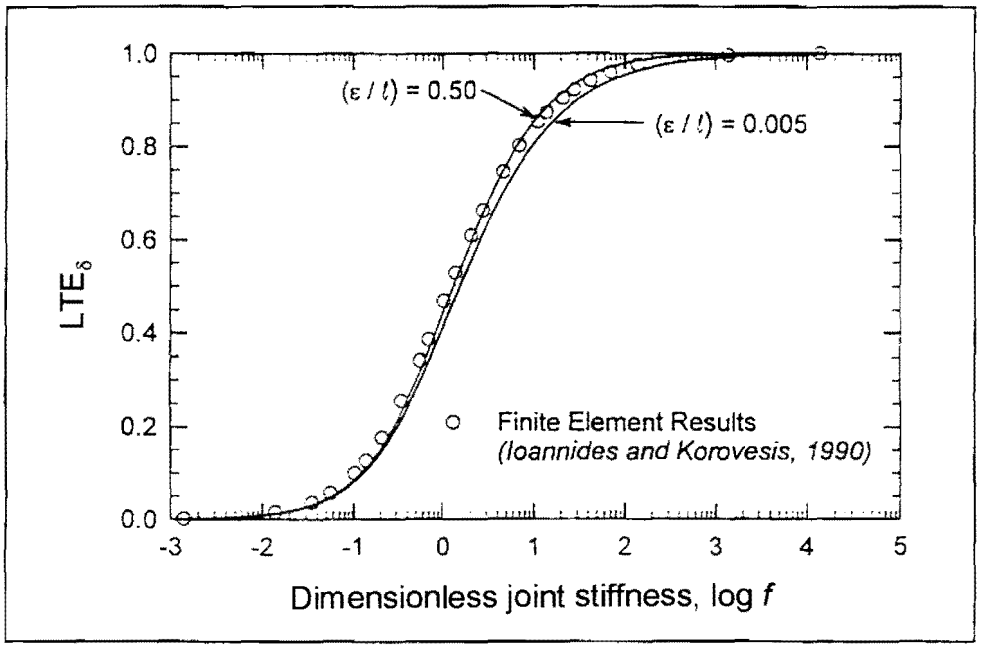

Figure B.5: Variation of load transfer efficiency with respect to deflection with dimensionless joint stiffness and dimensionless load size ratio

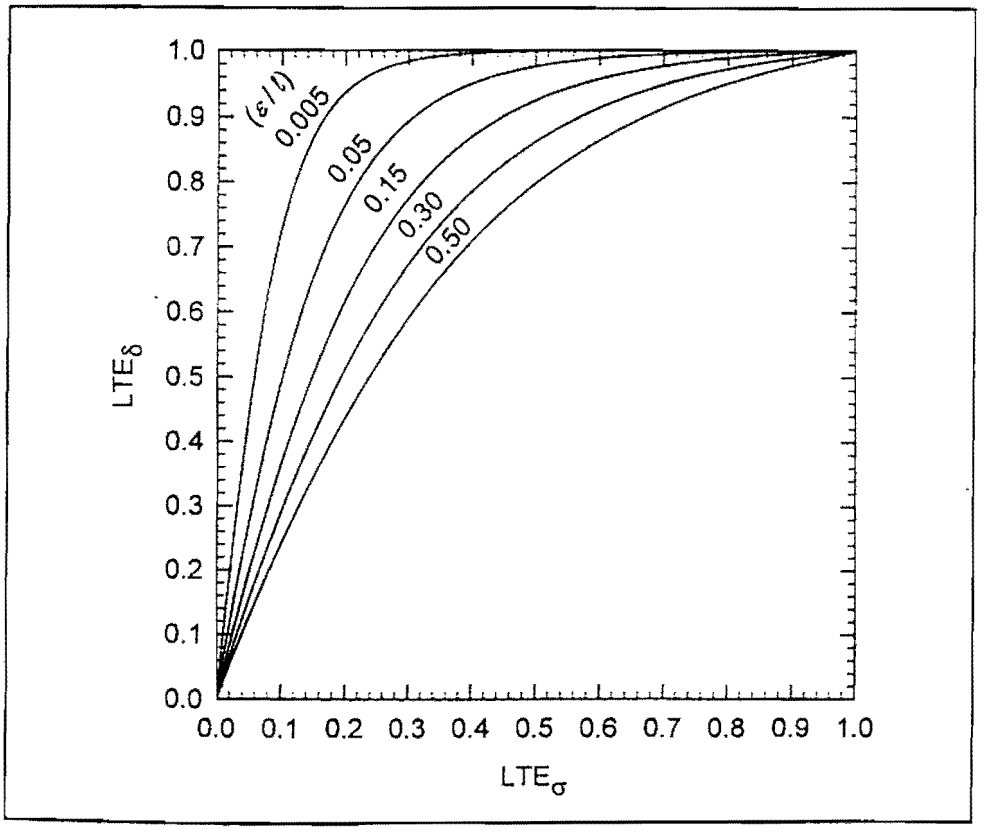

Figure B.6: Relationship between load transfer efficiencies with respect to deflection and stress for various dimensionless load size ratios

Figures B.5 and B.6 confirm the observations that LTE_Δ is rather insensitive to ε/l, where as the sensitivity of the relationship between these two efficiencies to ε/l is quite pronounced. The improvement achieved using the solution by Skarlatos and modern computational tools is clearly discernible in Figure B.7, in which the newly derived LTE_Δ versus LTE_σ relationships for two extreme load size ratios are compared with earlier finite element results.

Non-linear regression was used to develop an expression for LTE_Δ as a function of the dimensionless joint stiffness, f, and of the dimensionless load size ratio, ε/l. Assuming a linear variation with ε/l, the resulting relationship was as follows:

$$LTE_\Delta = \frac{1}{1+\log^{-1}\left[\dfrac{0{,}214-0{,}183\left(\dfrac{\varepsilon}{l}\right)-\log f}{1{,}180}\right]} \qquad \text{(B.44)}$$

(R^2 = 1,0)

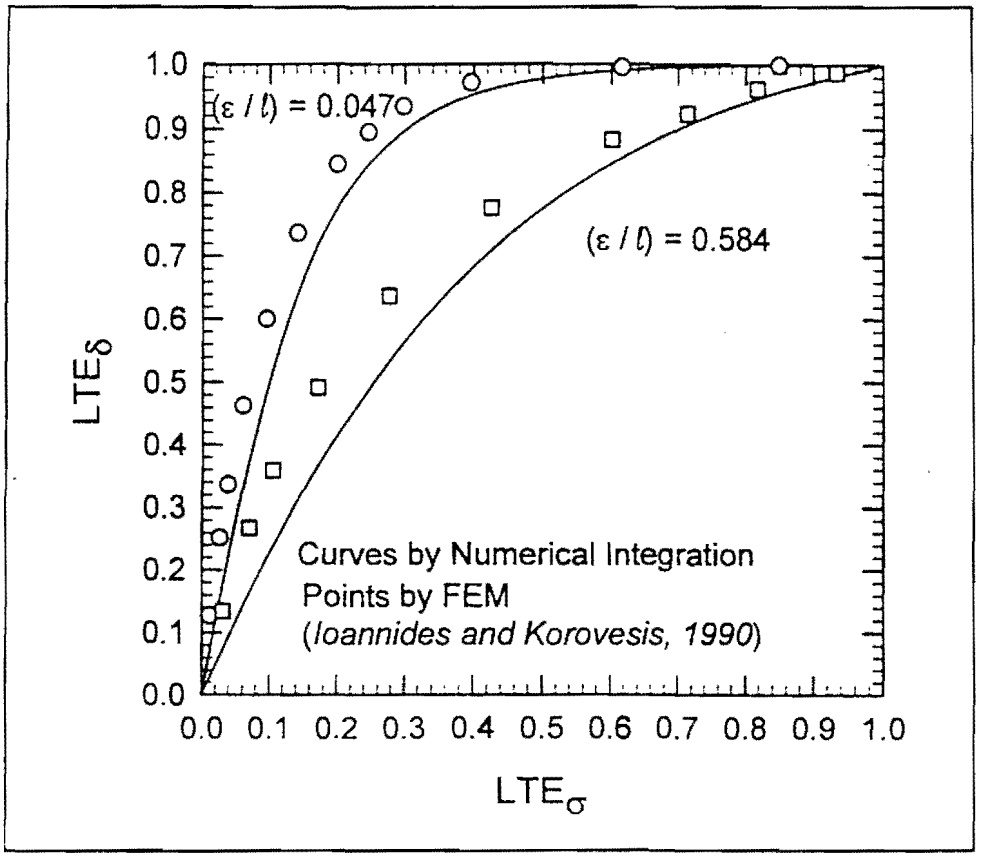

Figure B.7: Comparison of newly derived solution with earlier finite element results

Likewise, non-linear regression was used to develop an expression for LTE_Δ as a function of LTE_σ and of ε/l. The regression formula obtained in this fashion was:

$$LTE_\Delta = \frac{\left[1206\left(\frac{\varepsilon}{l}\right)+377\right]LTE_\sigma^2 - 393\left(\frac{\varepsilon}{l}\right)LTE_\sigma^3}{1+689\left(\frac{\varepsilon}{l}\right)LTE_\sigma + \left[370-154\left(\frac{\varepsilon}{l}\right)\right]LTE_\sigma^2} \qquad \text{(B.45)}$$

($R^2 = 0{,}999$)

APPENDIX C: DOWEL MODELLING

TABLE OF CONTENTS

LIST OF FIGURES

LIST OF SYMBOLS

a, b, c	Constants for a particular value of f_r ($0{,}05 < f_r < 0{,}065$)
β	Relative stiffness of dowel/concrete system
c	Dowel bar radius
d	Diameter of dowel bar
Δ_S	Shear displacement across crack
Δ_X	Local bond slip
η_{shear}	Shear load transfer efficiency (range 0 – 1)
E_d	Modulus of elasticity of dowel
E_s	Modulus of elasticity of steel
$\varepsilon_b, \varepsilon_t$	Strain at bottom and top of dowel
F_d	Dowel force
F_{du}	Ultimate dowel shear force
f_{cu}	Ultimate compressive strength of concrete cube
f_y	Yield stress of reinforcing steel
G_f	Specific gravity of foundation

I_d	Moment of inertia of the dowel
k	Modulus of subgrade reaction
K	Modulus of dowel support
K_i	Initial shear stiffness of dowel bar
M_P	Plastic moment capacity of dowel bar
M_z	Bending moment
P	Total load applied
σ_b	Bearing stress of concrete
σ_d	Maximum stress in dowel bar
τ_x	Local bond stress
V_{dowel}	Shear force transferred across the gap through the dowel bar
V_{slab}	Shear force transferred through a continuous slab

APPENDIX C: DOWEL MODELLING

C.1 DOWEL MODELLING

C.1.1 INTRODUCTION

The essence of the literature review on dowel modelling has been presented in Chapter 2. However, in order not to cloud the issue, some of the analytical and finite element (FE) studies that have merit are summarised here.

C.1.2 ANALYTICAL DOWEL MODELLLING

C.1.2.1 Millard and Johnson (1984)

In an attempt to study the internal mechanisms of shear transfer and dowel action across a single crack to enable more accurate modelling of shear stiffness, Millard and Johnson (1984) *devised tests of a new type* to examine independently the aggregate interlock (see paragraph 2.5) and dowel action effects in reinforced concrete.

Aggregate interlock action was eliminated from the *dowel action* specimens (2 / 300 mm high x 225 mm wide x 100 mm thick rectangular concrete prisms) by the construction of a smooth, low-friction crack passing through the centre of the specimen. This was achieved by casting each specimen in two stages. The first half was cast against a flat steel plate positioned across the centre of the mould. After 24 hours this plate was removed and the exposed face covered with two layers of thin polythene sheeting. The remainder of the specimen was then cast against this sheeting. Each reinforcing bar cast into the dowel action specimens was fitted with two strain gauges at the location of the crack to measure the axial and flexural strains.

In theoretical dowel action models, it has been suggested that there are three mechanisms of shear transfer through dowel action, namely: direct shear, kinking, and flexure of the dowel bars. If the concrete supporting each bar were considered to be rigid, the first two mechanisms would predominate, however, significant deformation of the concrete does occur, so that flexure of the dowel bar within the concrete is the principal action. This has been modelled by considering the dowel bar as a beam on an elastic foundation. The dowel force, F_d is given by:

$$F_d = 0{,}166\Delta_s G_f^{0{,}75} d^{1{,}75} E_s^{0{,}25} \qquad \text{(C.1)}$$

Where the constant term is dimensionless, and:

Δ_s = Shear displacement across the crack (mm);

G_f = Specific gravity of foundation;

d = Diameter of the bar (mm); and

E_s = Elastic modulus of steel (MPa).

However, the high stress concentration in the concrete supporting the bar results in a non-linear behaviour, so that only the initial dowel stiffness can be predicted using Equation (C.1).

The softening of the concrete supporting the dowel bar results in a redistribution of the reactions, so that the maximum bending moment in the bar moves away from the crack location. Failure occurs either by tensile splitting of the concrete or when the bar reaches its ultimate bending moment. In the latter case the plastic moment is given by:

$$M_p = \frac{1}{6} f_y d^3 \tag{C.2}$$

Where:

f_y = Yield stress of reinforcing steel (MPa).

A study of the internal equilibrium required to produce this moment gave the ultimate dowel force, as:

$$F_{du} = 1{,}30 d^2 f_y^{0,5} f_{cu}^{0,5} \tag{C.3}$$

Where:

f_{cu} = Compressive cube strength for concrete (MPa).

The presence of an axial tensile force in a dowel bar has been shown to reduce the shear stiffness. It is presumed that this is due to localised damage to the concrete adjacent to the bar. However, a tensile force will also cause a reduction in M_p, so that the ultimate dowel force would also be expected to diminish.

Equation (C.3) can predict the ultimate shear force in a dowel bar quite accurately, for specimens without axial tension. For a dowel bar with an axial force of αf_y, Equation (C.2) is modified to:

$$M_p = \frac{1}{6} d^3 f_y (1 - \alpha^2) \tag{C.4}$$

Consequently, Equation (C.3) becomes:

$$F_{du} = 1{,}30 d^2 f_{cu}^{0,5} \{ f_y (1 - \alpha^2) \}^{0,5} \tag{C.5}$$

Which predicts the ultimate dowel force quite closely.

An exponential function was selected to describe the over-all dowel action behaviour. Millard and Johnson (1984) experienced that the actual deterioration of the concrete beneath the reinforcement and the resulting redistribution of internal forces was too complex to permit realistic analytical modelling, and therefore assumed that the dowel force was given by:

$$F_d = F_{du}\left(1 - \exp\left\{-K_i\Delta_s / F_{du}\right\}\right) \tag{C.6}$$

Where:

F_{du} = Ultimate dowel force given by Equation (C.5); and

K_i = Initial dowel stiffness given by Equation (C.1).

The dowel action test results showed that increasing the diameter of the reinforcement resulted in higher shear stiffness and ultimate stress. There was also an increasing tendency for the smooth crack to widen, although this was much less than observed in the aggregate interlock tests. The specimens were cut open after testing to expose the faces of the cracks. This revealed a splitting failure crack in those specimens with 12 mm or 16 mm diameter bars, but also that there was more spalling associated with the larger dowel bars.

C.1.2.2 Millard and Johnson (1985)

In their previous study Millard and Johnson (1984) investigated the shear transfer across cracks in reinforced concrete due to aggregate interlock and to dowel action. Separate specimens were prepared for aggregate interlock testing (see Chapter 2) and for dowel action testing. In this follow-up study (Millard and Johnson, 1985) the combined effect of aggregate interlock and dowel action was studied.

Specimens similar to those prepared for the 1984 study were prepared. The specimens were cracked in direct tension. The tensile force was then maintained while in-plane shear forces were applied across the crack. Measurements of the shear stiffness and subsequent crack widening, together with the tensile forces in the reinforcement were taken, using strain gauges embedded within the bars. A technique of resin injection was used to study the variation in the width of the crack beneath the surface of the concrete. No significant variation was observed.

Initially, two bars of each diameter used in the study (8, 12, and 16 mm) were tested in axial tension up to failure to obtain a calibration curve for each. A study of the anchorage properties of reinforcing bars embedded in concrete showed that the axial stiffness is dependent upon the relative rib area, f_r. An empirical expression was used to relate the local bond stress, τ_x, on the surface of a short length of embedded bar to the local bond slip, Δ_x:

$$\frac{\tau_x}{f_{cu}} = a + b\Delta_x^{17c}$$

(C.7)

Where:

f_{cu} = Ultimate compressive strength of the concrete (MPa)

a, b, c = Constants for a particular value of f_r ($0{,}05 < f_r < 0{,}065$)

The initial axial stiffness at the face of the crack, normal to the plane of cracking, which restrain crack widening, was found to be up to five times higher than when similar reinforcement was used in aggregate interlock tests, because of the effect of local bond. A reduction in the width of the initial crack from 0,5 mm to 0,125 mm resulted in an increase in the shear stiffness and the ultimate shear stress of up to five times. Increasing the diameter of the reinforcement resulted in an increase in the shear stiffness and ultimate shear stress, but it had less influence upon the ratio of crack widening to shear slip than might be expected. The normal stiffness did not increase proportionately to the reinforcement ratio. This was attributed to the poorer anchorage properties of the larger-diameter bars.

When cutting open some of the specimens, the results indicated that some slip occurred between the reinforcement and the concrete. It has been found that if the angle of the slope of the reinforcing bar spiral rib and the axis of the bar is less than 40°, slip is likely to occur. In this study the mean slope of the ribs were found to be 28°, thus slip was likely to occur, resulting in very little variation in the width of the crack beneath the surface. From this it was deduced that the shear stiffness due to aggregate interlock in those reinforced concrete specimens could be assumed to be the same as that obtained from an aggregate interlock specimen, when the normal stiffnesses are the same. Changes in initial crack width had a greater effect upon the shear stiffness of reinforced concrete specimens than upon aggregate interlock specimens.

In conclusion Millard and Johnson (1985) remarked that a comparison of the reinforced concrete test results with the previous aggregate interlock and dowel action tests had shown that no fundamentally different mechanics occur. There was, however, an interaction between the two modes of behaviour. Aggregate interlock caused additional tensile forces in the reinforcement due to overriding of the crack faces. This caused a reduction in the dowel action shear stiffness and strength. Likewise, local bond between the reinforcement and the concrete, absent from the aggregate interlock tests, produced a higher tensile stiffness normal to the plane of cracking, resulting in an increase in the aggregate interlock shear stiffness and strength, but this was sensitive to deterioration of the local bond. *Large initial crack widths, low concrete strengths or the use of large-diameter bars all had an adverse effect upon the anchorage stiffness of the reinforcement and consequently upon the aggregate interlock shear stiffness and strength.*

Therefore, when the tensile stiffness of the reinforcement normal to the plane of cracking is known, the two-phase aggregate interlock model and the elasto-plastic dowel-action model can be used to predict

the behaviour of reinforced concrete specimens cracked in tension and then subjected to in-plane shear across the cracks.

C.1.2.3 Snyder (1989)

The construction of full-depth repairs of Portland cement concrete (PCC) pavements has become a major part of pavement rehabilitation programs throughout the United States. Many of these repairs failed due to failure of the repaired load transfer system. During 1985 the University of Illinois Department of Civil Engineering contracted with the Federal Highway Administration (FHWA) to conduct extensive field, laboratory, and analytical studies concerning the evaluation and rehabilitation of concrete pavements. This study included repeated shear load testing of dowels installed in concrete and surveys of more than 2 000 in-service, full-depth repairs with various load transfer system designs.

This study involved the application of repeated shear loads to dowels anchored in holes drilled in concrete specimens. Data collection and analysis focused on the relationship between applied load and dowel deflection. The purpose of the laboratory study was to estimate the effects of several design and construction variables on the performance of dowels that are anchored into existing PCC slabs during the placement of full-depth repairs.

Five design and construction variables were included in the main test matrix:

a) Dowel diameter.
b) The width of the void to be filled with anchor material when the dowel is placed in the exact centre of the drilled hole.
c) Anchor material.
d) Embedment length.
e) Drill type (varying drill impact energy).

PCC slabs were obtained from Interstate 70 near Effingham, Illinois, for the fabrication of test specimens. Four undamaged slabs (1,2 m by 3,6 m) were lifted out of the pavement and transported to the University of Illinois, where they were cut into 310 mm by 460 mm test specimens. The specimen bases were capped with cement mortar to provide a stable base for testing. A steel drilling frame was assembled to hold the specimens and drill rigs, ensuring that the holes were drilled perpendicular to and centred within one of the 310 mm faces of each test specimen.

Anchor materials were prepared just prior to installation of the non-coated steel dowels. A two-cylinder caulking-gun arrangement provided by the manufacturer dispensed the epoxy mortar. The cement grout was mixed in accordance with the manufacturer's recommendations for achieving a "flow able" mix. A vinyl bag was filled with the grout and squeezed to force the grout through an attached

nozzle into the drilled hole. A tight-fitting nylon disk was fixed on each dowel at a distance equal to the embedment length to prevent the anchor material from flowing out of the holes and creating voids around the dowels.

Two specimens were prepared using 25 mm diameter dowels cast in fresh (20,7 MPa) concrete with 229 mm of embedment. These specimens were cured for 24 hours, subjected to 5 000 load cycles (to simulate early opening of the repair), cured for an additional 27 days, and subjected to an additional 595 000 load cycles. This was to set a standard of deflection performance against which to compare the anchored dowels, and to simulate the conditions imposed on the end of the dowel embedded in the repair.

Two specimens were also prepared to test the performance of the dowels installed in close-fitting holes. Dowels were turned on a metal lathe to achieve dowel diameters of 27 and 28 mm. The dowels were inserted in holes drilled with 27 mm nominal diameter steel drills. The smaller of the two bars was loose enough to be moved slightly in any direction. Some epoxy mortar was placed around this dowel at the concrete face. The larger bar could not be inserted to full depth by hand and was forcibly hammered into the hole without epoxy mortar.

Specimens fabricated using cement grout were allowed to cure in the lab for 7 to 14 days prior to testing. Specimens prepared using epoxy mortar were cured for 24 hours to 7 days.

Repeated bi-directional vertical shear loads were applied to the dowel installed in the test specimens Several load waveforms (simulating the passage of 160 kN tandem axles) were tried during preliminary tests. Specimen response was found to be relatively insensitive to the waveforms being considered. Thus a sinusoidal form with a peak magnitude of 13,4 kN (3 000 lb) and a frequency of 6 Hz was ultimately selected. This resulted in the application of nearly 520 000 load cycles per day, or about a year's worth of heavy traffic loads daily.

Loads were generated hydraulically using an MTS Model 661 ram with a 50 kN capacity. The load was applied to the dowel through a specially fabricated, high-strength steel-loading collar that allowed vertical deflection and associated angular dowel movement about a lateral axis.

A linear variable displacement transducer (LVDT) was mounted on an aluminium bracket attached to the face of each specimen and connected to the load collar using a small threaded nylon rod. This device was used to measure electronically the movement of the load collar and dowel relative to the PCC specimen.

The following conclusions and observations were drawn from this study:

a) The use of grout disks was essential to achieve the potential performance of any anchored dowel installation. These disks should be specified for all doweled, full-depth repair construction projects to ensure good bearing support around the dowel.

b) The epoxy mortar anchoring material was easier to use and produced more consistent results than the cement grout.

c) The use of larger dowel diameters significantly reduced concrete bearing stresses, dowel deflections, and dowel looseness when all factors were held constant.

d) Increasing the size of the *drilled hole radius minus dowel radius* from 0,8 mm to 3,2 mm improved the performance of dowels anchored in cement grout, because better distribution of stiff grout could be achieved. Very fluid grouts performed poorly, regardless of the gap.

e) Small gaps improved the performance of dowels anchored in epoxy mortar, because thinner supporting layers of epoxy mortar, which was softer than the concrete specimens, deformed less than thick layers.

f) Reducing dowel embedment resulted in very small increases in dowel deflection and looseness when epoxy mortar was used. Even smaller increase resulted when good cement grout specimens were tested.

g) Close-fitting holes offered promise when used with good anchor materials, quality control, and grout retention disks.

h) The hollow stainless steel dowel performed adequately, although it did not bond with the epoxy mortar that was used. Concurrent testing by FHWA demonstrated the need to fill hollow dowels with concrete or some other stiff material to reduce deformation of the dowel at the joint face.

i) It appeared that the following design and construction parameters could provide excellent field performance:

   i) 38 mm diameter (nominal), corrosion-resistant solid steel dowels.

   ii) 39,7 mm diameter (nominal), guided drills for epoxy mortar anchor materials.

   iii) 44,5 mm diameter (nominal), guided drills for cement grout anchor materials.

   iv) 178 mm or greater dowel embedment.

   v) Use of rapid-curing, consistent, easy-to-use anchor material (reduction of the emphasis to use cheaper materials when they are difficult to install adequately).

   vi) Use of grout retention disks during curing of the anchor materials.

C.1.2.4 Hossain and Wojakowski (1996)

Hossain and Wojakowski (1996) reported the results of a survey, conducted over a period of 9 years, where six jointed reinforced concrete pavement (JRCP) and one jointed plain concrete (JPCP) pavement test sections were surveyed annually for faulting. The main focus of the investigation was to determine the effect of *concrete mix consolidation* with time on joint faulting and load transfer efficiency.

The fundamentals on which the study was based, reached prior to the investigation, are that four major types of distress affect the performance of concrete pavements:

a) Loss of foundation support, caused by erosion and pumping of subbase materials from beneath the slab.
b) Joint or crack faulting, arising from heavy loads moving across the joint.
c) Slab cracking, caused by fatigue damage resulting from repeated heavy loads, bending stresses due to loss of support, tensile stresses due to thermal and moisture gradients, and uneven foundation settlement.
d) Joint deterioration, caused by poor joint design, non-working or frozen load transfer devices and D-cracking caused by frost-susceptible, non-durable aggregates.

Twenty-three test sections with lengths from 32 to 1 584 m were constructed with various adjustments to vibrator settings (frequency and amplitude), concrete admixtures, and other special features of JRCP. Seven of these test sections were monitored for long-term performance for this joint faulting and load transfer efficiency study.

Joint fault depth measurements were made with a fault meter built from the plans provided by the University of Illinois. Falling weight deflectometer (FWD) tests were done using a Dynatest-8000 FWD to assess the load transfer efficiencies of the joints.

The results of this study showed that:

a) As the original concrete density increased because of improved consolidation, the rate of increase of joint fault depth decreased at doweled joints.
b) The occurrence of joint faulting was much more severe when load transfer devices were not present.
c) Improved concrete mix consolidation appeared to improve load transfer, resulting in a lower rate of faulting.

C.1.2.5 Parsons, Eom, and Hjelmstad (1997)

A two-dimensional finite element model of a doweled joint in a rigid pavement system was described by Parsons et al (1997). They introduced and tested a definition of joint efficiency based on load transferred through dowel action, as follows:

$$\eta_{shear} = \frac{V_{dowel}}{V_{slab}} \qquad (C.8)$$

Where:

η_{shear} = Shear load transfer efficiency (range 0 – 1)

V_{dowel} = Shear force transferred across the gap through the dowel bar (kN);

V_{slab} = Shear force transferred through a continuous slab (kN); and

This shear load transfer efficiency was found to be a more useful measure of joint performance, as it captured the reduction in efficiency that accompanies an increase in the misfit of a joint.

C.1.2.6 Sargand (1999)

The Ohio Research Institute for Transportation and the Environment, together with the Ohio University installed 12 dowel bars in an in-service pavement to monitor their response under environmental cycling and dynamic loading.

Suitable sites were located approximately 5 miles east of Athens, Ohio where U.S.50 was being upgraded from a 2-lane facility to a 4-lane divided highway to instrument and install 12 dowel bars and monitor their response under environmental cycling and dynamic loading. The concrete slab was constructed 254 mm (10 inch) thick.

Six dowel bars were instrumented to monitor dynamic and environmental response. A small area was machined flat on the top and bottom of each bar at its midpoint for Micro-Measurements uniaxial strain gauges and on one side for a 45° rosette. The gauges were either welded to the bars or cemented with AE-10 epoxy. Micro-Measurements M-Coat F components were then used to prevent the intrusion of moisture and protect the gauge and sensor leads. Shallow grooves were cut from the midpoint to the end of the bars to house the lead wires. A small cavity was cut in the end of the bars where the lead wires could be epoxied and protected from the concrete. Three instrumented bars were inserted into each of two dowel bar baskets at positions corresponding to 0,152, 0,762, and 1,981 m from the outside edge of the pavement. The two baskets were set at consecutive joints.

Thermocouples were installed 0, 76, 152, and 229 mm from the bottom of the slab at four locations near the dowel bars to monitor pavement temperature. The three sensors closest to the bottom of the slab were fabricated into a single unit and attached to the dowel baskets. The top thermocouple was installed during placement of the concrete by making a 25 mm deep groove in the green concrete, placing the sensor in the groove, and covering it before finishing was initiated. Contraction joints were sawed in the pavement directly above the strain gauges to control shrinkage cracking.

Six additional bars were machined in a similar manner and used in two joints placed at a different time. Some of these dowel bars were instrumented with fibre optic gauges and installed at identical positions

in the pavement to provide redundant strain measurements. Slightly smaller areas were required on the bars for mounting the fibre optic gauges than was required for the wire gauges.

The uniaxial and rosette strain gauges were both capable of collecting slow responses due to changes in the environmental conditions and fast responses induced by dynamic loads. For environmental responses, data collection was initiated one hour before placement of the concrete and continued at 30-minute intervals for 37 days. Each data point was the average of five readings taken at 60-second increments.

Bending moments in the steel dowel bars were calculated using the following formula:

$$M_z = \frac{E_d I_d (\varepsilon_b - \varepsilon_t)}{2c} \tag{C.9}$$

Where:

M_z	=	Bending moment (Nm);
E_d	=	Modulus of elasticity (MPa);
I_d	=	Moment of inertia of the dowel;
ε_b, ε_t	=	Strain at bottom and top; and
c	=	Dowel bar radius (mm).

A strong correlation between differential temperature in the pavement slab and bending moment in the dowel bars was observed. The magnitude of these bending moments and the corresponding stresses in the dowel bars was much higher than expected. Bearing stresses are of particular concern early in the life of the pavement because the concrete has not attained its full compressive strength.

The magnitude of these bending moments will depend upon the amount of curvature being induced in the slab by curling and warping as well as the extent to which curvature is being resisted by dowel bar stiffness and the bearing resistance of the concrete surrounding the bars.

The relationship between bending moment and maximum stress in the dowel bars were calculated with the formula:

$$\sigma_d = \frac{M_z c}{I_d} \tag{C.10}$$

Where:

σ_d	=	Stress (MPa);
M_z	=	Bending moment (Nm); and
c	=	Dowel bar radius (mm).

The calculation of concrete bearing stress around the dowel bars involved certain assumptions, as shown in the following equation:

$$\sigma_b = K\left[\frac{P - \beta M}{2\beta^3 E_d I_d}\right] \qquad \text{(C.11)}$$

Where:

σ_b = Bearing stress (MPa);

K = Modulus of dowel support;

P = Shear Force on a dowel bar (kN);

β = $\sqrt[4]{\frac{Kd}{4E_d I_d}}$; and

d = Dowel bar diameter (mm).

The allowable bearing stress of fully cured concrete is 23 MPa (3300 psi) as calculated with the empirical formula:

$$\sigma_b = \frac{(4 - d)}{3} f_{cu} \qquad \text{(C.12)}$$

Where:

σ_b = Allowable bearing stress (MPa);

f_{cu} = Ultimate compressive strength of concrete (MPa).

During curing, the allowable bearing stress of PCC increases as its ultimate compressive strength increases. Therefore, the rate at which concrete attains its bearing strength must exceed the rate at which bearing stress is developed around the dowel bars. If the applied bearing stress is greater than the concrete is able to withstand, some type of distress will ensue. Increasing the number and diameter of the bars to reduce concrete bearing stress may not be effective since the overall rigidity of the joint and the induced moment will be increased.

The data collected strongly suggest the need to include environmental parameters in dowel bar design procedures.

In conclusion Sargand (1999) noted that in this study, the magnitude of bending moments generated in the instrumented steel dowel bars as they resist slab curvature during curing and temperature cycling exceeded those generated by FWD loading over the joints. These environmental moments will be even greater in situations where larger temperature gradients are present. As repeated applications of high bearing stress are incurred throughout the life of the pavement, concrete at the dowel bar interface will

wear away, gradually resulting in looseness around the bars. This will reduce the effectiveness with which dowel bars transfer load and limit environmental slab deformations.

Sargand (1999) further concluded that the design of dowel bars for rigid pavement joints involves a delicate balance between resisting slab curvature induced by concrete curing and temperature gradients, transferring dynamic load to adjacent slabs, and maintaining an acceptable bearing stress in concrete around the bars. As load transfer systems become more rigid, slab curvatures are reduced and dynamic loads are distributed better across the slabs, but this rigidity result in greater bending moments being transferred to the concrete. If load transfer systems are made less rigid, slabs will experience greater environmental curvature and more non-uniform support for carrying traffic loads, leading to higher tensile stress in the slab and higher compressive stress in the supporting layers.

He recommended that additional research is needed to clearly identify the manner in which dowel bars can be designed most effectively to carry traffic loads without exceeding the strength limitations of the materials involved.

C.1.3 FINITE ELEMENT DOWEL MODELLING

C.1.3.1 Nishizawa, Koyanagawa, Takeuchi and Kimura (2001)

The objective of this study was to develop a mechanical design method for a doweled joint. In order to investigate the mechanical behaviour of a dowel bar, a mechanical model of a dowel bar in a transverse joint in a concrete pavement was developed based on the three dimensional finite element (3D FE) method PAVE3D.

In the model, a dowel bar is divided into two segments embedded in concrete and a segment between them (see Figure C.1). The segment between slabs is represented with a beam element, connected to two solid elements (P and Q) at both nodes as well as at the inner nodes p and q, because there is no support of concrete surrounding the segment (see Figure C.2). These segments were modelled as a beam on elastic foundation and a 3D-beam element, respectively. The model was verified by comparing the predicted strains in the concrete slab and dowel bar with the experimental data obtained from loading tests conducted on a model pavement and an actual pavement. The effects of the transverse joint structure and subbase stiffness on the stresses in the dowel bar and concrete slab were investigated using numerical simulations with PAVE3D.

In accordance with the design manual used in Japan, the geometry and spacing of the dowel bars are determined empirically. A survey of the condition of concrete pavements in Japan showed that many concrete pavements in heavy-duty roads have suffered from longitudinal cracks that initiated at

transverse joints in wheel paths. It was also found that some dowel bars were broken inside the joint opening of transverse joints.

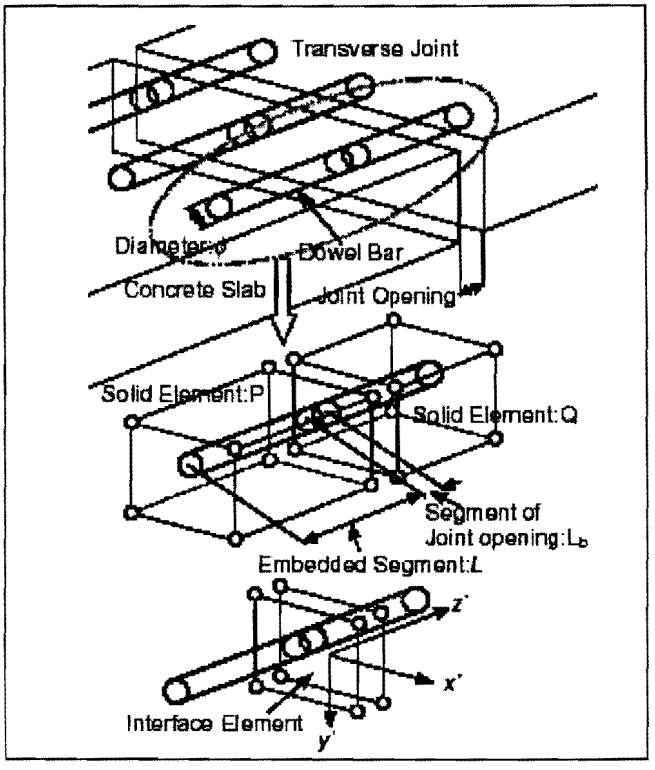

Figure C.1: Dowel bar element (Nishizawa et al, 2001)

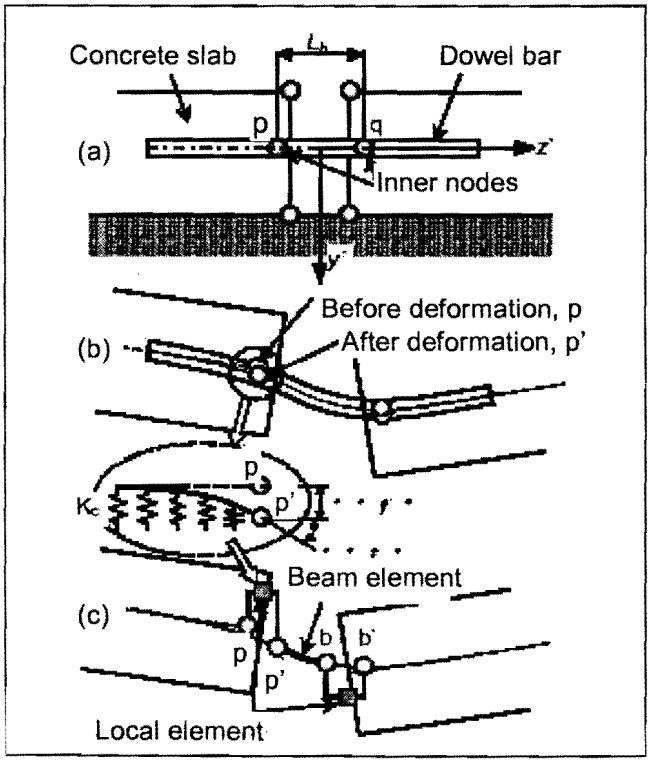

Figure C.2: Displacement of dowel bar element (Nishizawa et al, 2001)

These facts suggested that the current design methods used to determine the diameter, length, and spacing of dowel bars at transverse joints were inappropriate. A rational design method based on mechanical analyses was therefore required.

In order to experimentally investigate the mechanical behaviour of dowel bars, a model pavement with a 100 mm thick concrete slab on a granular subbase was constructed in a laboratory. Two types of transverse joints with 23 mm diameter and 11 mm diameter dowel bars were installed. Strains in the dowel bars produced by a vertical load applied at the transverse joint edge were measured with gauges attached on the surface of the dowel bars. The experiment was analysed by PAVE3D, which allowed the computation of displacements and stresses in the dowel bars as well as in the concrete slab, subbase and subgrade, taking into account the geometry and spacing of dowel bar. The model was verified by comparing the predicted strains in the concrete slab and dowel bars with experimental data obtained from loading tests conducted on a model pavement and an actual pavement. The comparison showed a fairly good agreement and confirmed the validity of PAVE3D. The results showed that the geometry and spacing of dowel bars had a great effect on the stress in the dowel bar but the effect of the stresses on the concrete slab was relatively small. It was also found that increasing the subbase stiffness decreased the stresses in both the dowel bars and in the concrete slab. Therefore, it was concluded from this study that strengthening the subbase might be a good measure to enhance the structural capacity of a concrete pavement system.

APPENDIX D: THEORETICAL CONCRETE PAVEMENT MODELLING WITH 3DFE PROGRAMME EVERFE

TABLE OF CONTENTS

LIST OF TABLES

LIST OF FIGURES

LIST OF SYMBOLS

α	Coefficient of thermal expansion
E	Modulus of elasticity
μ	Poisson's ratio
ρ	Density

APPENDIX D: THEORETICAL CONCRETE PAVEMENT MODELLING WITH 3DFE PROGRAMME EVERFE

D.1 INTRODUCTION

The decisions reached so far as to the modelling techniques that would be used in this study determined the input variables used to first conduct a theoretical analysis of the envisaged concrete pavement models. This was in order to determine the ranges for the different input variables that could be expected during modelling in the laboratory.

D.2 PAVEMENT SYSTEM AND LOADING

The concrete pavement was modelled as two slabs with dimensions 3 700 mm (wide) x 2 250 mm (long) x 230 mm (thick), with 35 MPa compressive strength. These dimensions were chosen as the standard lane width in South Africa is 3,7 m, the standard joint interval for jointed concrete pavements is 4,5 m, and the average concrete thickness is 230 mm. For simplicity the joint was not skewed. Three different types of subbases were evaluated, namely: crushed stone (G1), cement stabilised gravel (C2), and continuously graded asphalt (AC). The natural soil was modelled as an elastic solid foundation using rubber mats to simulate a uniform subgrade and provide continuous support. The rubber used in the modelling was tested beforehand and had a k-modulus of 80 MPa/m. The properties of the materials used in the analyses are summarised in Table D.1.

Table D.1: Input variables for material properties

Portion of system	E (MPa)	μ	α ($^{\circ}C^{-1}$)	ρ (kg/m^3)
Concrete slab (230 mm)	30 000	0,15	$1,1 \times 10^{-5}$	2 400
Crushed stone subbase (125 mm)	450	0,35		2 200
Cement stabilised subbase (125 mm)	3 000	0,35		2 400
Asphalt subbase (40 mm)	2 500	0,44		2 400
Steel	200 000	0,25		

The loading used for each study was a single 80 kN axle, applied at the edge of the first slab. The axle had dual wheels, and each wheel was idealised as a rectangular patch with uniform pressure, acting over a 180 mm wide by 200 mm long contact area. The tyre contact area gave a uniform pressure of approximately 555 kPa (80 psi). The load was placed symmetrically across the centreline of the slab, as shown in Figure D.1. Aggregate interlock load transfer efficiency on each subbase was determined using 9, 19, 37,5, and 63 mm aggregate, by varying the width of the crack or joint between the slabs.

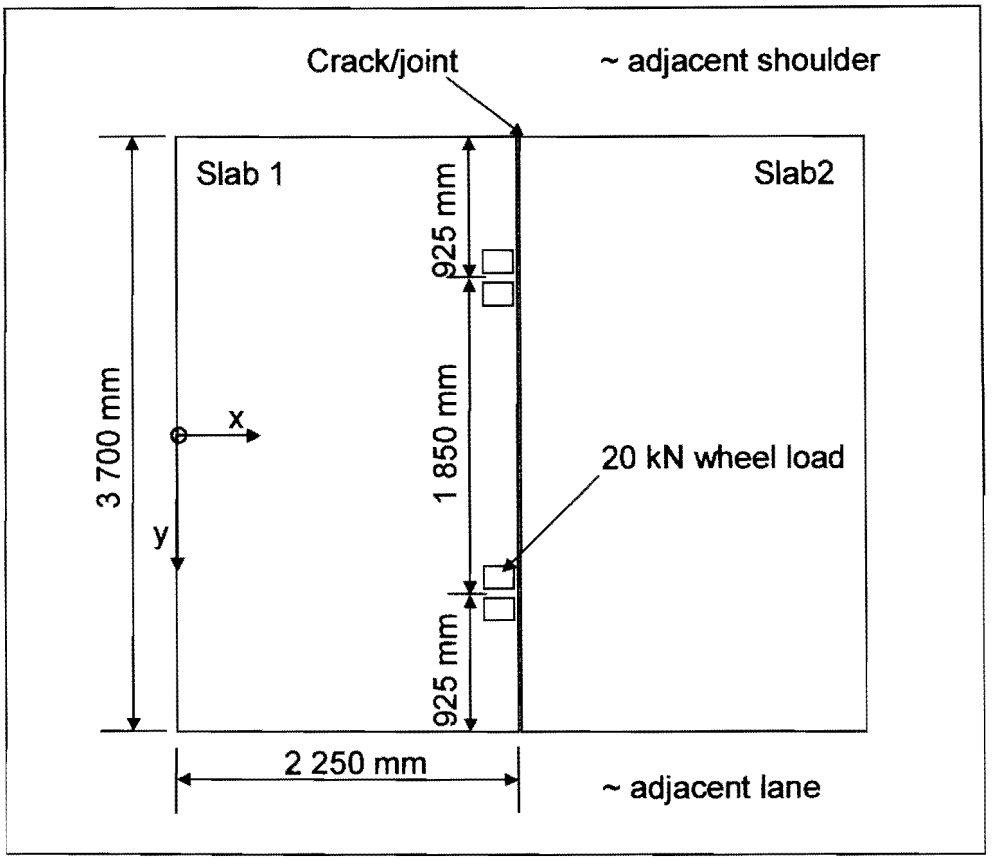

Figure D.1: Plan view of slabs showing wheel loads

The effect of temperature variations through the slab was taken into account by choosing a uniform baseline temperature of 20°C. Assuming that the temperature at the bottom of the slab was 10°C, and at the top of the slab 30°C, implied that the temperature difference was -10°C for the bottom of the slab and +10°C for the top of the slab in relation to the baseline temperature.

All these parameters were set in the three dimensional finite element (3D FE) computer software programme EverFE. The deflection load transfer efficiency of each model was determined at the joint between the slabs, at the centre of the wheel load at (x, y, z) = (2250, 925, -230) and (2263, 925, -230). With the load being placed symmetrically across the centreline of the slab, it was only necessary to evaluate the results at one dual wheel load position. For comparison purposes the deflection load transfer efficiency was also determined at the centre of the slab at (x, y, z) = (2250, 0, -230) and (2263, 0, -230). This was in order to compare the difference between the reaction of the slab at a loaded position versus an unloaded position.

The initial version of EverFE used in the analyses was not able to calculate the aggregate interlock shear force transferred across the joint accurately, nor the shear force transferred through to the dowels.

After personal communication with the developer of EverFE (Davids, 2000) a specific executable file was upgraded so that the theoretical shear load transferred could be determined.

D.3 THEORETICAL AGGREGATE INTERLOCK MODELLING

The deflection load transfer efficiency in the wheel path for each combination of aggregate sizes on the different subbases is presented in Figures D.2 to D.4. The vertical scale was kept constant for all three these figures to facilitate visual comparison. The larger the aggregate size the greater the deflection load transfer efficiency at a specific crack width. This held true for crack widths between 0,1 mm and 2,5 mm. However, the results started to converge to a constant value at a crack width of about 2,5 mm. This was especially noticeable for the smaller aggregate sizes. This "convergence" in the theoretical load transfer efficiency predicted by EverFE confirmed the statement made by Jensen (2001) that the load transfer efficiency of the concrete pavement at crack widths larger than 2,5 mm is a function of the subbase strength. Theoretical analyses with EverFE were carried out at crack widths of 10 mm. The Deflection load transfer efficiency at 10 mm for all aggregate sizes was exactly the same as the minimum deflection value already reached at 2,5 mm in the analysis for the 9 mm maximum sized aggregate. What was also important was the fact that the thin, flexible asphalt subbase had the largest theoretical load transfer efficiency. This could be attributed to easier "embedment" of the concrete in the subbase, compared to "lift-off" that may be experienced on a cement stabilised subbase. To facilitate an easier comparison the deflection load transfer efficiency obtained for the 19 mm maximum sized aggregate on all three subbases evaluated was plotted on one graph (see Figure D.5).

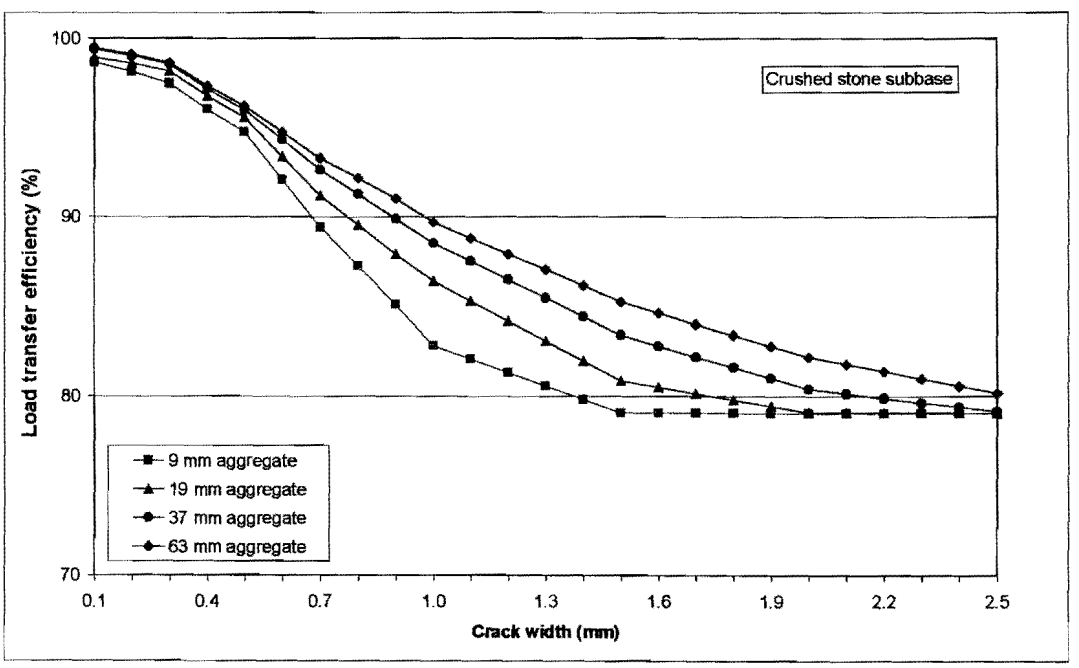

Figure D.2: Deflection load transfer efficiency in the wheel path (crushed stone subbase)

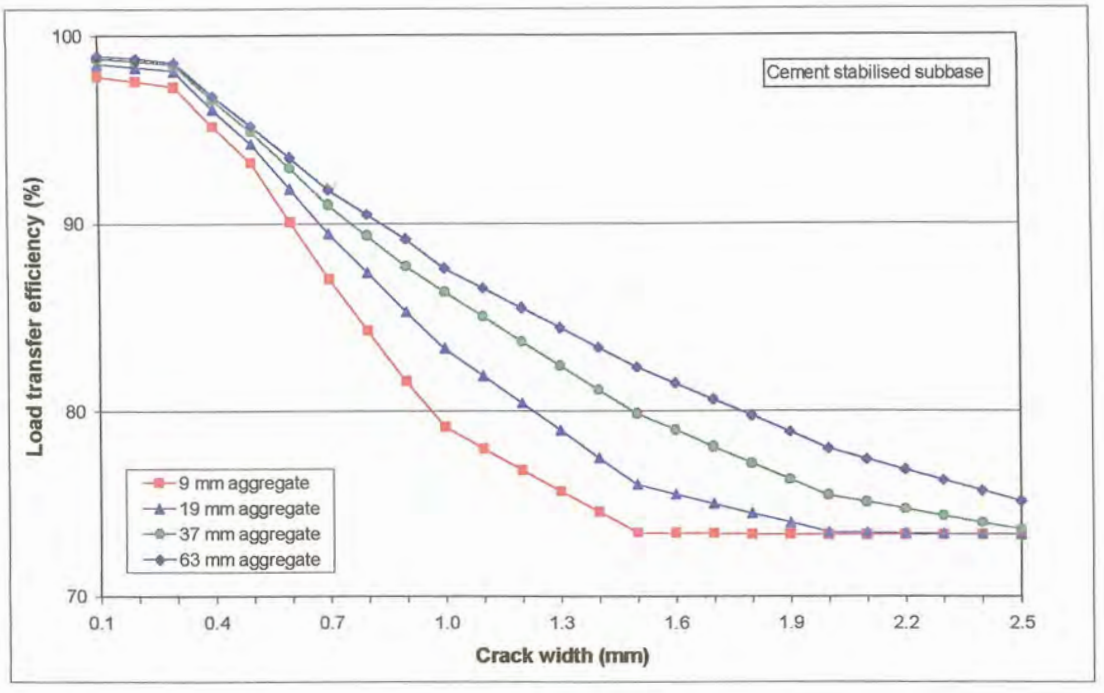

Figure D.3: Deflection load transfer efficiency in the wheel path (cement stabilised subbase)

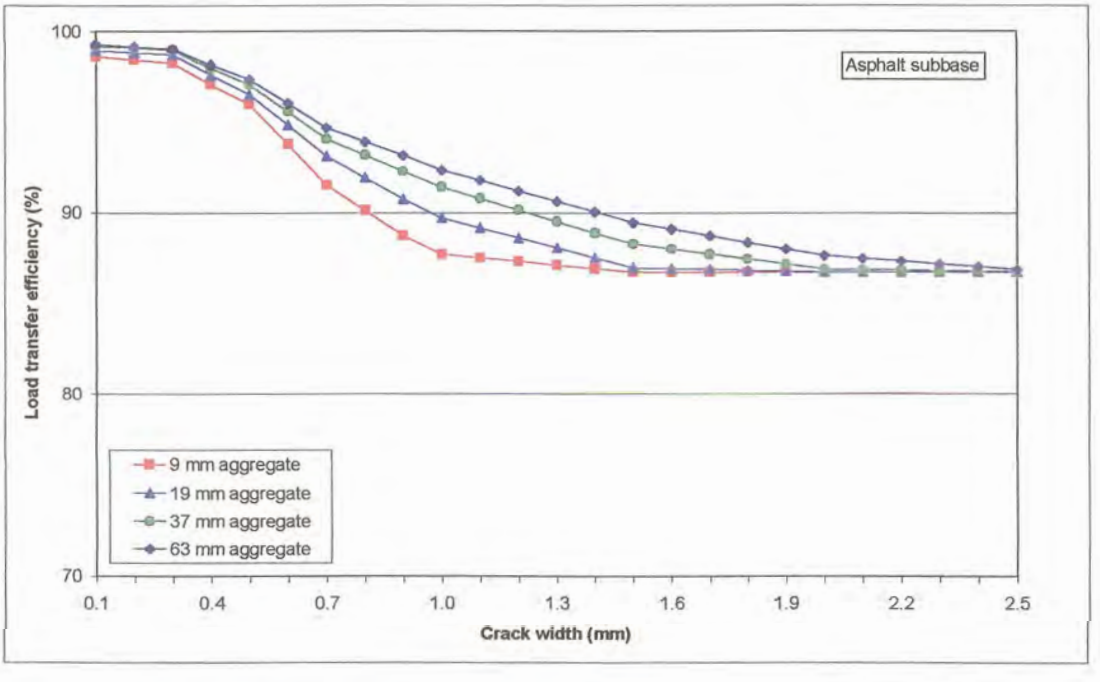

Figure D.4: Deflection load transfer efficiency in the wheel path (asphalt subbase)

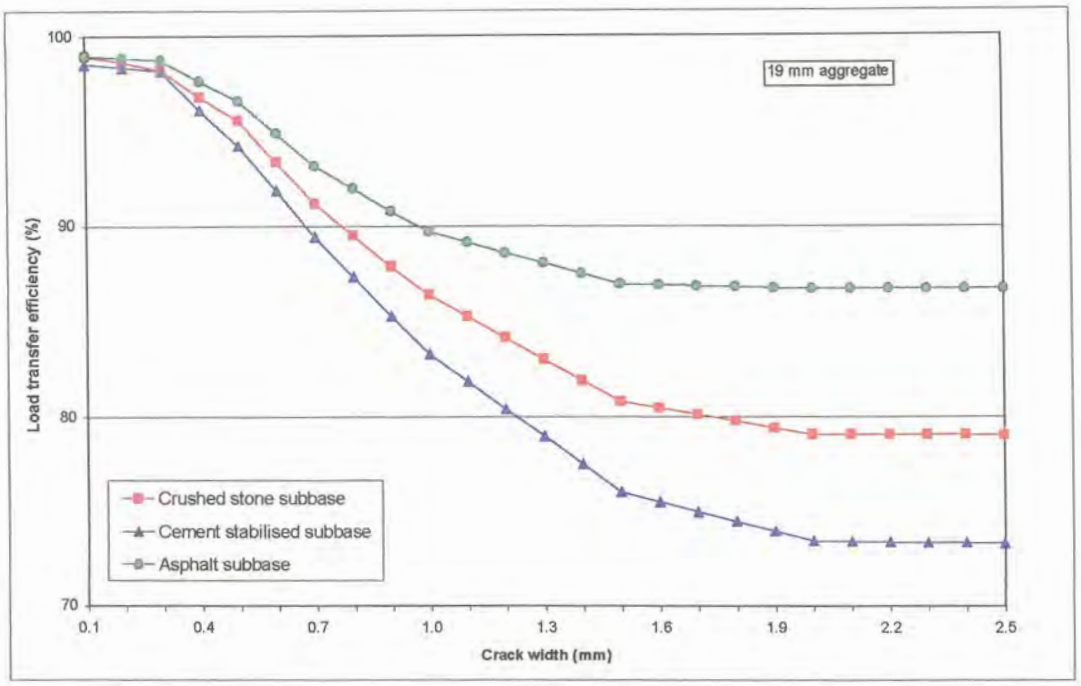

Figure D.5: Deflection load transfer efficiency in the wheel path for all three subbases (19 mm aggregate)

The deflection load transfer efficiency at the centreline of the slab was also determined. Figures D.6 to D.8 present these comparisons for 9 mm and 63 mm aggregate sizes on the different subbases. At small crack widths (< 0,4 mm) the deflection load transfer efficiency at the centreline of the slab was close to 100% in all three figures, and higher than in the wheel path. However, as the crack width increased beyond 0,4 mm, the load transfer efficiency at the centreline became less than in the wheel path. This typically occurred at crack widths of approximately 0,8 mm for the 9 mm maximum aggregate size concrete, and at crack widths of approximately 1,5 mm for 63 mm maximum aggregate sized concrete. This implied that during traffic loading little or no movement takes place at the centreline of the traffic lane, between the wheel loads at small crack widths, but as the crack width increases, the crack tends to open up at the centreline, while it tends to close up in the wheel path. Another practical explanation of this tendency is that the concrete pavement experiences less of the effects of moment and inertia at the centreline than in the wheel path. The larger aggregate size yielded higher load transfer efficiencies than the smaller aggregate size at the centreline between the wheel loads. The load transfer efficiency values at the centreline also tended to converge to a constant value at a crack width of about 2,5 mm, but the eventual load transfer efficiencies were less than in the wheel path

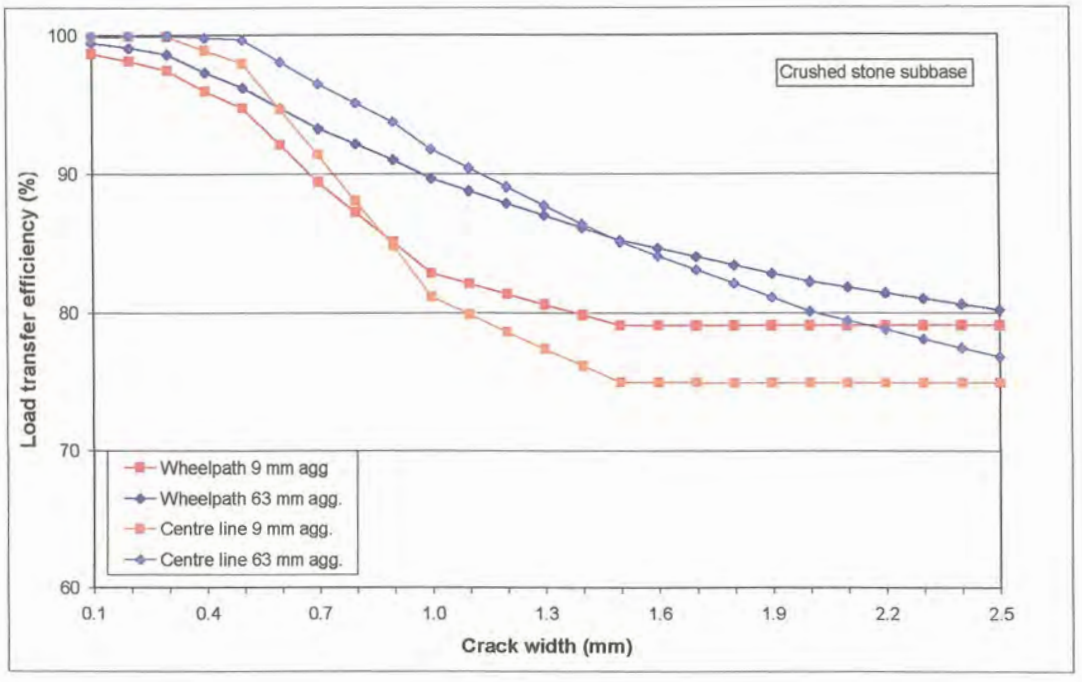

Figure D.6: Deflection load transfer efficiency – wheel path versus centreline (crushed stone subbase)

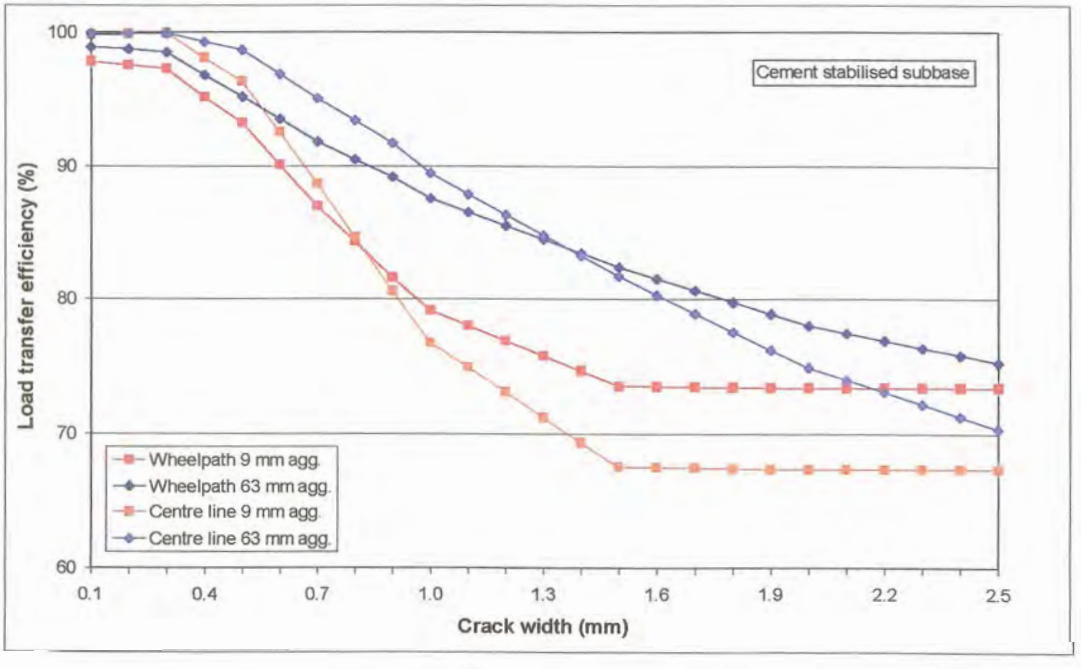

Figure D.7: Deflection load transfer efficiency – wheel path versus centreline (cement stabilised subbase)

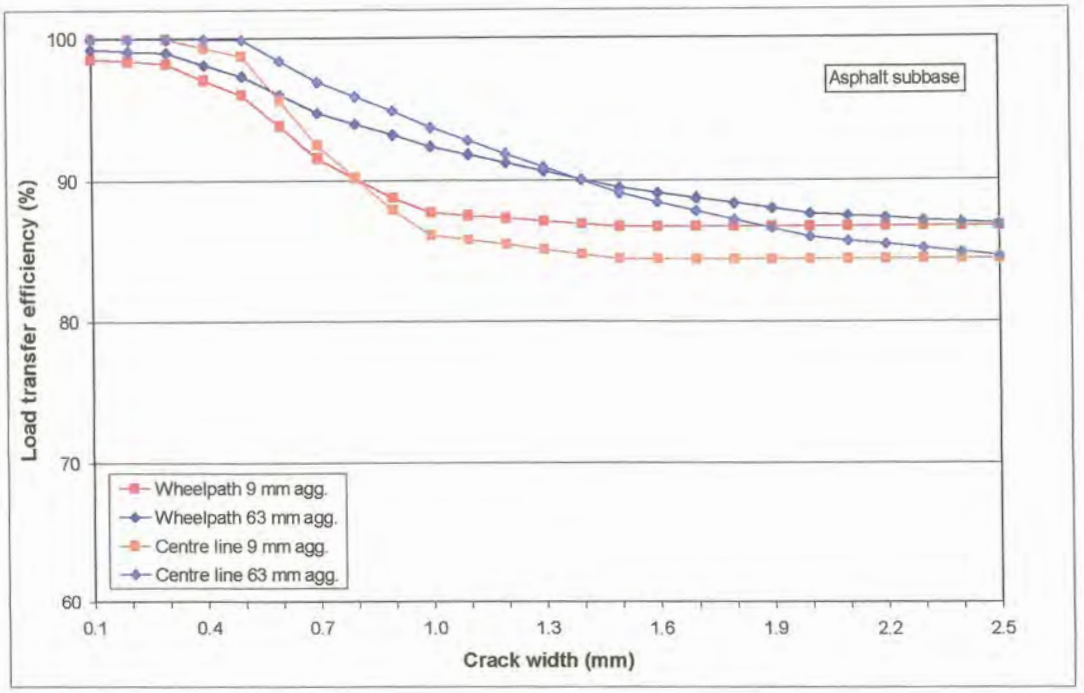

Figure D.8: Deflection load transfer efficiency – wheel path versus centreline (asphalt subbase)

The point of maximum shear stress was in the wheel path at (x, y, z) = (2250, 925, -230). Figures D.9 to D.11 show the maximum shear stress measured in the wheel path for the three subbases considered. The initial lower stress value obtained for the 9 mm aggregate on a crushed stone subbase, can be ascribed to an initial slip that takes place on the weaker subbase, before the maximum stress is reached at a crack width of 0,3 mm.

The numerically integrated sum of the shear force transferred across the joint, reached a maximum at 0,3 mm crack width (due to an initial slip that takes place on the weaker subbase), where after it decreased to approximately 0 kPa at 2,5 mm crack width for the model with a crushed stone subbase. Both the cement stabilised model, as well as the asphalt subbase model had maximum values at 0,1 mm crack width, decreasing to approximately 0 kPa at 2,5 mm crack width (see Figures D.12 to D.14).

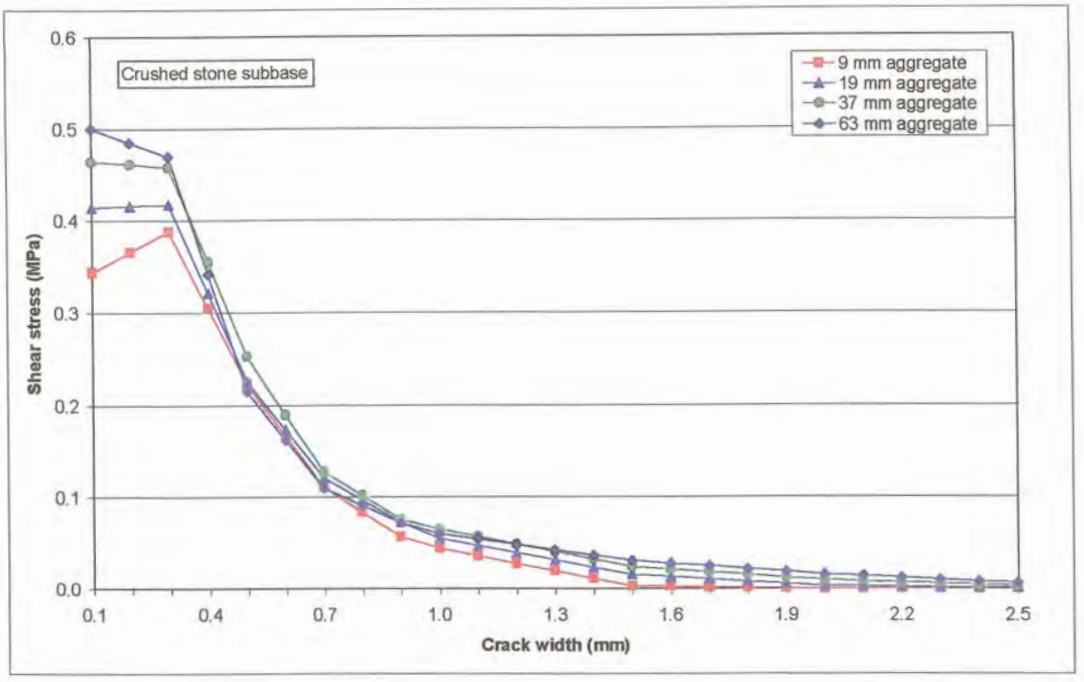

Figure D.9: Maximum shear stress at joint in wheel path (crushed stone subbase)

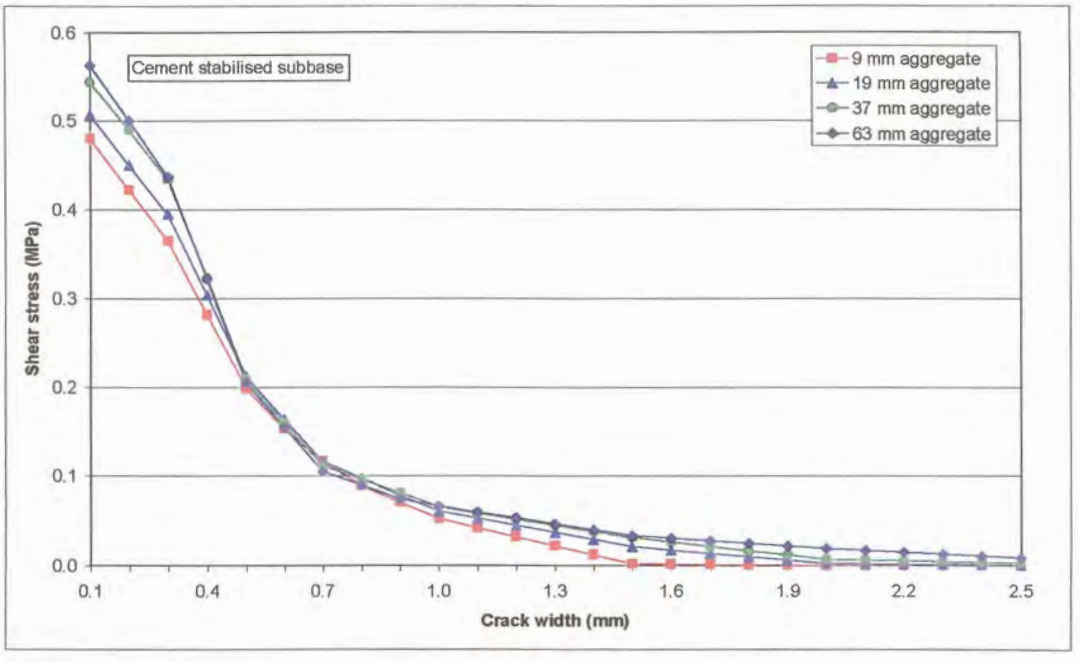

Figure D.10: Maximum shear stress at joint in wheel path (cement stabilised subbase)

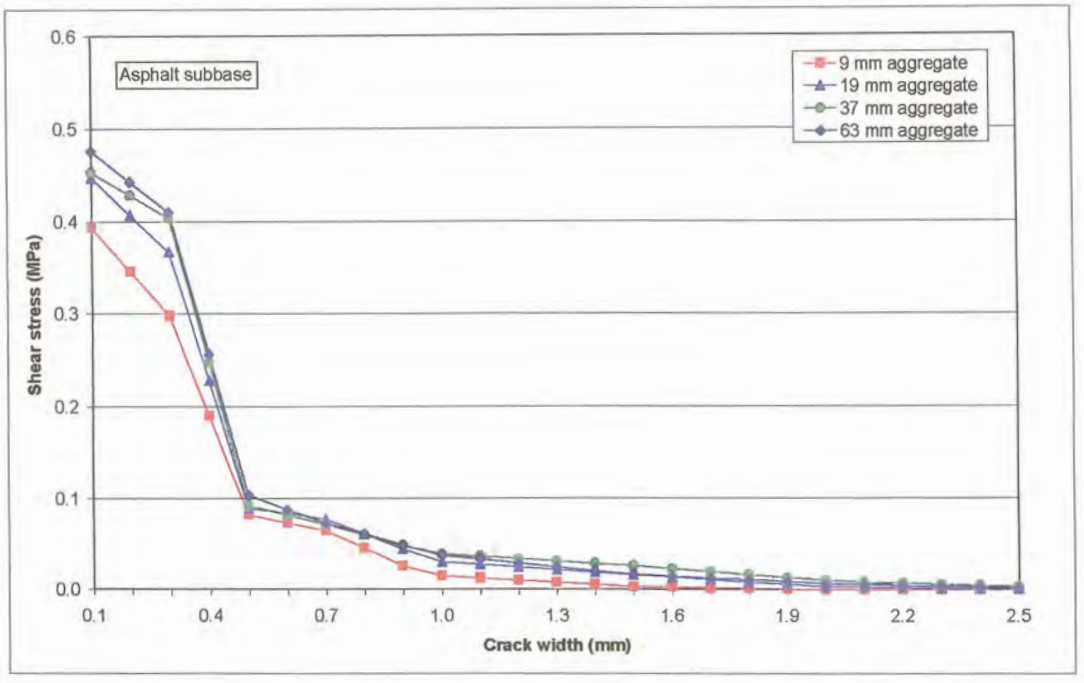

Figure D.11: Maximum shear stress at joint in wheel path (asphalt subbase)

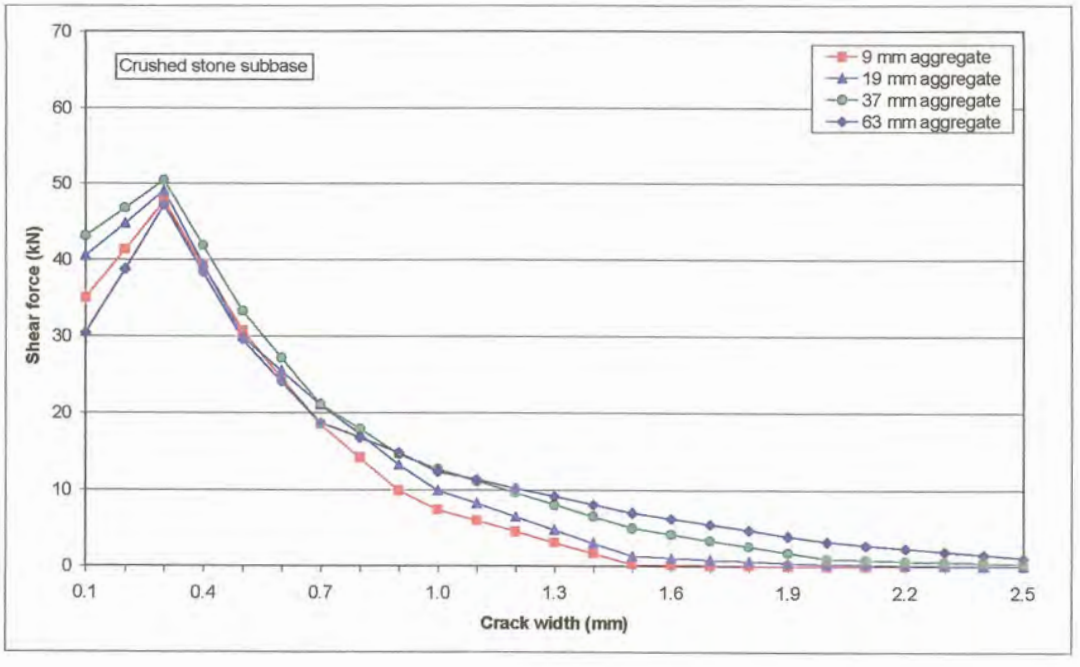

Figure D.12: Total shear force at joint (crushed stone subbase)

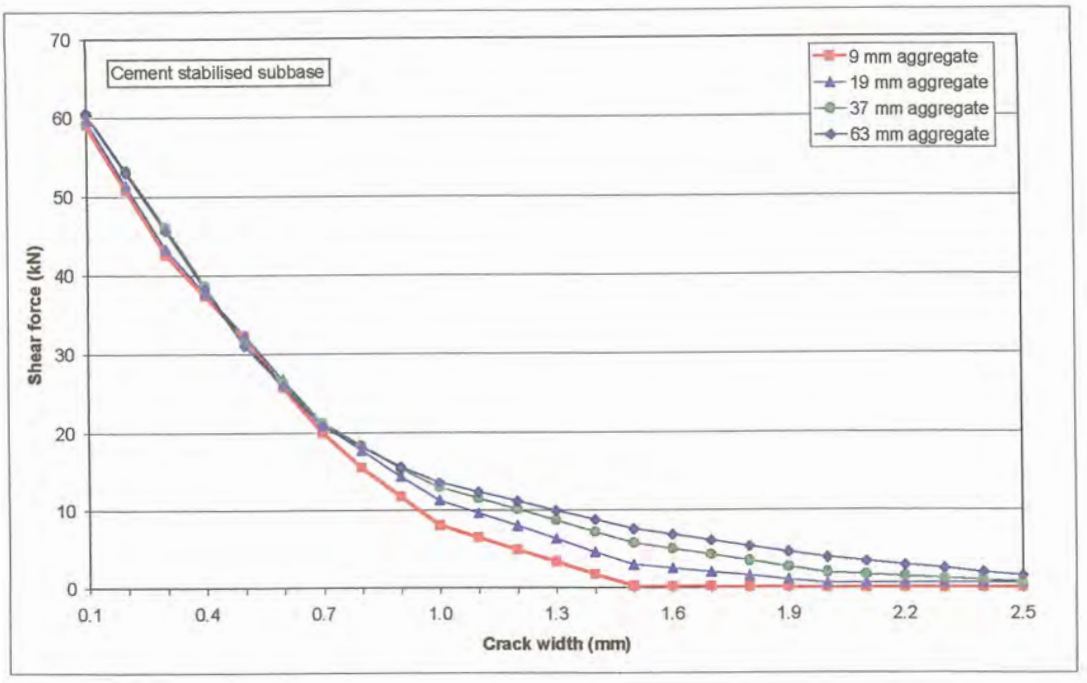

Figure D.13: Total shear force at joint (cement stabilised subbase)

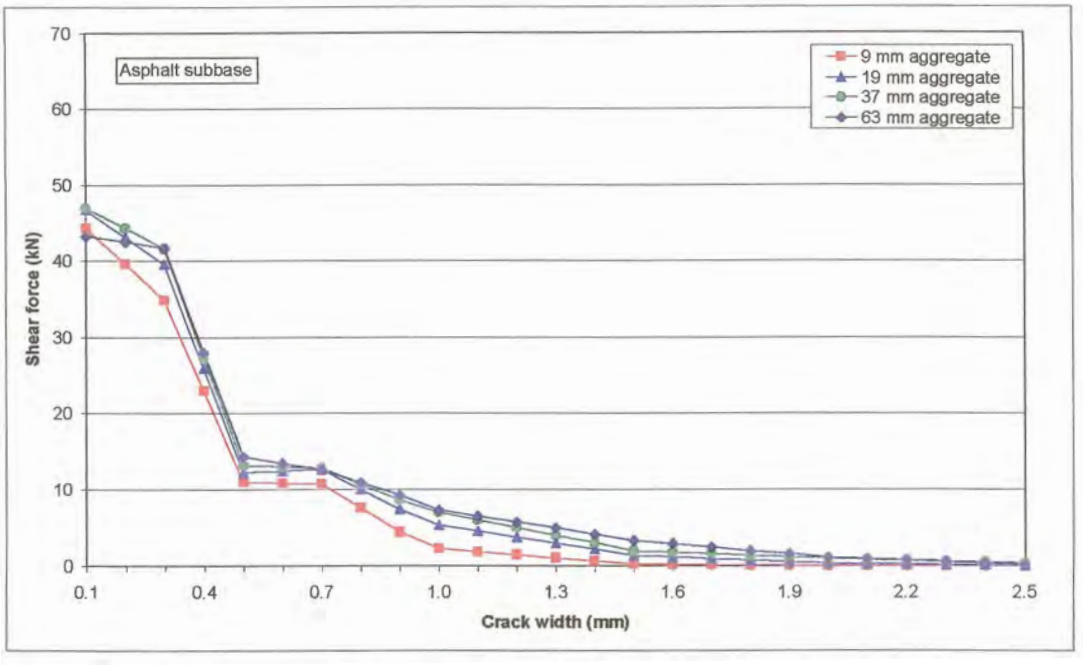

Figure D.14: Total shear force at joint (asphalt subbase)

To quantify the effect of a temperature gradient through the concrete the cement stabilised subbase modelling was repeated with a zero temperature gradient in the concrete, and the results were compared with those previously obtained. The load transfer efficiency in the wheel path showed a marked

difference, with the results converging at approximately 57%, compared to the previous 75% (see Figure D.15). The maximum shear stress and shear force results obtained with the zero temperature gradient models are given in Figures D.16 and D.17. In both instances the graphs showed the same trend, parallel to the previously obtained graphs, but at much lower initial stresses and forces. Depending on the temperature gradient chosen, the results could also have been the opposite. This emphasised the importance of measuring temperature differentials through the pavement when attempting to model the performance.

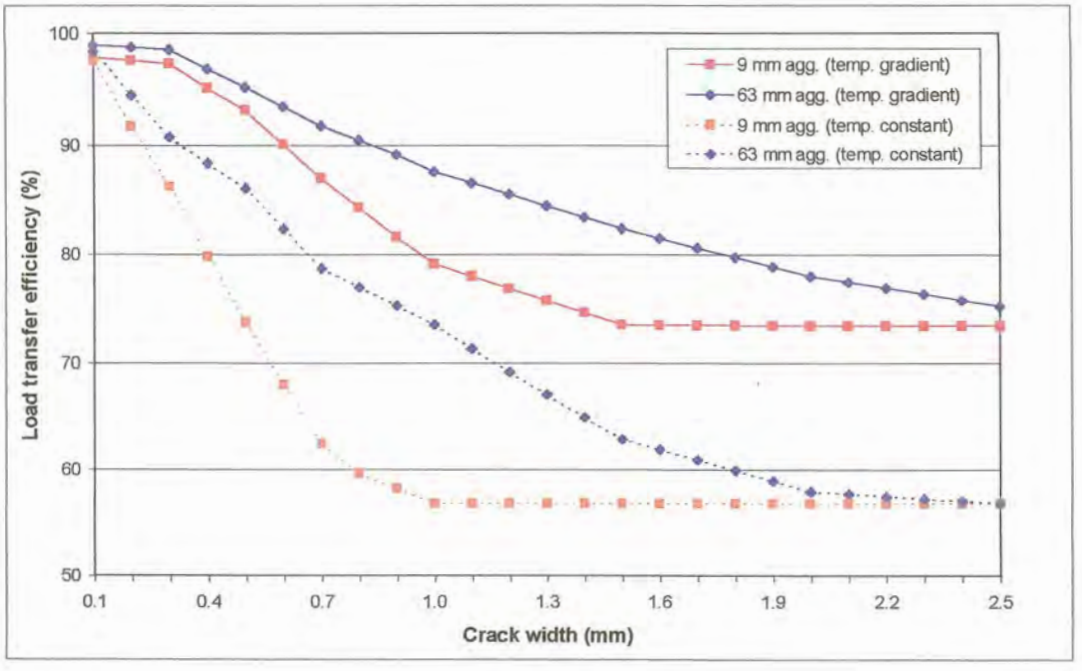

Figure D.15: Deflection load transfer efficiency in wheel path – cement stabilised subbase with and without temperature gradient through concrete slab

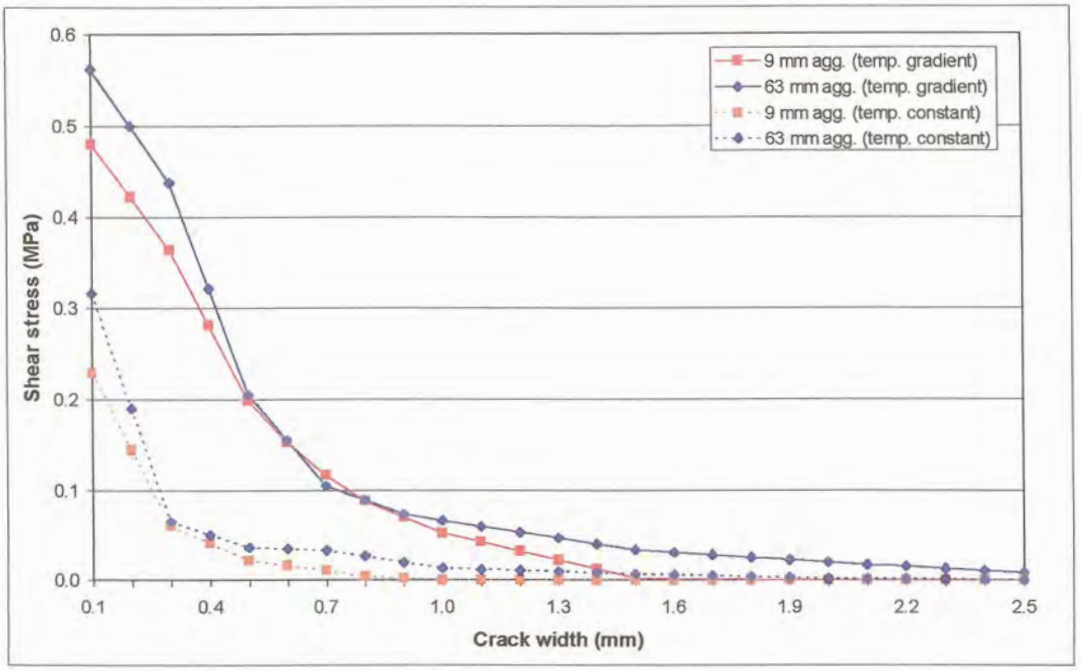

Figure D.16: Maximum shear stress at joint in wheel path – cement stabilised subbase with and without temperature gradient through the concrete slab

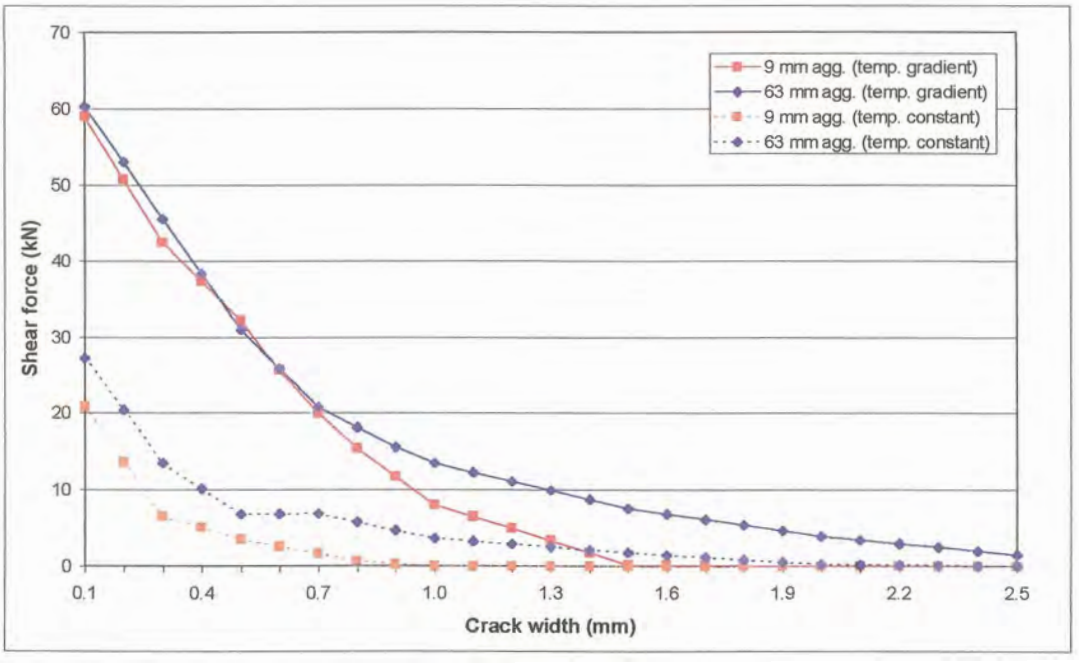

Figure D.17: Total shear force at joint – cement stabilised subbase with and without temperature gradient through the concrete slab

D.4 THEORETICAL DOWEL MODELLING

The effect of dowel looseness was determined using 16, 25, and 32 mm diameter bars (460 mm long) at 300, 450, and 600 mm spacing, respectively, on each subbase, by varying the size of the gap around the dowel. The joint width was set at 12,5 mm to eliminate the effect of aggregate interlock in this case. Figure D.18 (similar to Figure D.1) shows a plan view of the placement of the wheel loads, as well as the dowel bars.

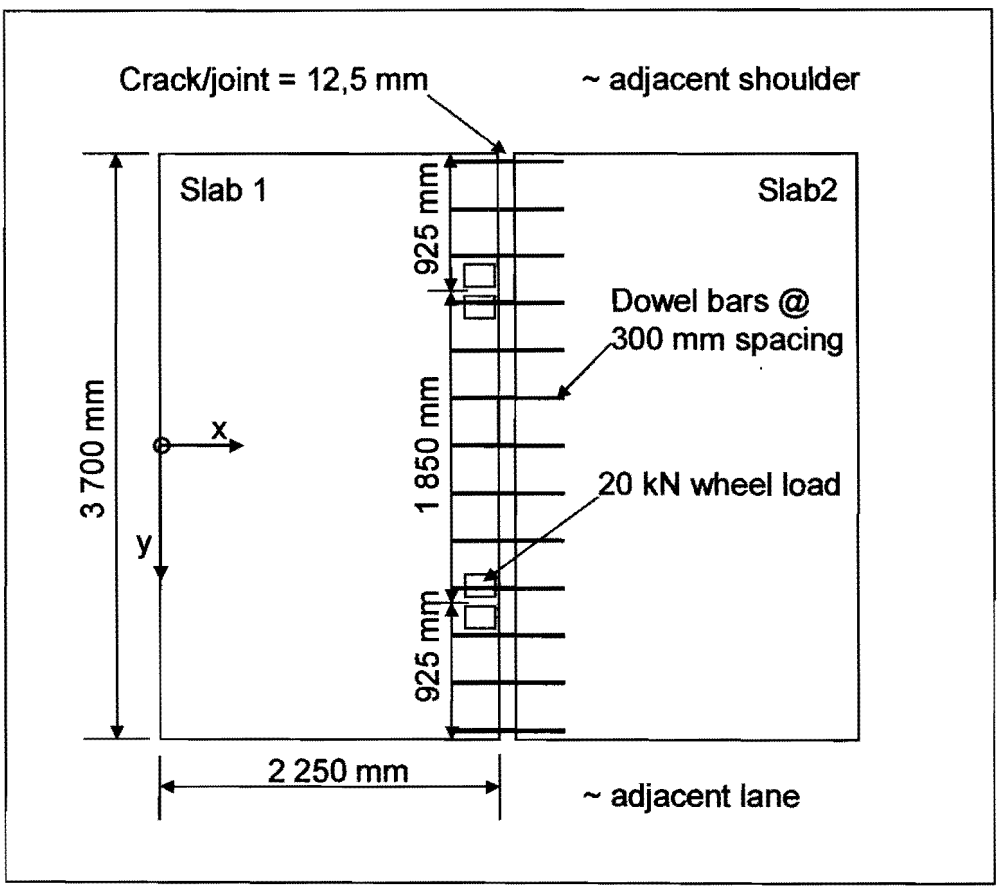

Figure D.18: Plan view of slabs showing wheel loads and dowel bars

The model used to study the effect that dowel looseness has on the response of the pavement is shown in Figure D.19. After setting up the different models, all the parameters were kept constant (as defined in Table D.1), while only the value of the gap between the dowel bar and the surrounding concrete at the joint face was varied from 0,00 mm to 0,10 mm.

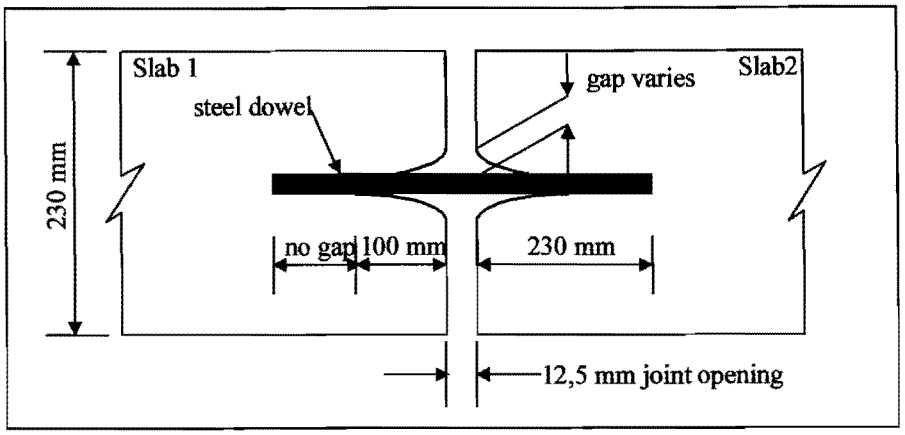

Figure D.19: Cross-section of gap around dowel at joint

D.4.1 CONSTANT DOWEL BAR SPACING AT INCREASED DOWEL BAR DIAMETER

D.4.1.1 Dowel bar spacing – 300 mm

Figures D.20 to D.22 present the deflection load transfer efficiency for 16, 25, and 32 mm diameter dowel bars at 300 mm spacing with increasing gap width around the dowels, on the three subbases considered. The deflection load transfer efficiency increased with increasing dowel diameter.

Once again, the load transfer efficiency at the centre of the slab was compared with that in the wheel path to represent the performance of the pavement at an unloaded position, as well as at the position of loading. The deflection load transfer efficiency in the wheel path for the models with the crushed stone subbase decreased from between 97,4% and 98,7% at 0,0 mm gap width to between 88% and 90% at 0,06 mm gap width, where after it remained constant. Similarly, the values obtained for the models with the cement stabilised subbase also decreased from between 96,7% and 98,5% efficiency at 0,0 mm gap width, to a constant 83,6% for the 16 mm diameter dowel bar, and 87,3% for the 32 mm diameter dowel bar at 0,06 mm gap width. The asphalt subbase models showed a decrease from between 96,9% and 98,4% at 0,0 mm gap width to between 80,8% for the 16 mm diameter dowel bar, and 84,8% for the 32 mm diameter dowel bar at 0,08 mm gap width. Where after it also remained constant. From Figures D.20 to D.22 it is obvious that the load transfer efficiency was higher at the centreline (unloaded position) than in the wheel path (loaded position) for all three subbases considered.

Figure D.23 present a comparison between the deflection load transfer efficiencies determined in the wheel path for 16 mm diameter dowel bars at 300 mm spacing on each of the three subbases simulated in the theoretical analyses. In this theoretical analysis, the crushed stone subbase had the highest and the asphalt the lowest load transfer efficiencies.

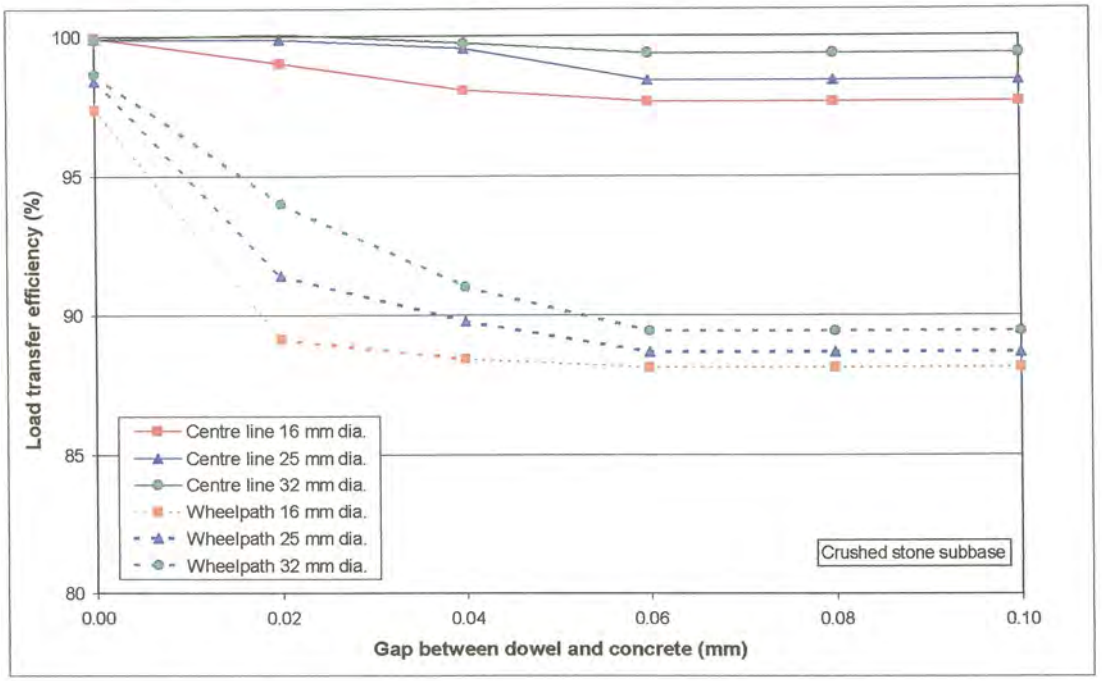

Figure D.20: Deflection load transfer efficiency with dowel bar spacing at 300 mm (crushed stone subbase)

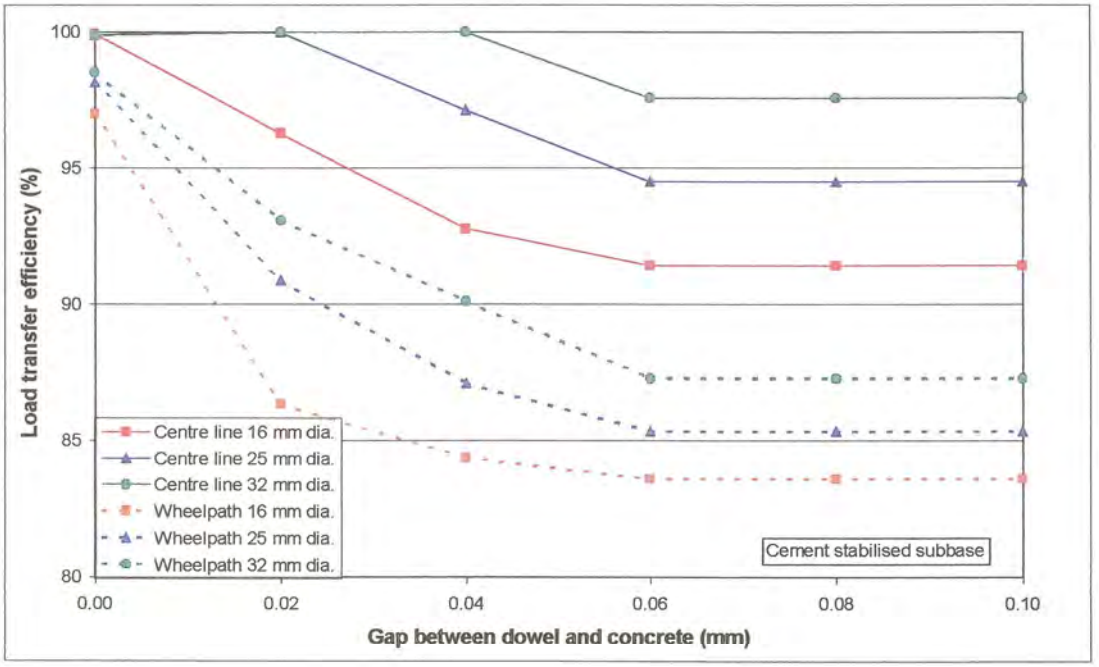

Figure D.21: Deflection load transfer efficiency with dowel bar spacing at 300 mm (cement stabilised subbase)

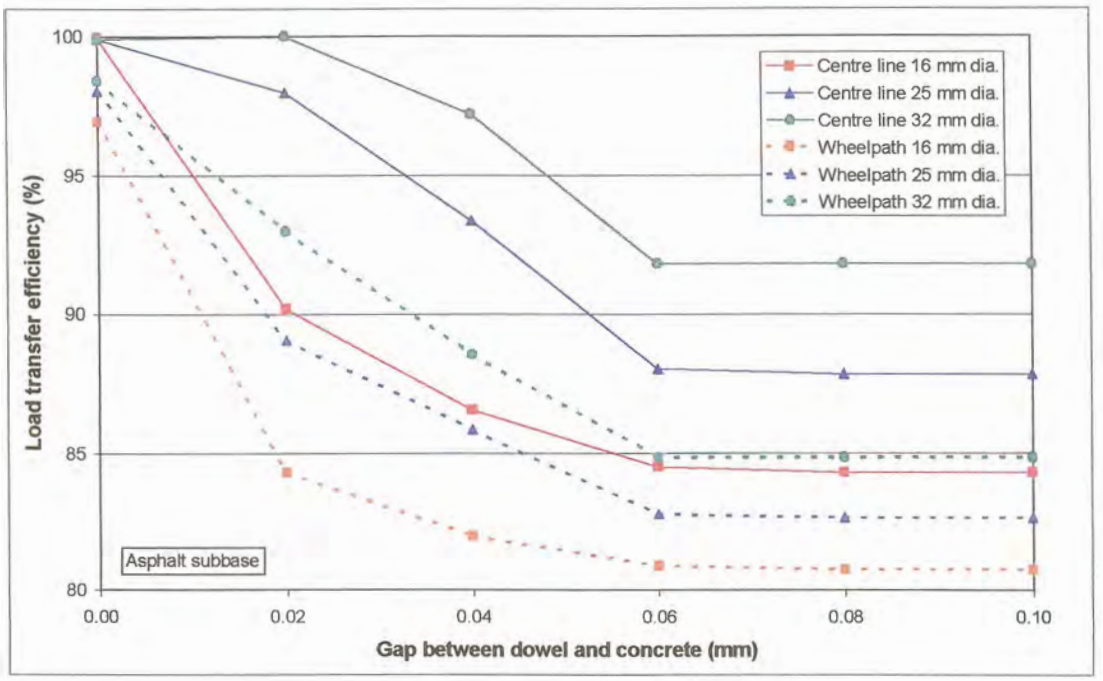

Figure D.22: Deflection load transfer efficiency with dowel bar spacing at 300 mm (asphalt subbase)

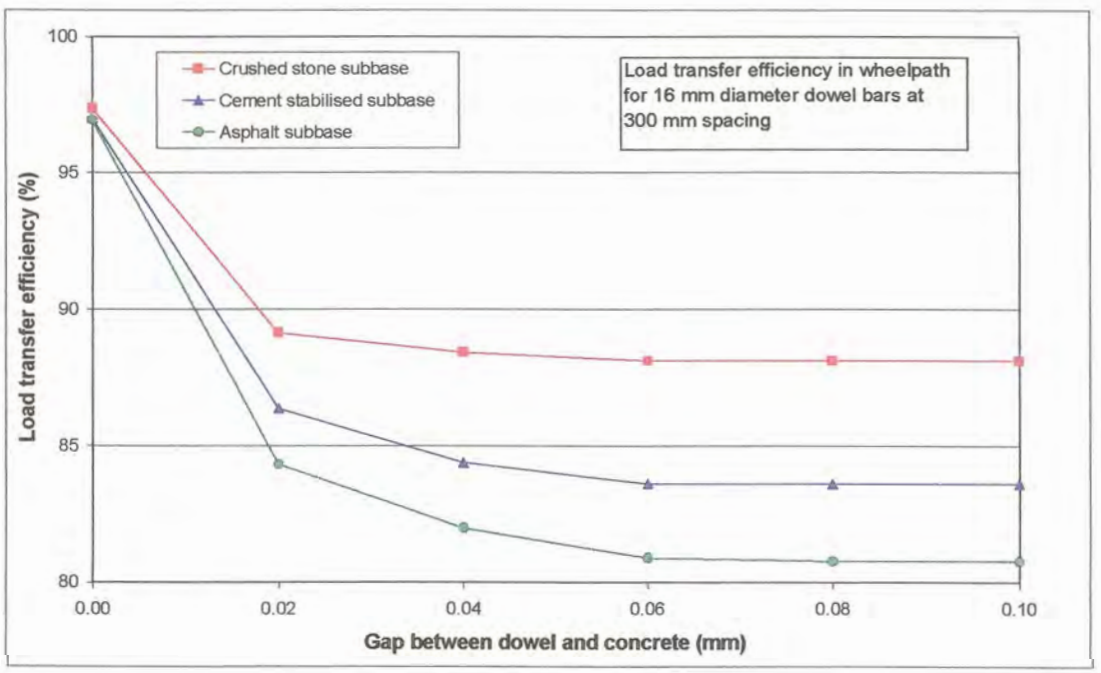

Figure D.23: Deflection load transfer efficiency for 16 mm diameter dowel bars at 300 mm spacing on all three subbases

The total shear force transferred across the joint due to the dowels at increasing gap widths is presented in Figures D.24 to D.26. According to these theoretical modelling results, an increase in dowel diameter results in an increase in shear force transferred across the joint.

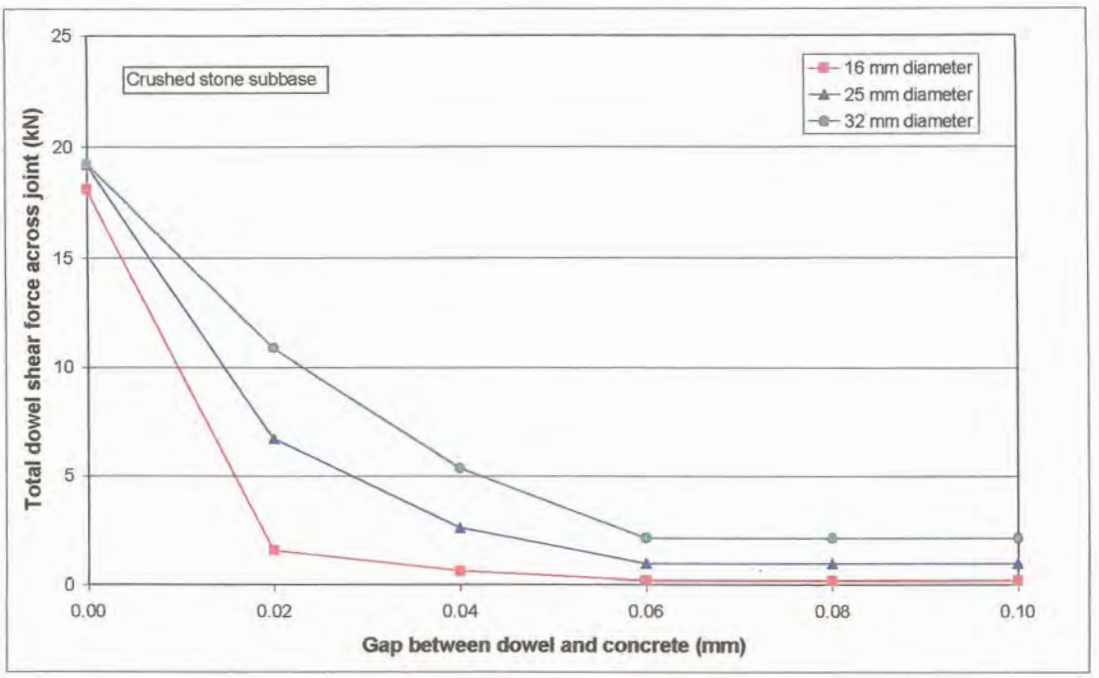

Figure D.24: Total shear force transferred across joint due to dowels (crushed stone subbase)

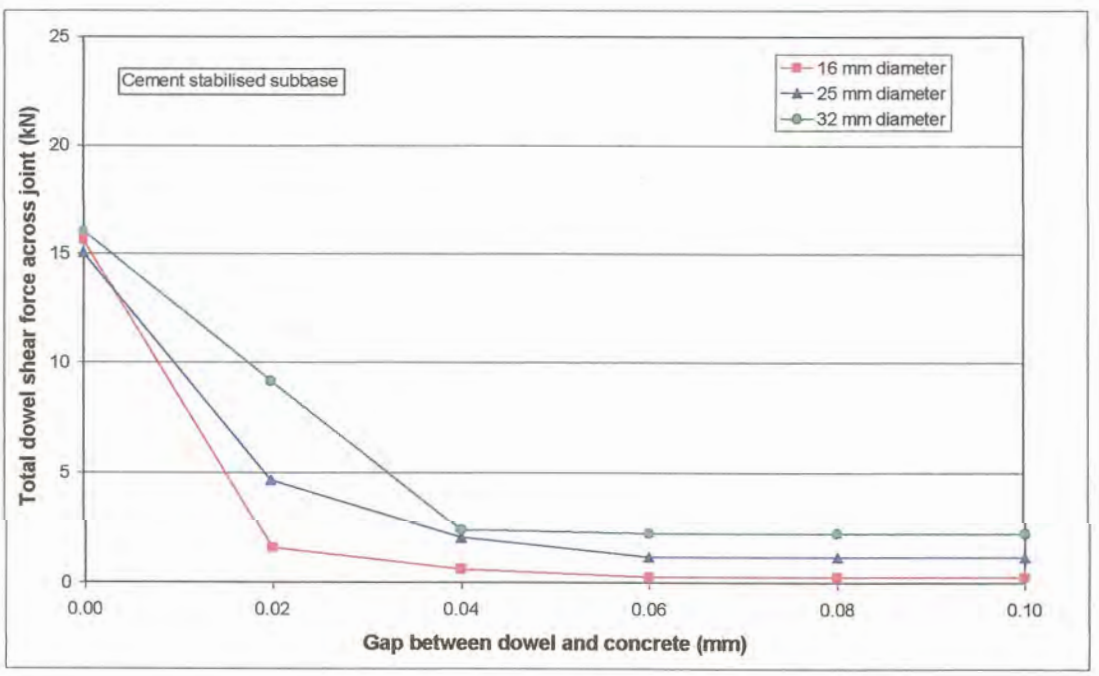

Figure D.25: Total shear force transferred across joint due to dowels (cement stabilised subbase)

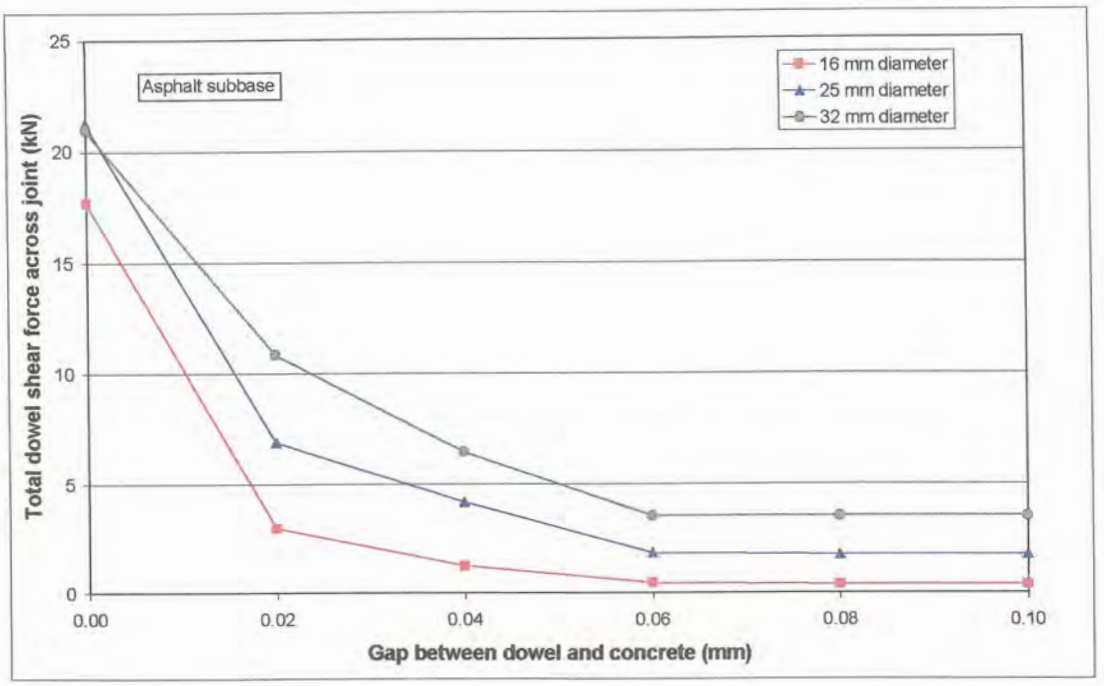

Figure D.26: Total shear force transferred across joint due to dowels (asphalt subbase)

To determine the effect of dowel spacing on the load transfer efficiency of the doweled slabs and on the shear force the dowels have to transfer across the joint, the above three sets of theoretical analyses were repeated with dowel bar spacing of 450, and 600 mm. The results of these analyses are presented below. It followed intuition that the load transfer efficiency would decrease with increasing dowel bar spacing for a constant dowel diameter. Similarly, the total shear load transferred across the joint through the dowels decreased for increasing dowel bar spacing for a specific dowel diameter, especially for the 16 mm diameter dowel bars. On the other hand, the total shear load transferred across the joint through the 25, and 32 mm diameter dowel bars at 600 mm spacing increased at 0 mm gap width in each case considered. This indicated that a too large dowel bar spacing can over-stress the dowel bars and cause it to fail.

D.4.1.2 Dowel bar spacing – 450 mm

Figures D.27 to D.29 present the deflection load transfer efficiency for 16, 25, and 32 mm diameter dowel bars at 450 mm spacing with increasing gap width around the dowels.

The total shear force transferred across the joint due to the dowels at increasing gap widths is presented in Figures D.30 to D.32.

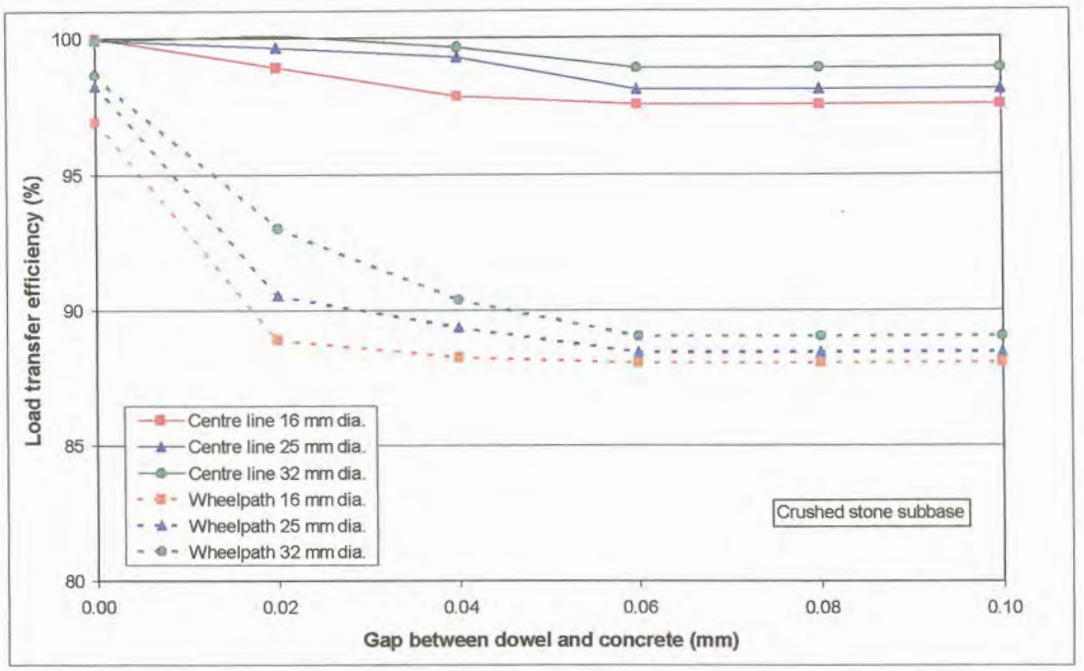

Figure D.27: Deflection load transfer efficiency with dowel bar spacing at 450 mm (crushed stone subbase)

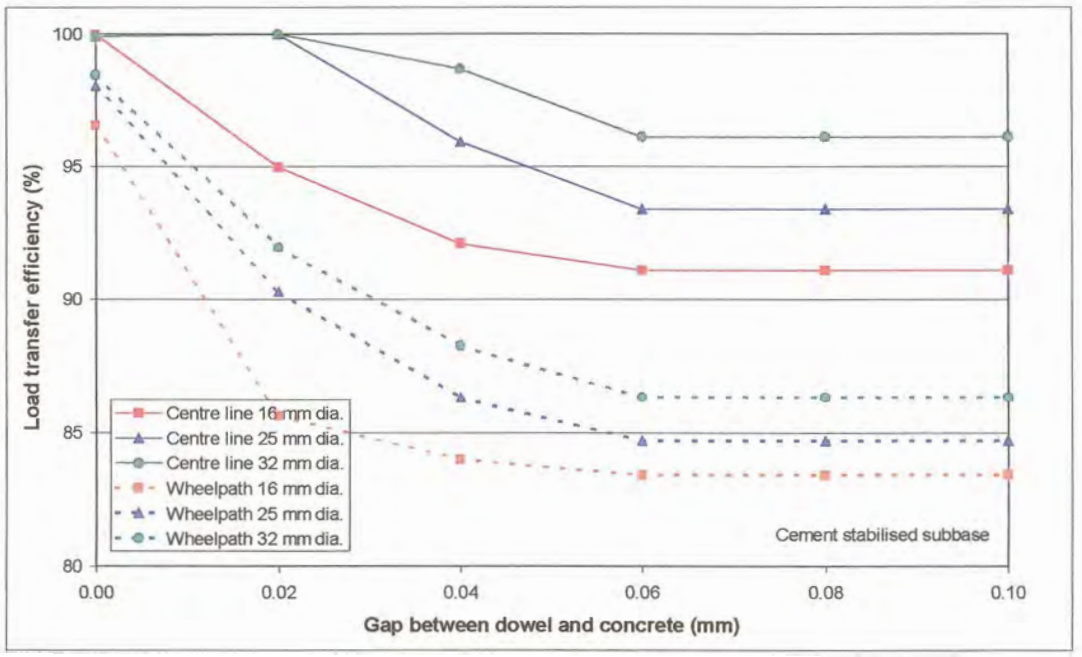

Figure D.28: Deflection load transfer efficiency with dowel bar spacing at 450 mm (cement stabilised subbase)

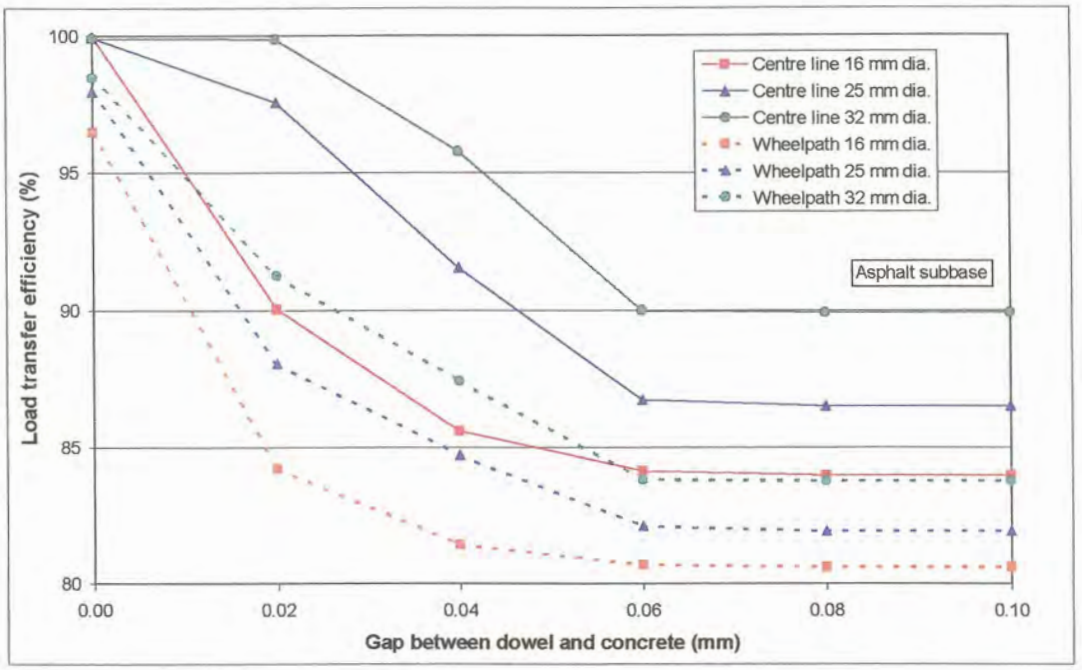

Figure D.29: Deflection load transfer efficiency with dowel bar spacing at 450 mm (asphalt subbase)

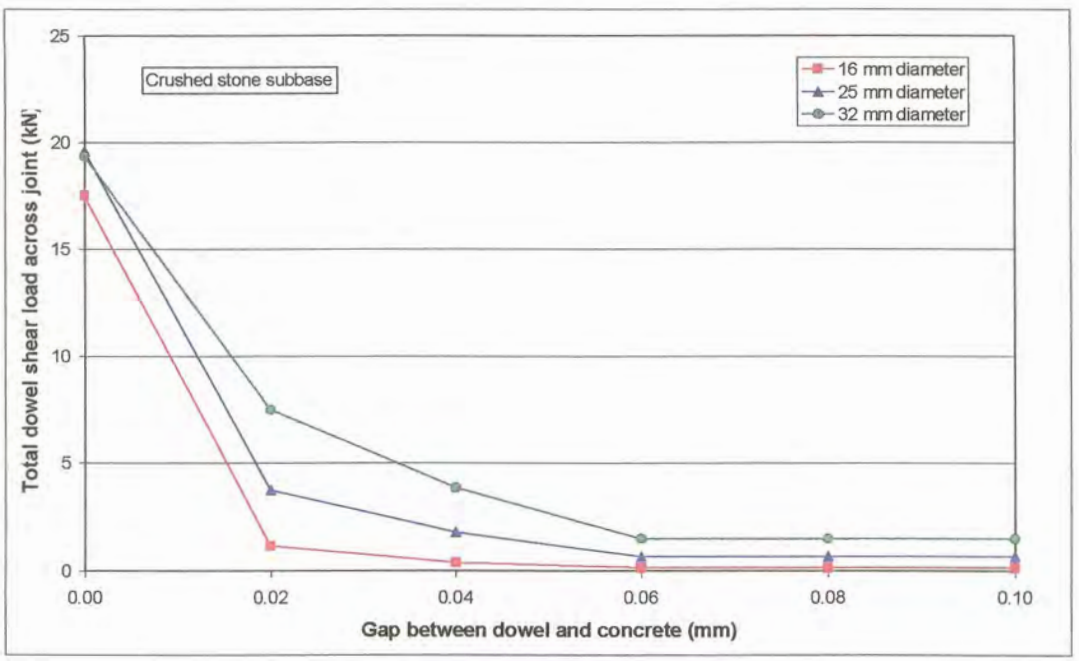

Figure D.30: Total shear load transferred across joint due to dowels with dowel bar spacing at 450 mm (crushed stone subbase)

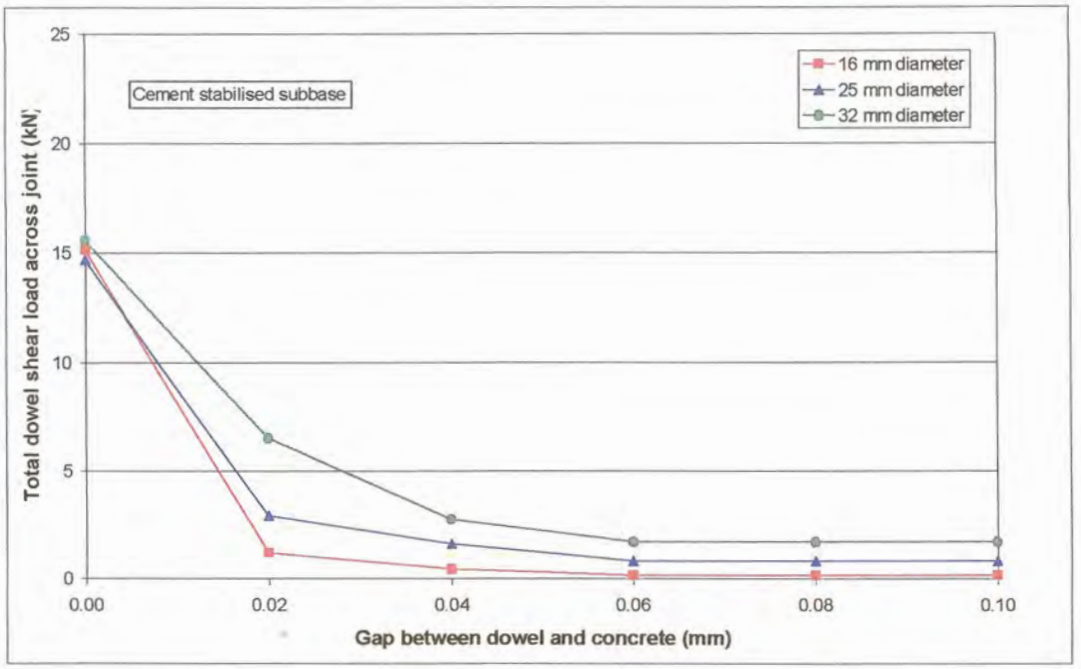

Figure D.31: Total shear load transferred across joint due to dowels with dowel bar spacing at 450 mm (cement stabilised subbase)

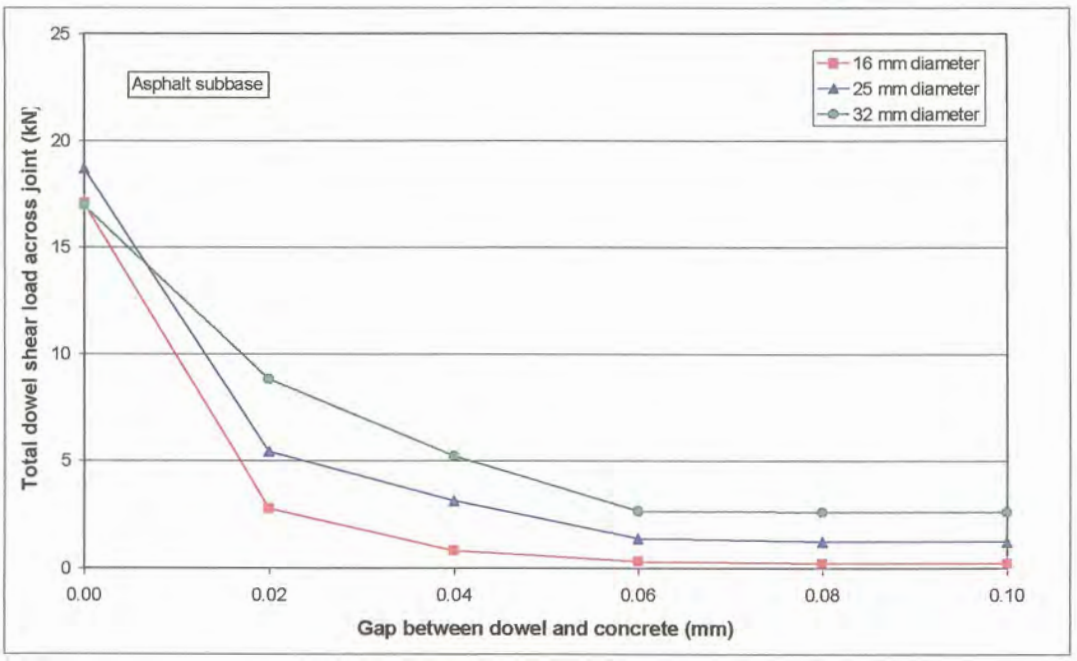

Figure D.32: Total shear load transferred across joint due to dowels with dowel bar spacing at 450 mm (asphalt subbase)

D.4.1.3 Dowel bar spacing – 600 mm

Figures D.33 to D.35 present the deflection load transfer efficiency for 16, 25, and 32 mm diameter dowel bars at 600 mm spacing with increasing gap width around the dowels.

The total shear force transferred across the joint due to the dowels at increasing gap widths is presented in Figures D.36 to D.38.

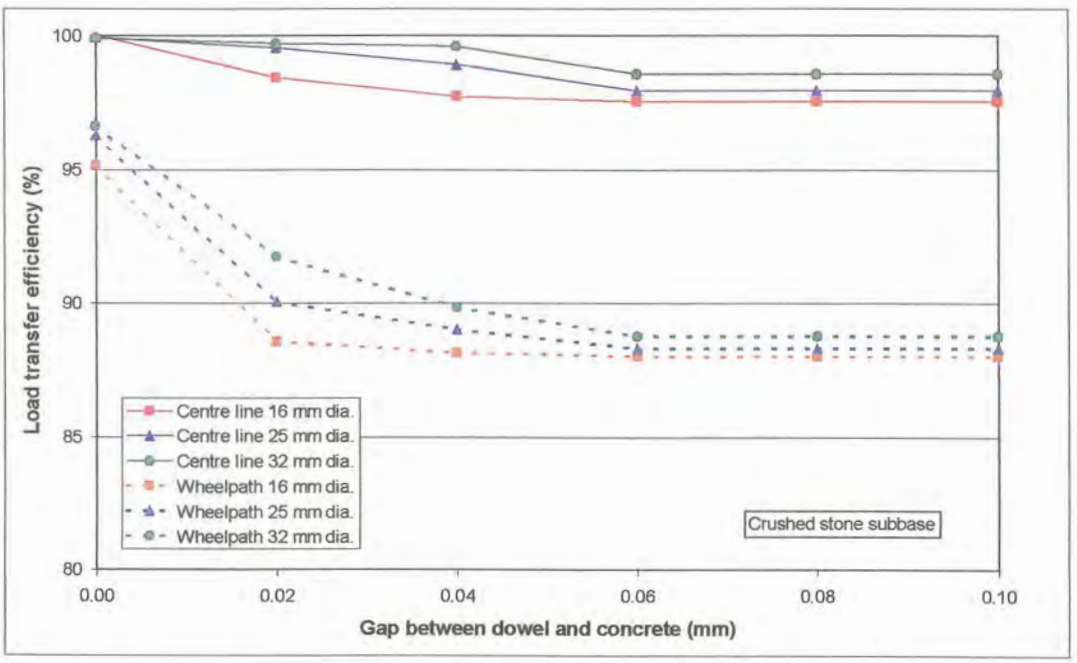

Figure D.33: Deflection load transfer efficiency with dowel bar spacing at 600 mm (crushed stone subbase)

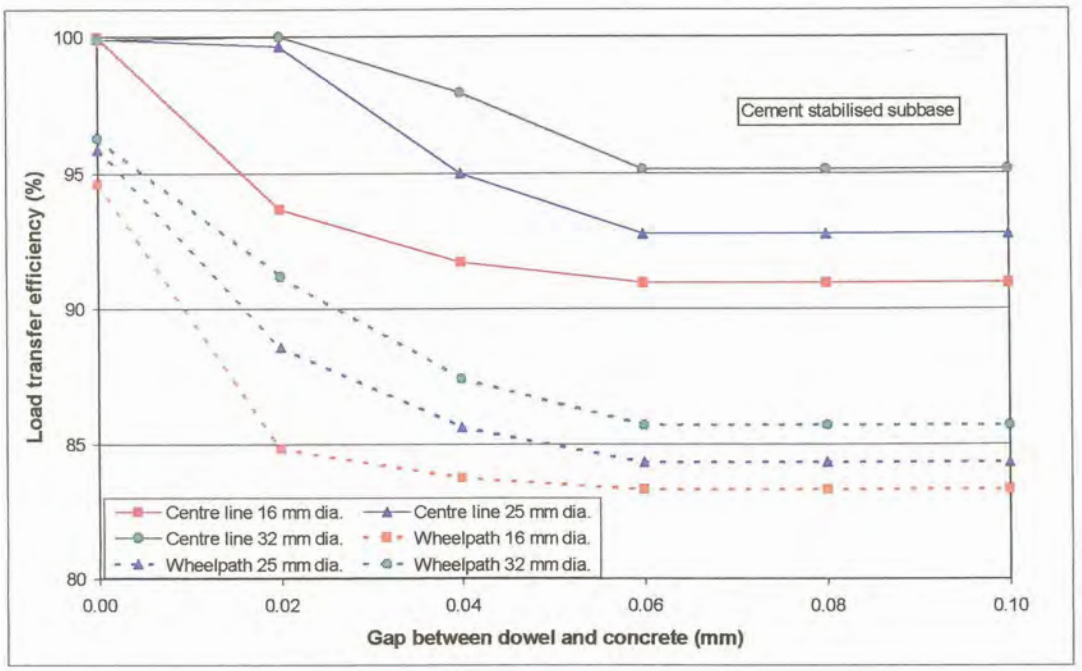

Figure D.34: Deflection load transfer efficiency with dowel bar spacing at 600 mm (cement stabilised subbase)

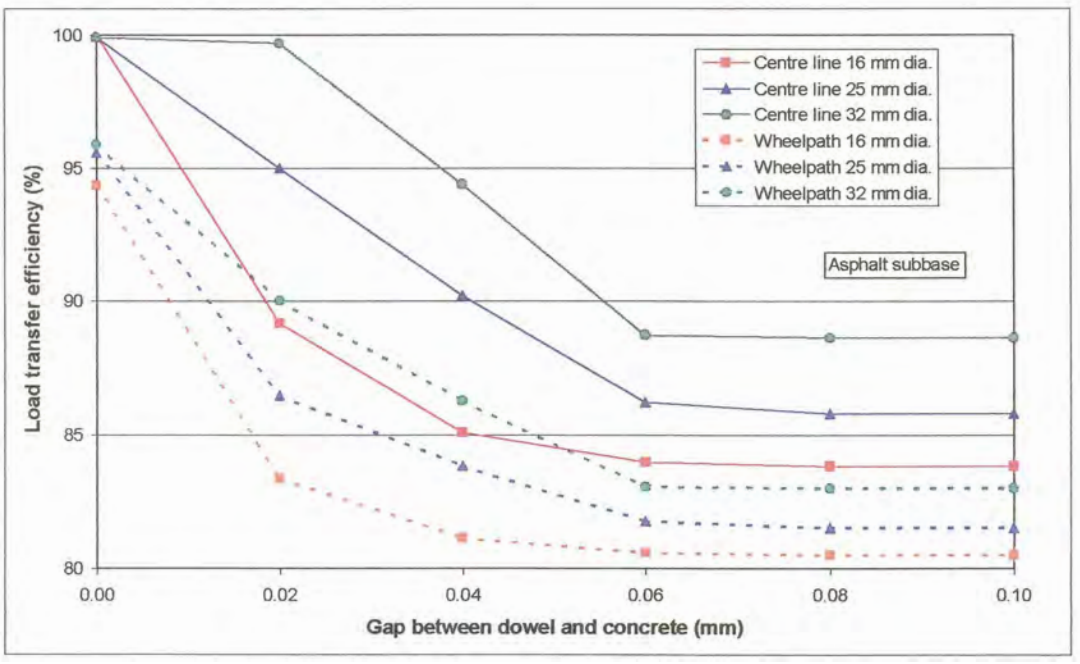

Figure D.35: Deflection load transfer efficiency with dowel bar spacing at 600 mm (asphalt subbase)

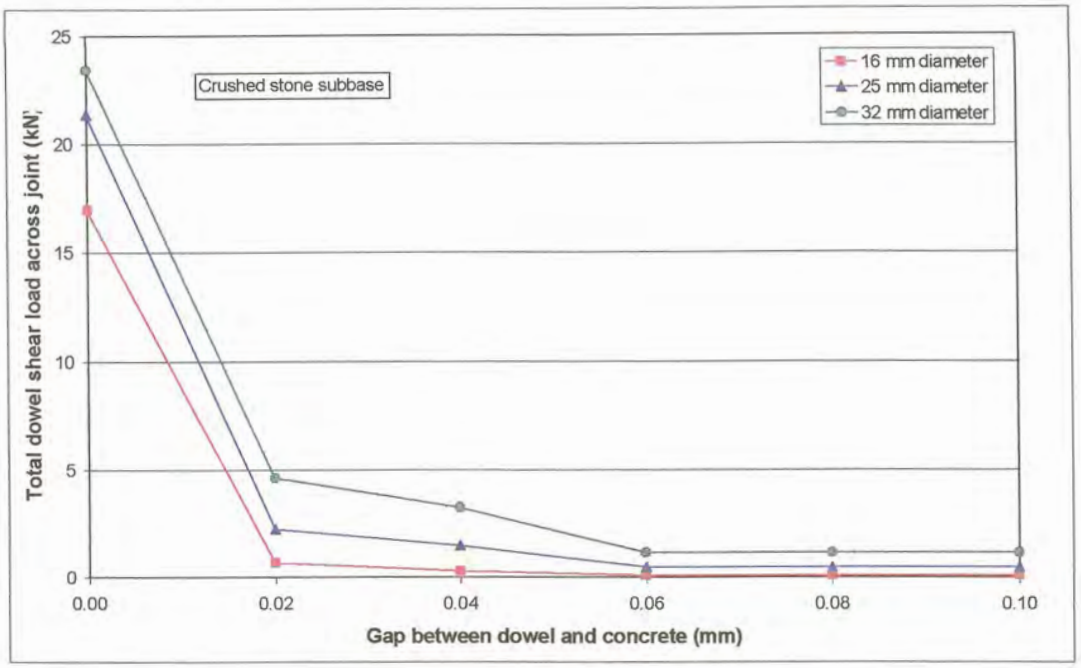

Figure D.36: Total shear load transferred across joint due to dowels with dowel bar spacing at 600 mm (crushed stone subbase)

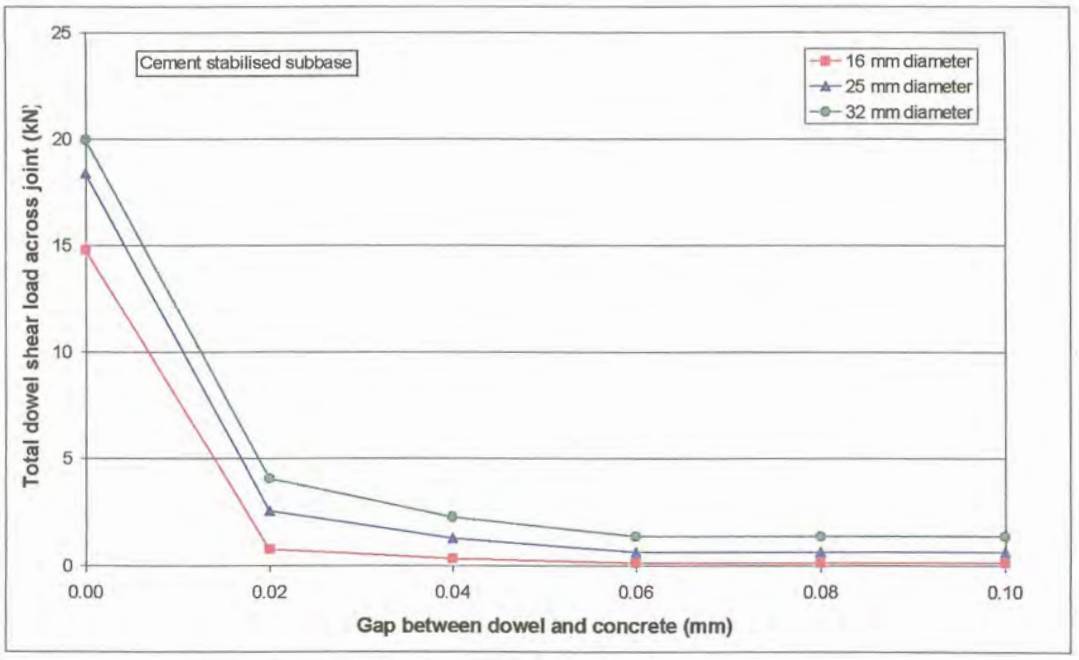

Figure D.37: Total shear load transferred across joint due to dowels with dowel bar spacing at 600 mm (cement stabilised subbase)

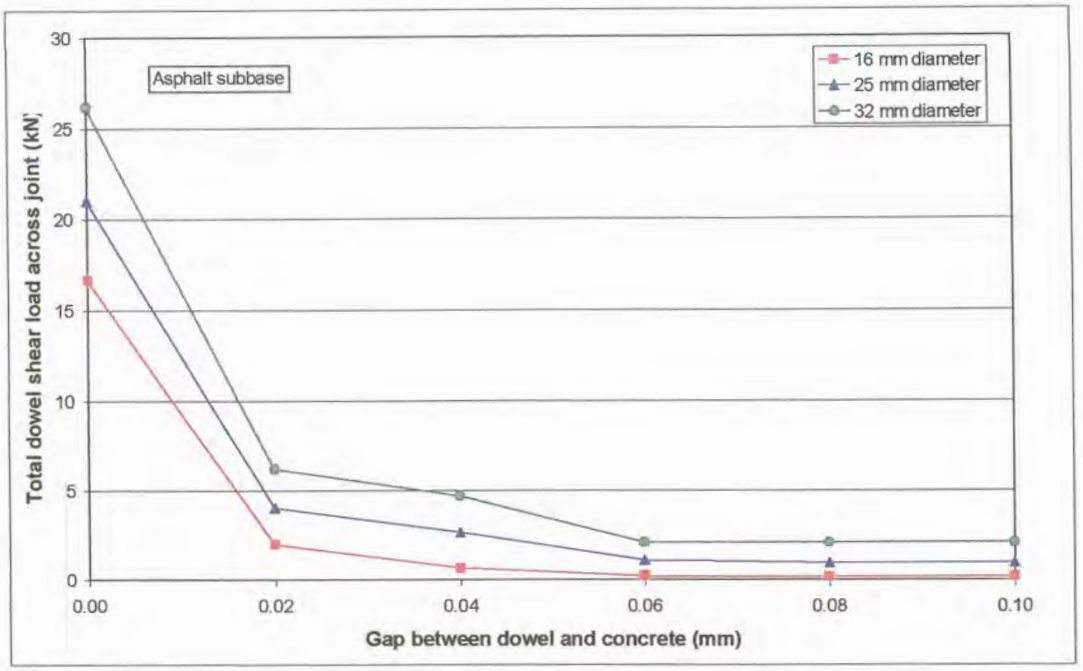

Figure D.38: Total shear load transferred across joint due to dowels with dowel bar spacing at 600 mm (asphalt subbase)

D.4.2 CONSTANT DOWEL BAR DIAMETER AT INCREASED DOWEL BAR SPACING

The effect of increasing the dowel bar spacing for a specific dowel bar diameter was also investigated. The results already obtained were regrouped for this purpose.

D.4.2.1 16 mm Diameter dowels

The deflection load transfer efficiency for 16 mm diameter dowel bars with increasing gap width between the dowel and the concrete at dowel bar spacings of 300, 450, and 600 mm, for each of the subbases considered, are presented in Figures D.39 to D.41. The deflection load transfer efficiency of an unloaded position, centre line (CL) was compared with that of a loaded position, wheelpath (WP).

Similarly the total shear load transferred across the joint through the dowels for 16 mm diameter dowels are presented in Figures D.42 to D.44.

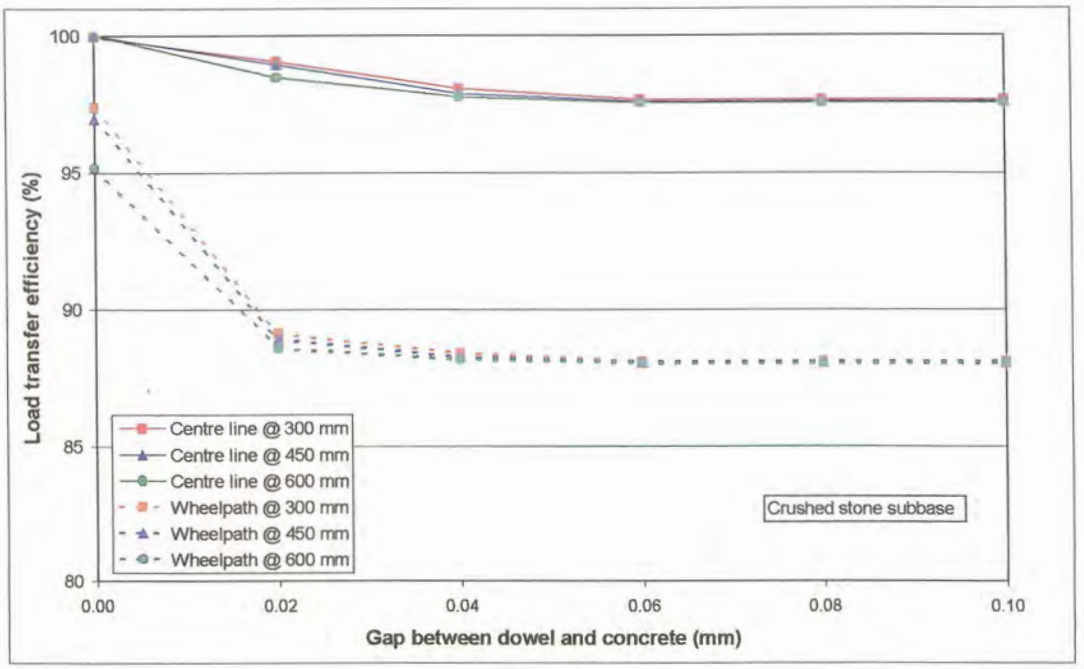

Figure D.39: Deflection load transfer efficiency for 16 mm diameter dowel bars at increased dowel bar spacing (crushed stone subbase)

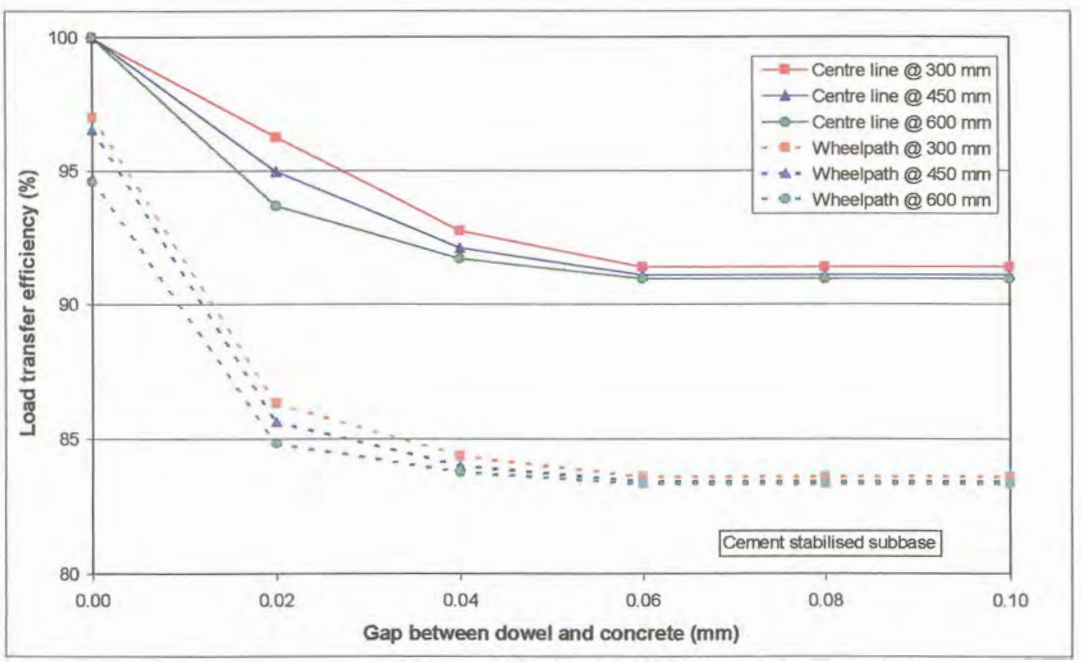

Figure D.40: Deflection load transfer efficiency for 16 mm diameter dowel bars at increased dowel bar spacing (cement stabilised subbase)

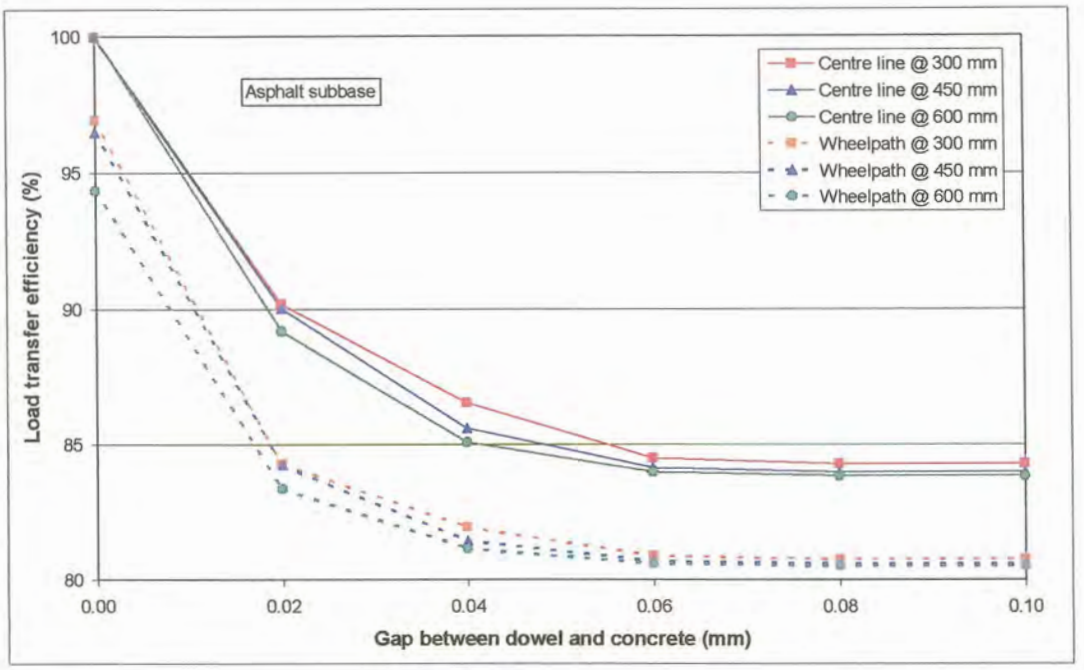

Figure D.41: Deflection load transfer efficiency for 16 mm diameter dowel bars at increased dowel bar spacing (asphalt subbase)

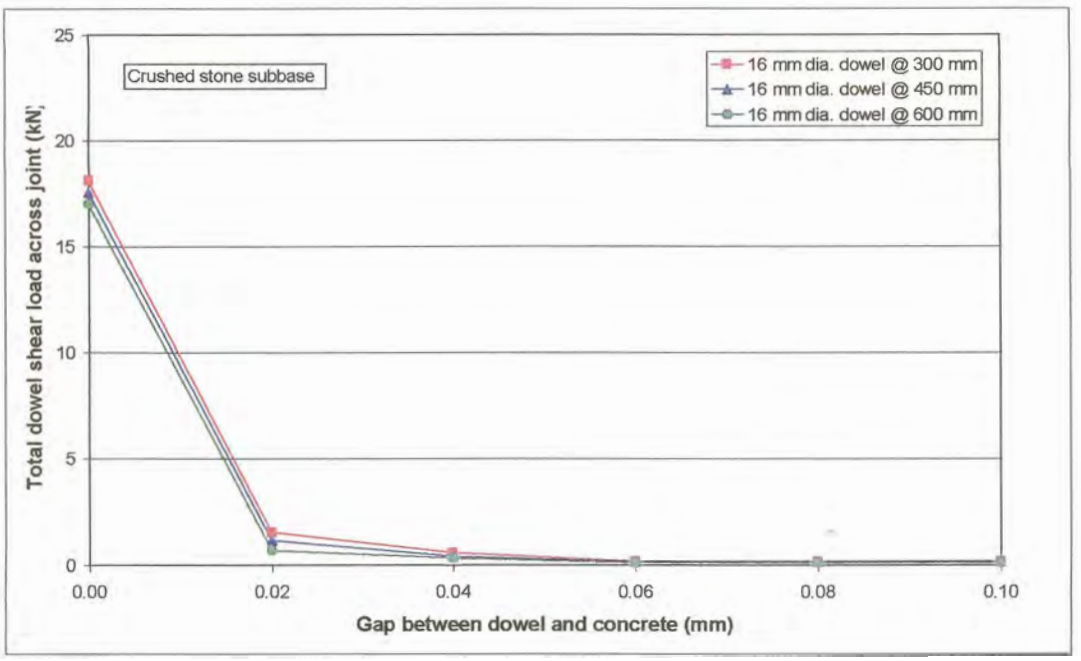

Figure D.42: Total shear load transferred across joint due to 16 mm diameter dowels with increased dowel bar spacing (crushed stone subbase)

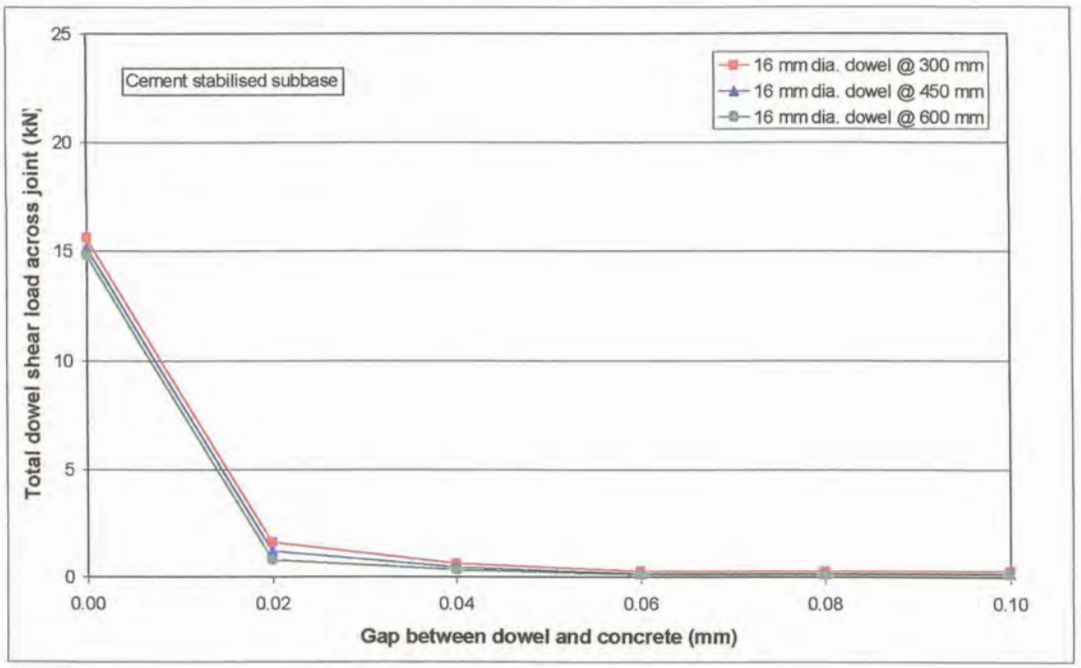

Figure D.43: Total shear load transferred across joint due to 16 mm diameter dowels with increased dowel bar spacing (cement stabilised subbase)

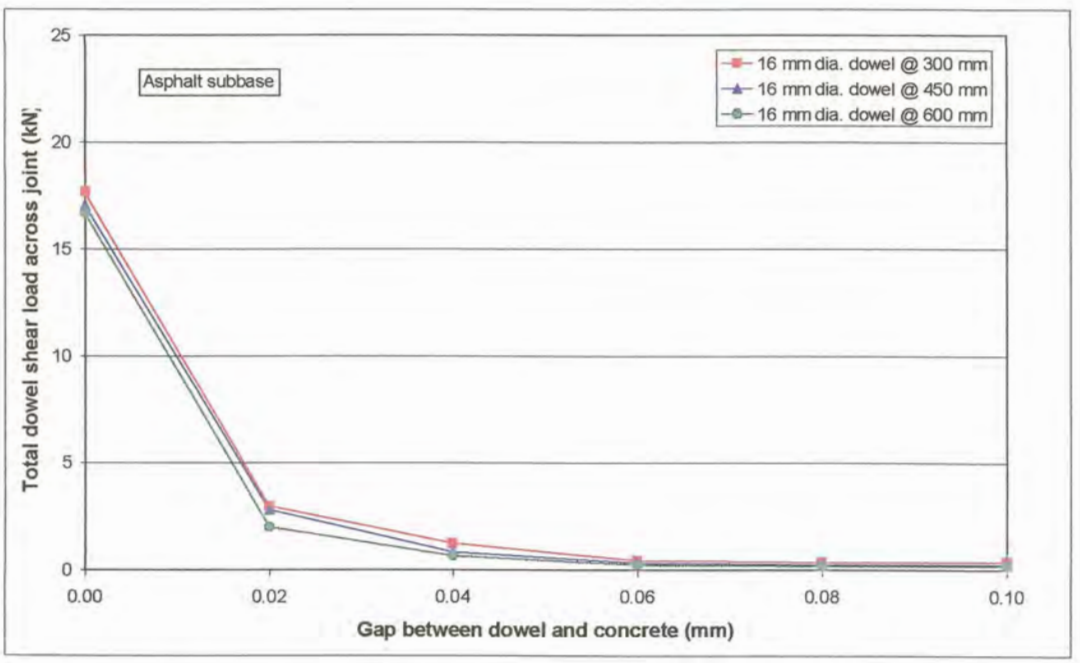

Figure D.44: Total shear load transferred across joint due to 16 mm diameter dowels with increased dowel bar spacing (asphalt subbase)

D.4.2.2 25 mm Diameter dowels

The deflection load transfer efficiency for 25 mm diameter dowel bars with increasing gap width between the dowel and the concrete at dowel bar spacings of 300, 450, and 600 mm, for each of the subbases considered, are presented in Figures D.45 to D.47. The deflection load transfer efficiency of an unloaded position, centre line (CL) was compared with that of a loaded position, wheel-path (WP).

Similarly the total shear load transferred across the joint through the dowels for 25 mm diameter dowels are presented in Figures D.48 to D.50.

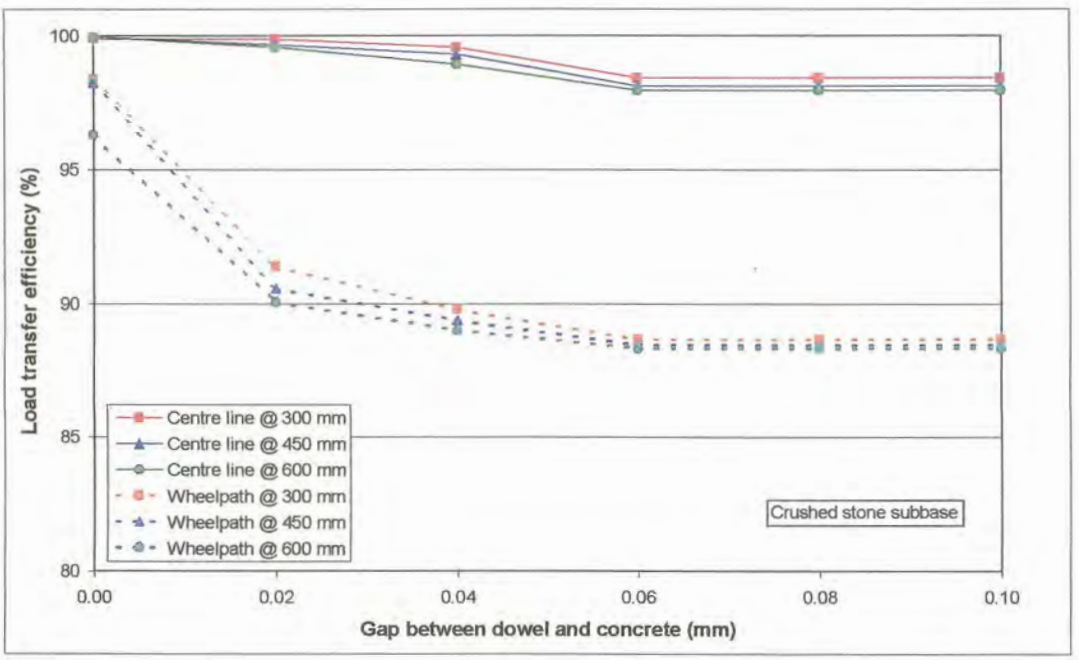

Figure D.45: Deflection load transfer efficiency for 25 mm diameter dowel bars at increased dowel bar spacing (crushed stone subbase)

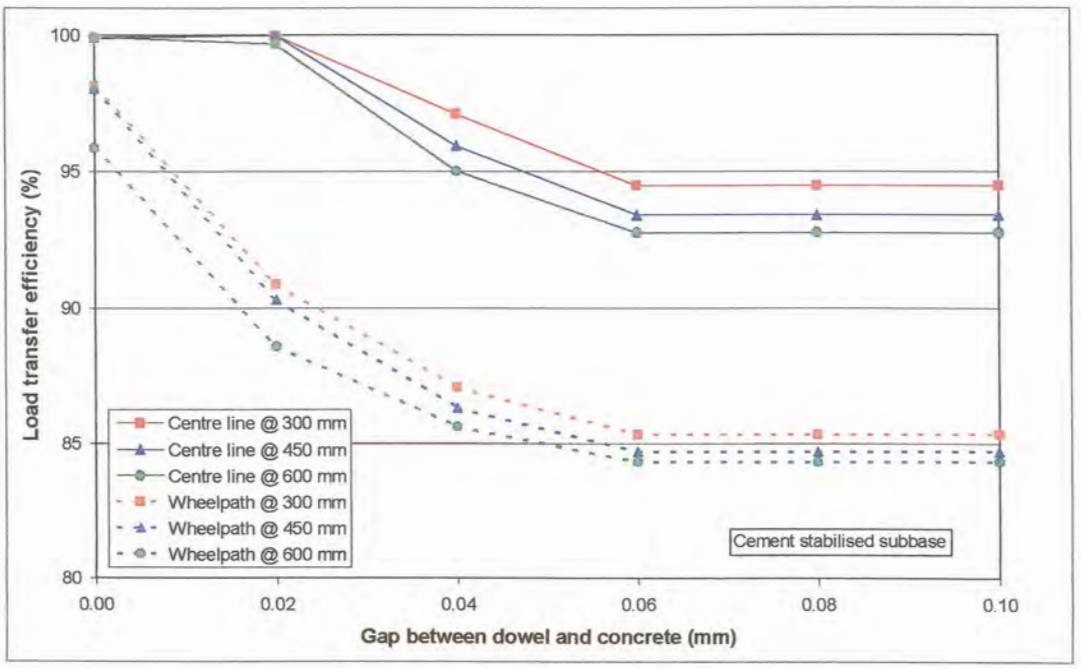

Figure D.46: Deflection load transfer efficiency for 25 mm diameter dowel bars at increased dowel bar spacing (cement stabilised subbase)

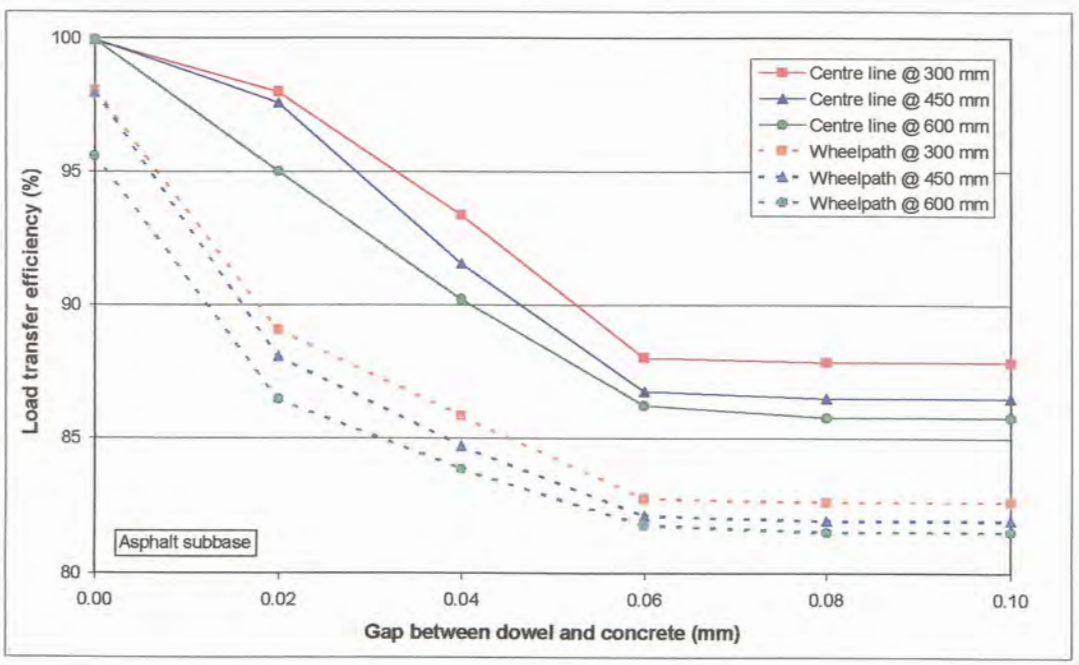

Figure D.47: Deflection load transfer efficiency for 25 mm diameter dowel bars at increased dowel bar spacing (asphalt subbase)

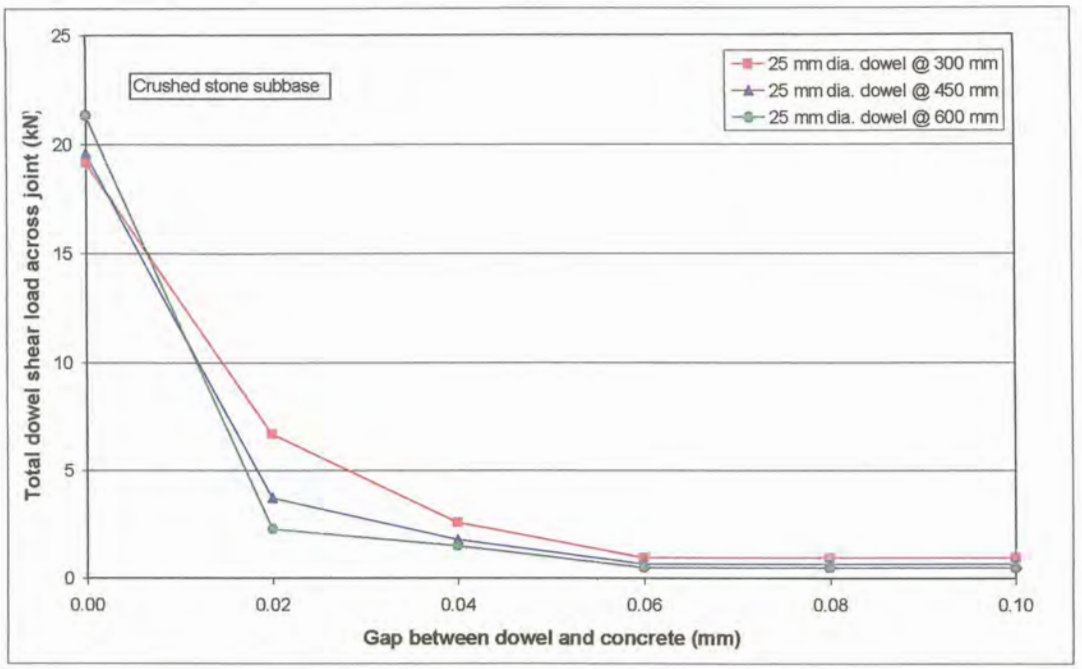

Figure D.48: Total shear load transferred across joint due to 25 mm diameter dowels with increased dowel bar spacing (crushed stone subbase)

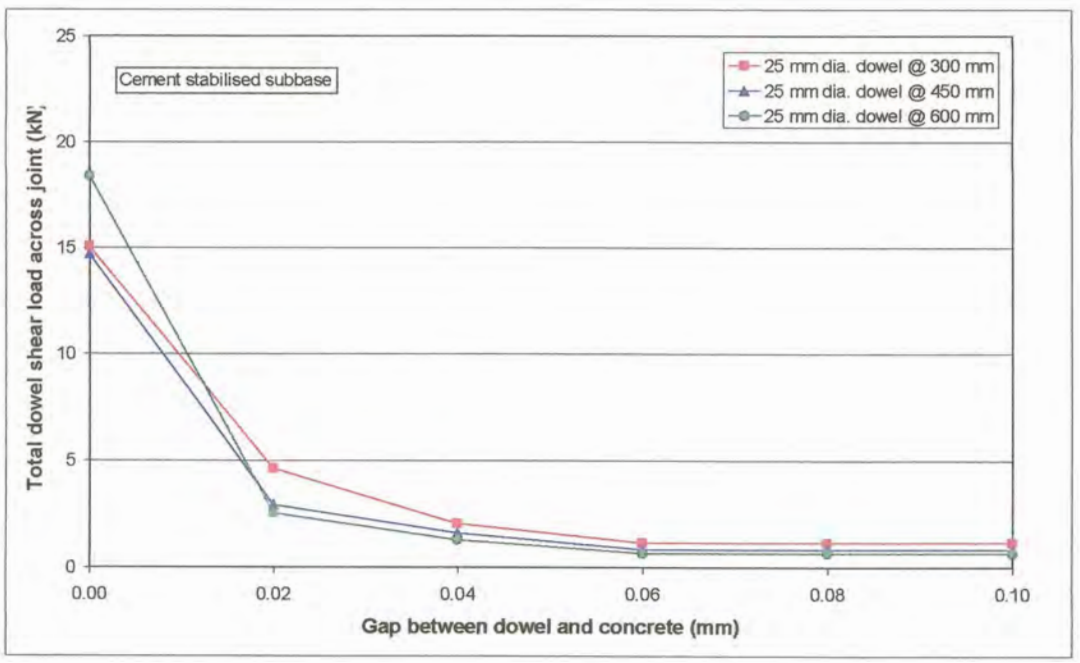

Figure D.49: Total shear load transferred across joint due to 25 mm diameter dowels with increased dowel bar spacing (cement stabilised subbase)

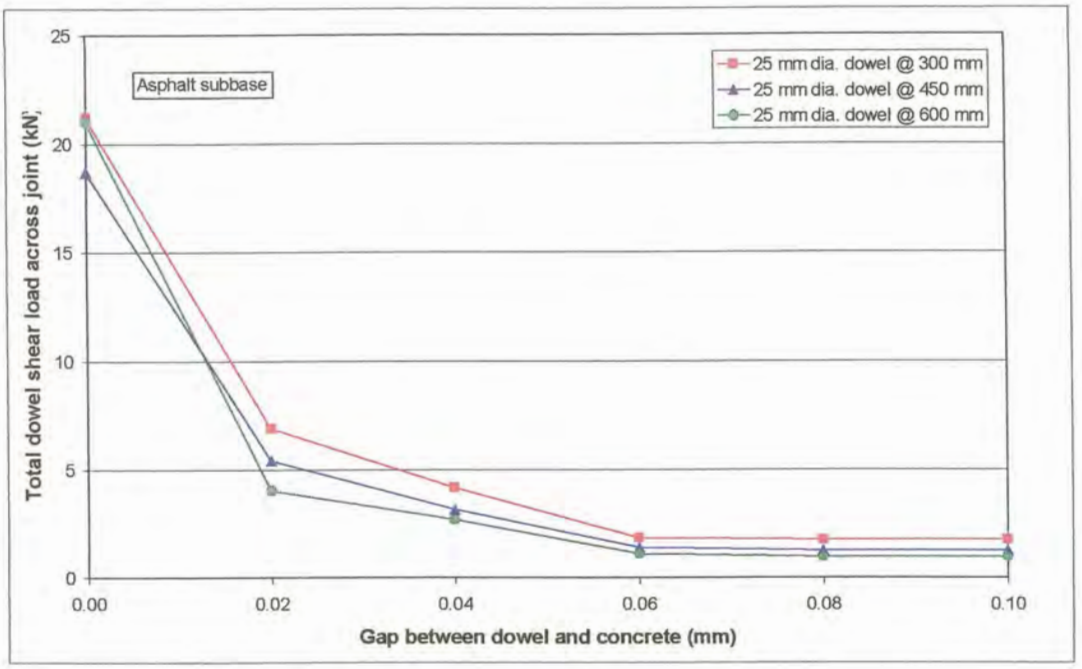

Figure D.50: Total shear load transferred across joint due to 25 mm diameter dowels with increased dowel bar spacing (asphalt subbase)

D.4.2.3 32 mm Diameter dowels

The deflection load transfer efficiency for 32 mm diameter dowel bars with increasing gap width between the dowel and the concrete at dowel bar spacings of 300, 450, and 600 mm, for each of the subbases considered, are presented in Figures D.51 to D.53. The deflection load transfer efficiency of an unloaded position, centre line (CL) was compared with that of a loaded position, wheel-path (WP).

Similarly the total shear load transferred across the joint through the dowels for 32 mm diameter dowels are presented in Figures D.54 to D.56.

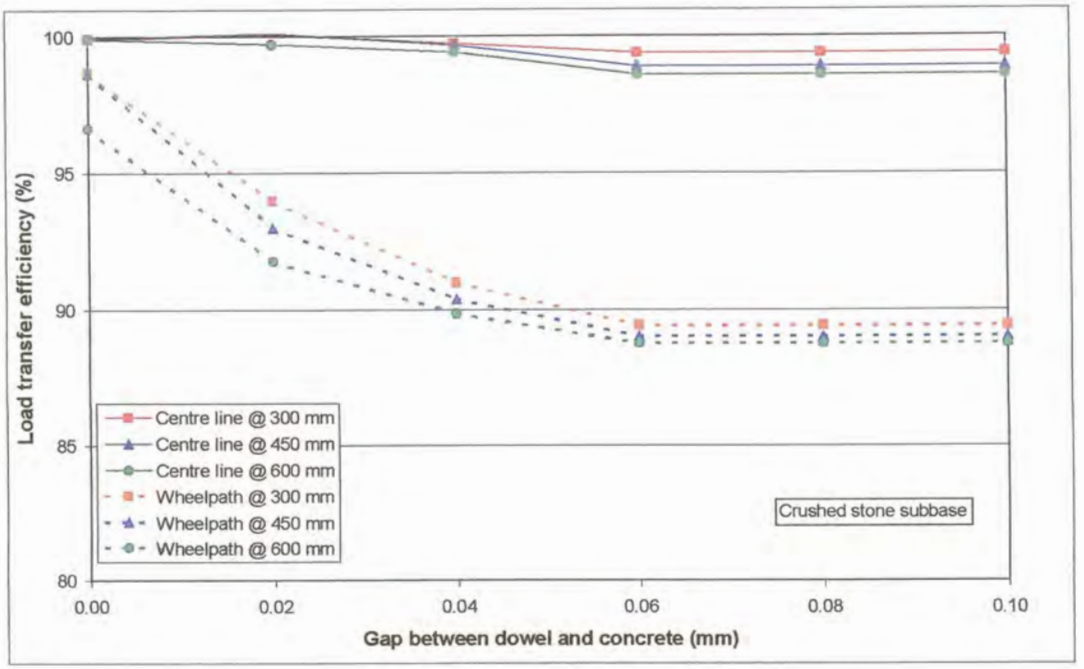

Figure D.51: Deflection load transfer efficiency for 32 mm diameter dowel bars at increased dowel bar spacing (crushed stone subbase)

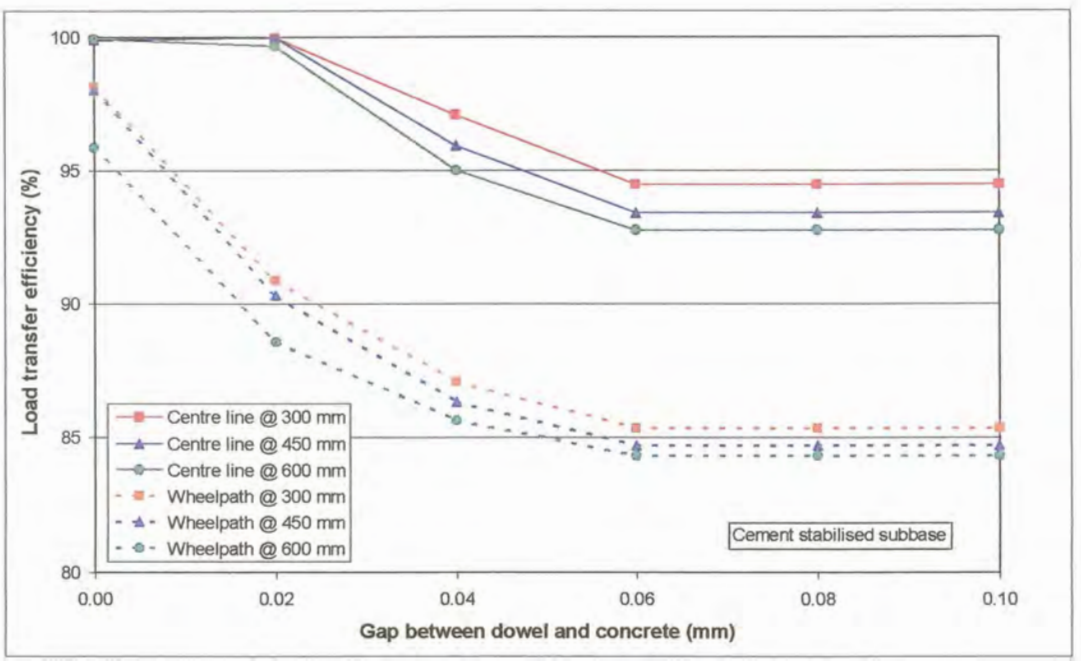

Figure D.52: Deflection load transfer efficiency for 32 mm diameter dowel bars at increased dowel bar spacing (cement stabilised subbase)

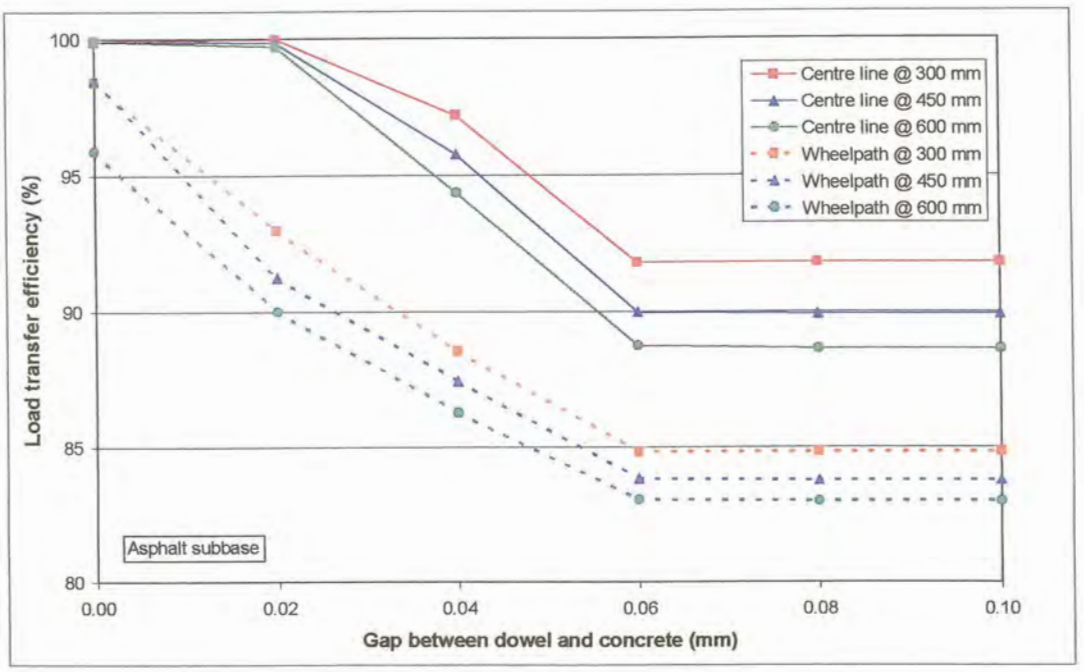

Figure D.53: Deflection load transfer efficiency for 32 mm diameter dowel bars at increased dowel bar spacing (asphalt subbase)

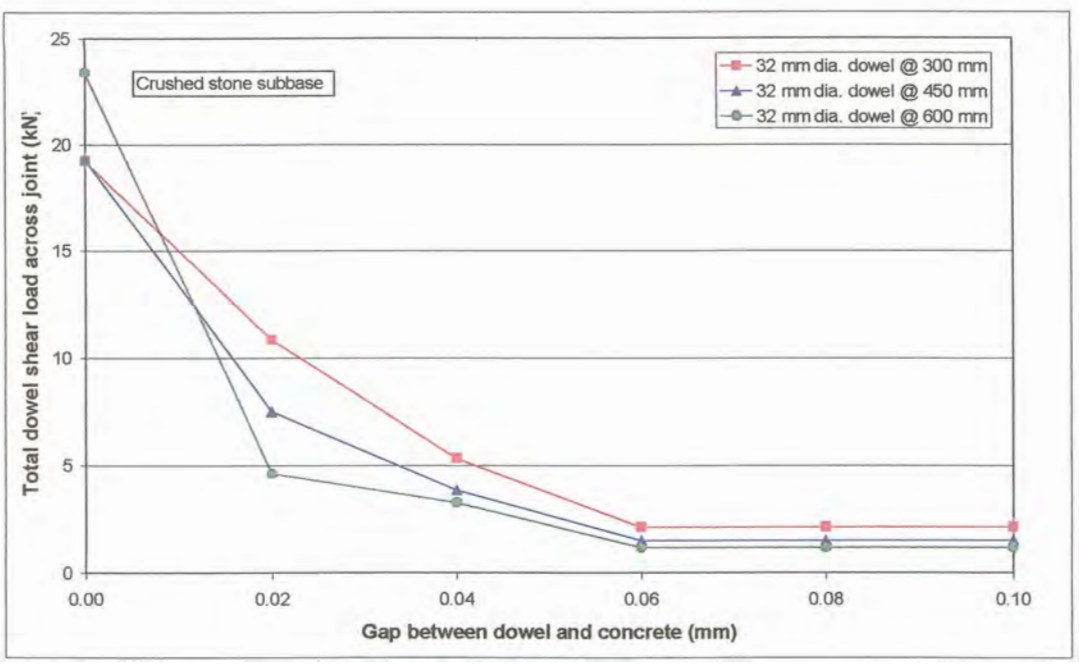

Figure D.54: Total shear load transferred across joint due to 32 mm diameter dowels with increased dowel bar spacing (crushed stone subbase)

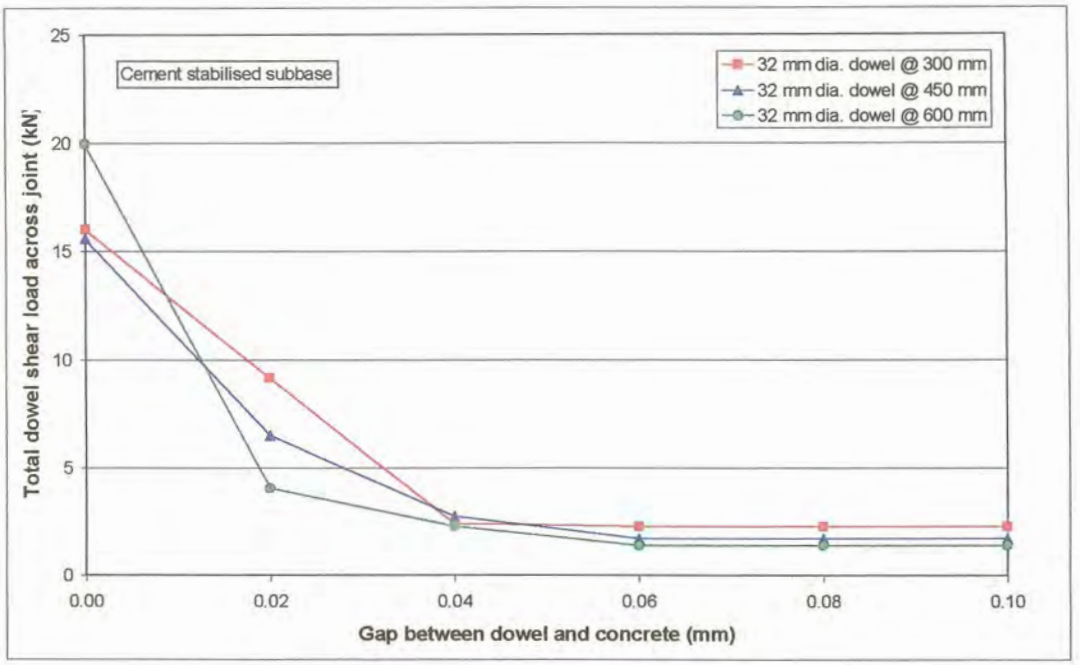

Figure D.55: Total shear load transferred across joint due to 32 mm diameter dowels with increased dowel bar spacing (cement stabilised subbase)

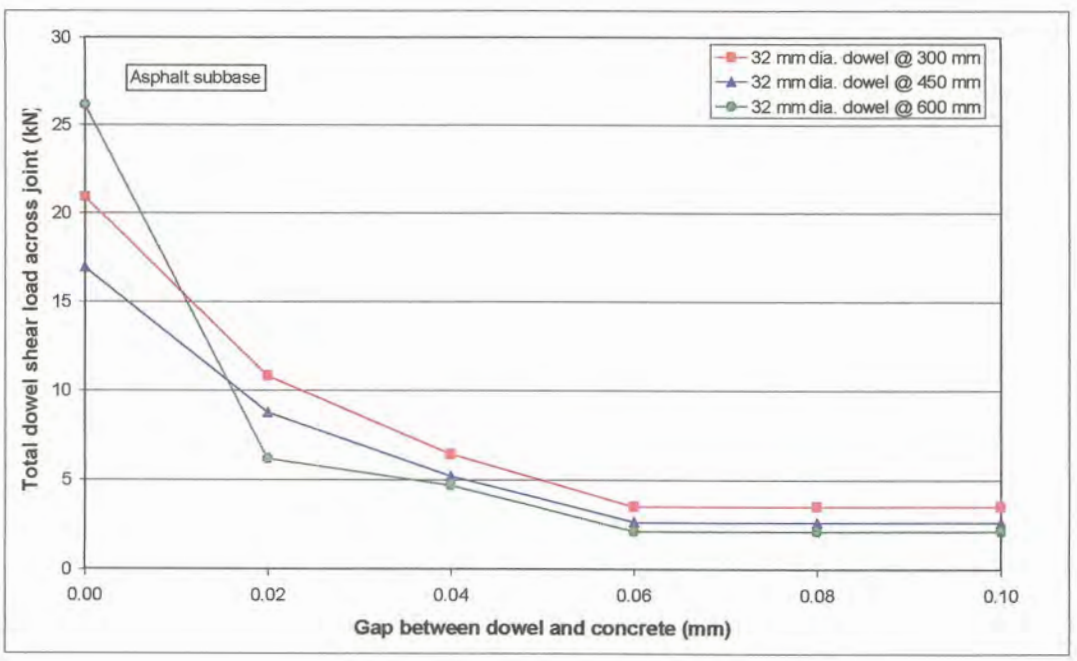

Figure D.56: Total shear load transferred across joint due to 32 mm diameter dowels with increased dowel bar spacing (asphalt subbase)

D.5 COMBINED AGGREGATE INTERLOCK AND DOWEL MODELLING

Soroushian et al (1988) investigated the combined effect of aggregate interlock and dowel action in reinforced concrete beam elements against sliding shear at a crack. Algorithms were developed for predicting the aggregate interlock constitutive behaviour using some empirical formulations. They concluded that at very small sliding-shear deformations (below 0,2 mm) the dowel action tended to dominate the shear resistance. At larger deformations, however, the aggregate interlock became more dominant. At sliding-shear deformations greater than 0,7 mm, about 65% of the total shear resistance in the case studied was provided by aggregate interlock. One of the results of their tests is given in Figure D.57.

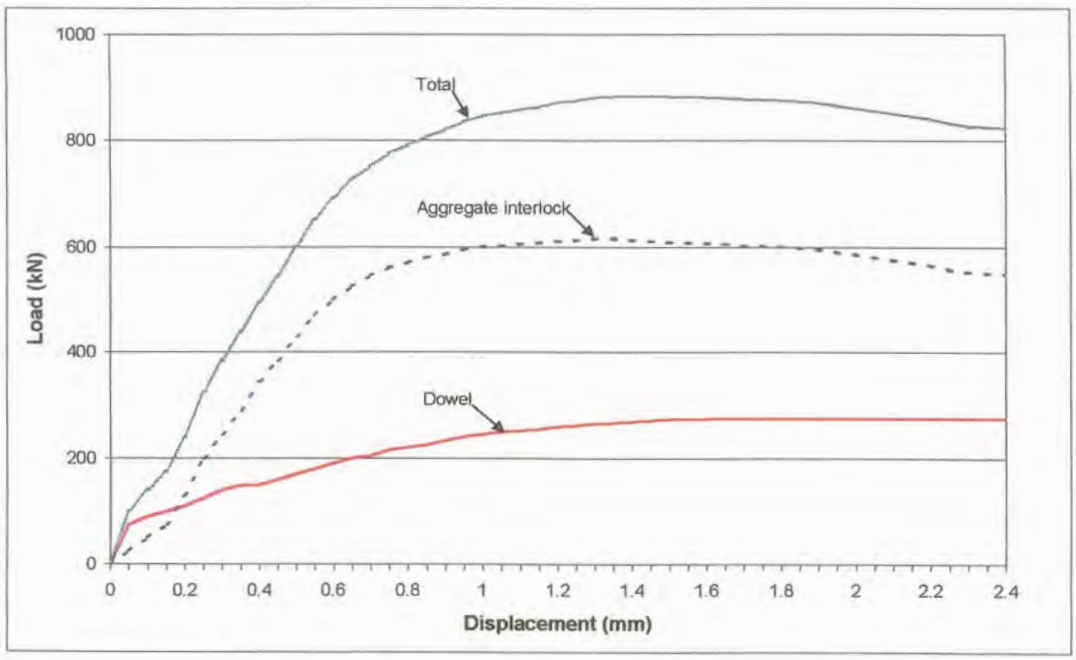

Figure D.57: Sliding shear behaviour at a constant crack width of 0,5 mm (Soroushian et al, 1988)

The combined effect of aggregate interlock and dowel action was also determined with EverFE. The same model as the one used in aggregate interlock modelling (par. D.3) with a cement stabilised subbase was used. To determine the effect of dowels in the model, 16 mm diameter dowels at 300 mm spacing were placed across the joint. During theoretical modelling the crack width was varied, while the gap around the dowel was kept constant.

The deflection load transfer efficiency obtained for 9 mm and 63 mm aggregate sizes are presented in Figure D.58. From this figure, it is obvious that the combined efficiency of aggregate interlock and dowels is far greater than for aggregate interlock only.

The maximum aggregate interlock shear stress measured in the wheel path was less for the combined aggregate interlock and dowel action models than for the models relying on aggregate interlock only (see Figure D.59). This could be ascribed to the dowels relieving some of the stress in the aggregate.

Just as for the shear stress, the total aggregate interlock shear force transferred across the joint was also less for the combined model than for the aggregate interlock model, as can be seen from Figure D.60.

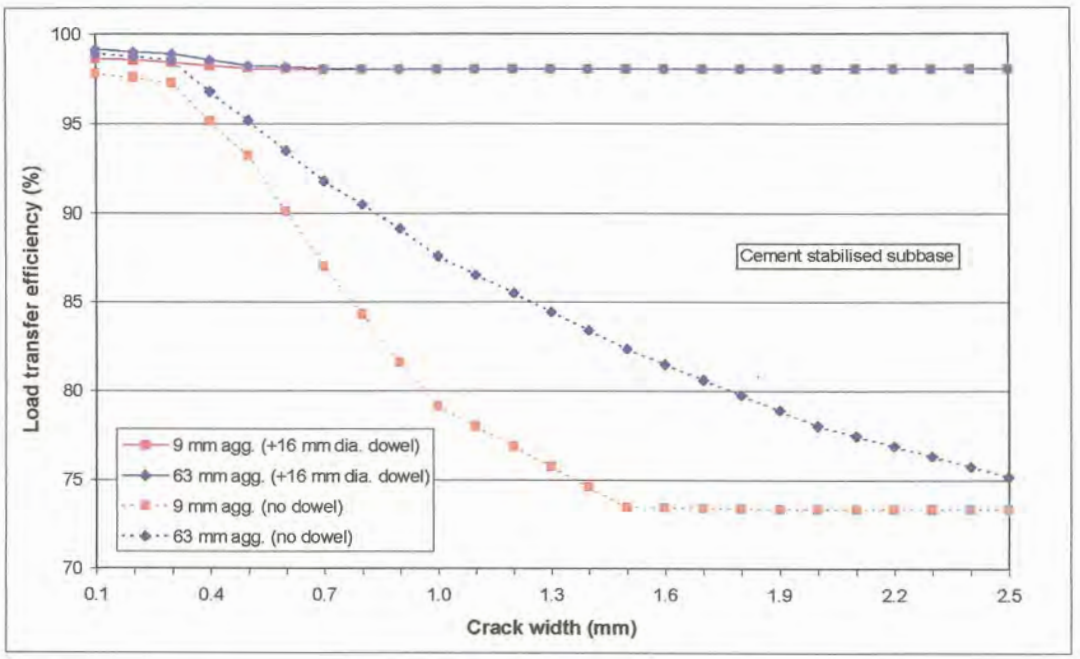

Figure D.58: Deflection load transfer efficiency in the wheel path – aggregate interlock versus combined effect of aggregate interlock and dowel action (no gap around dowel)

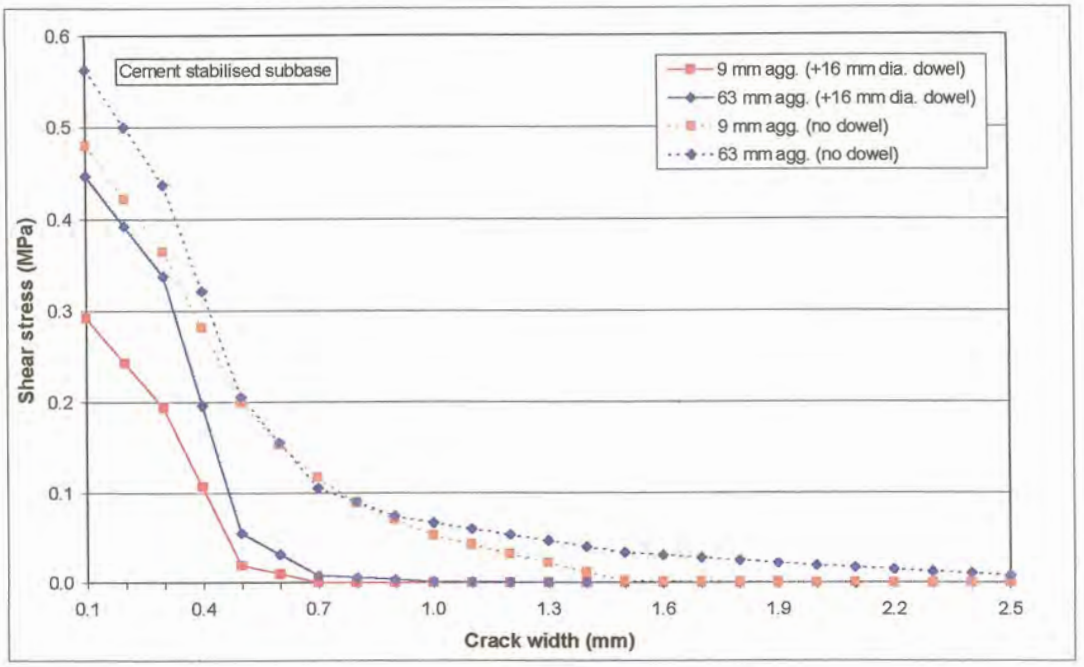

Figure D.59: Maximum shear stress at joint in wheel path – aggregate interlock versus combined effect of aggregate interlock and dowel action (no gap around dowel)

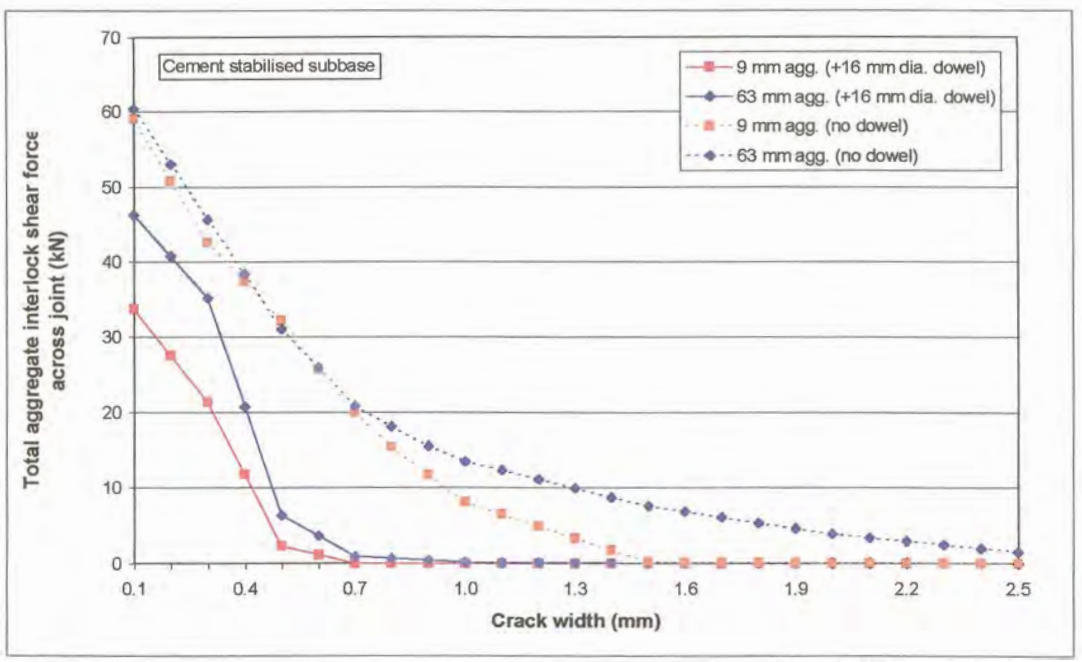

Figure D.60: Total shear force transferred across joint – aggregate interlock versus combined effect of aggregate interlock and dowel action (no gap around dowel)

The total shear force transferred across the crack due to dowel action was plotted on Figure D.61 together with the shear force transferred due to aggregate interlock for 9 mm and 63 mm maximum aggregate sizes. From this figure it could be concluded that aggregate interlock was initially the main factor contributing to the transfer of shear forces across a joint. However, the forces transferred due to aggregate interlock decreased rapidly, and was already close to zero at 0,7 mm crack width. On the other hand, the shear force transferred across the joint due to dowel action was initially (at 0,1 mm crack width) approximately 45% and 17% of the aggregate interlock shear force transferred for 9 mm and 63 mm aggregate sizes, respectively. Where after it decreased slightly and then increased to become the main contributing factor to the transfer of shear forces across the joint at 0,7 mm crack width. The forces transferred through the dowels at small crack widths for the 63 mm aggregate was less than for the 9 mm aggregate, due to the greater efficiency of the larger aggregate size.

Figures D.62 and D.63 present the total shear force transferred across the joint obtained by summing the forces due to aggregate interlock and dowel action for 9 mm and 63 mm maximum size aggregate, respectively.

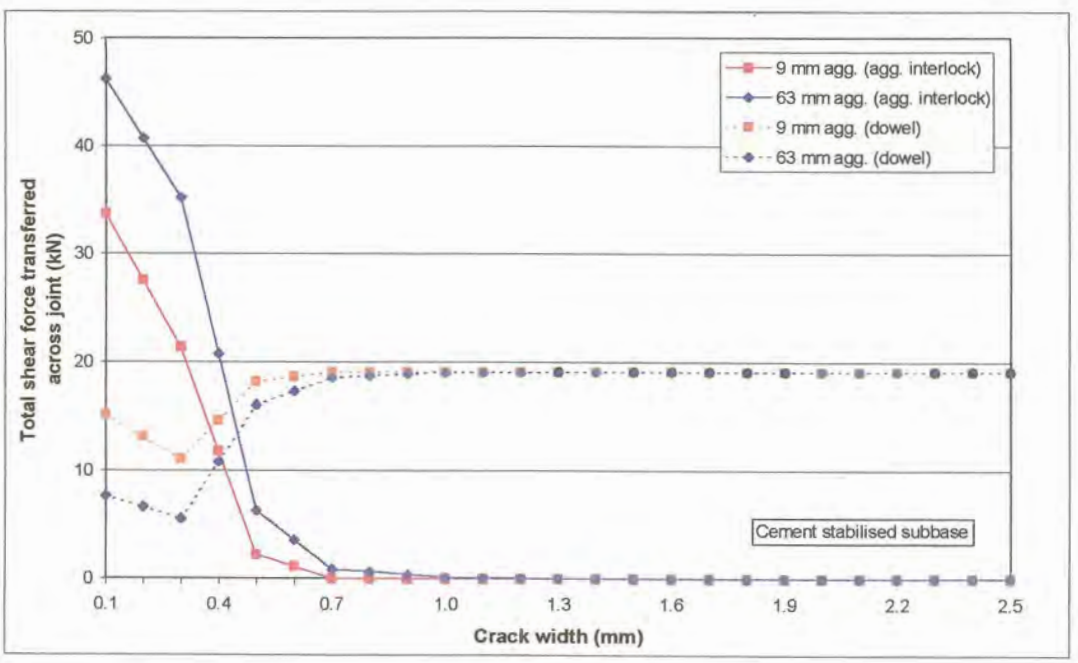

Figure D.61: Total shear force transferred across joint – combined effect of aggregate interlock and dowel action (no gap around dowel)

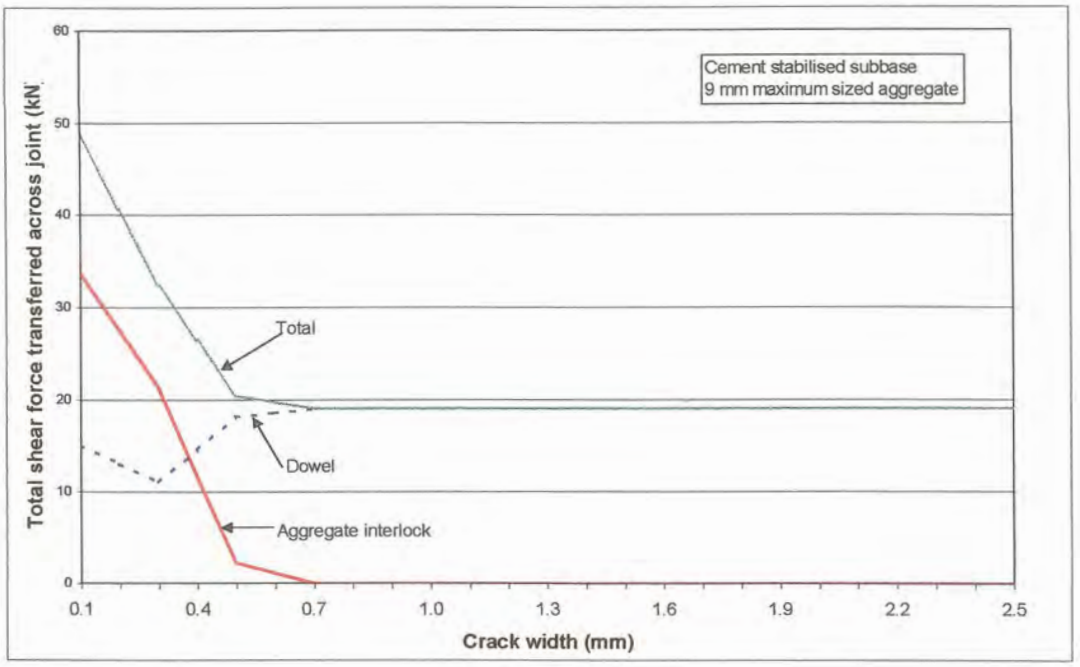

Figure D.62: Total shear force transferred across joint – 9 mm maximum sized aggregate – combined effect of aggregate interlock and dowel action (no gap around dowel)

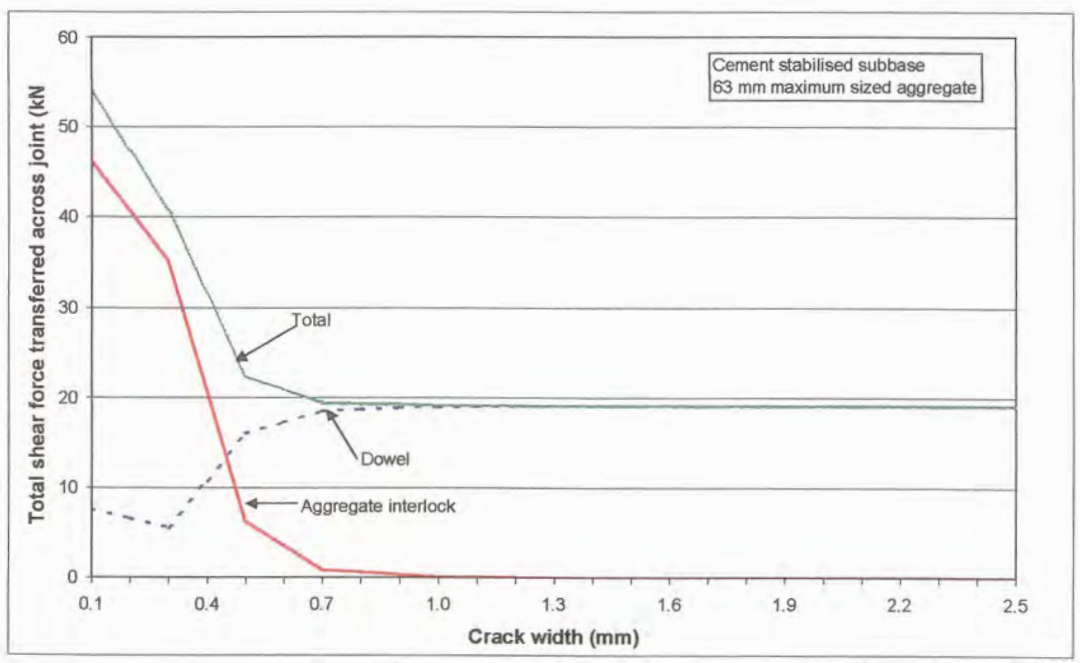

Figure D.63: Total shear force transferred across joint – 63 mm maximum sized aggregate – combined effect of aggregate interlock and dowel action (no gap around dowel)

The above theoretical analysis where the combined effect of aggregate interlock and dowel action was determined with EverFE, while varying the crack width, but keeping the gap around the dowel at zero, was repeated but in this instance, the gap around the dowel was also varied from 0,00 mm to 0,10 mm as described in paragraph D.3. The same model as the one used in aggregate interlock modelling (par. D.2) with a cement stabilised subbase was used. To determine the effect of dowels in the model, 16 mm diameter dowels at 300 mm spacing were placed across the joint.

The deflection load transfer efficiency obtained for 9 mm and 63 mm aggregate sizes and increasing gap sizes around the dowel bars are presented in Figures D.64 and D.65, respectively. From these figures, it is obvious that the bigger the gap around the dowel, the lower the load transfer efficiency. For comparison purposes, the values obtained for a joint relying on aggregate interlock only (no dowel), was also plotted on the graph. At a gap of 0,10 mm the load transfer efficiency approximated that of the "no dowel" case, which indicated that the dowel did not fulfil its purpose any more. This emphasised the importance of considering a gap around the dowel as well.

The development of maximum aggregate interlock shear stress relationships with increasing gap width around the dowel, measured in the wheel path for both 9 mm and 63 mm maximum aggregate sizes, are presented in detail in Figures D.66 to D.77. Once again, it is significant to note that the relationships obtained approximated the "no dowel" case.

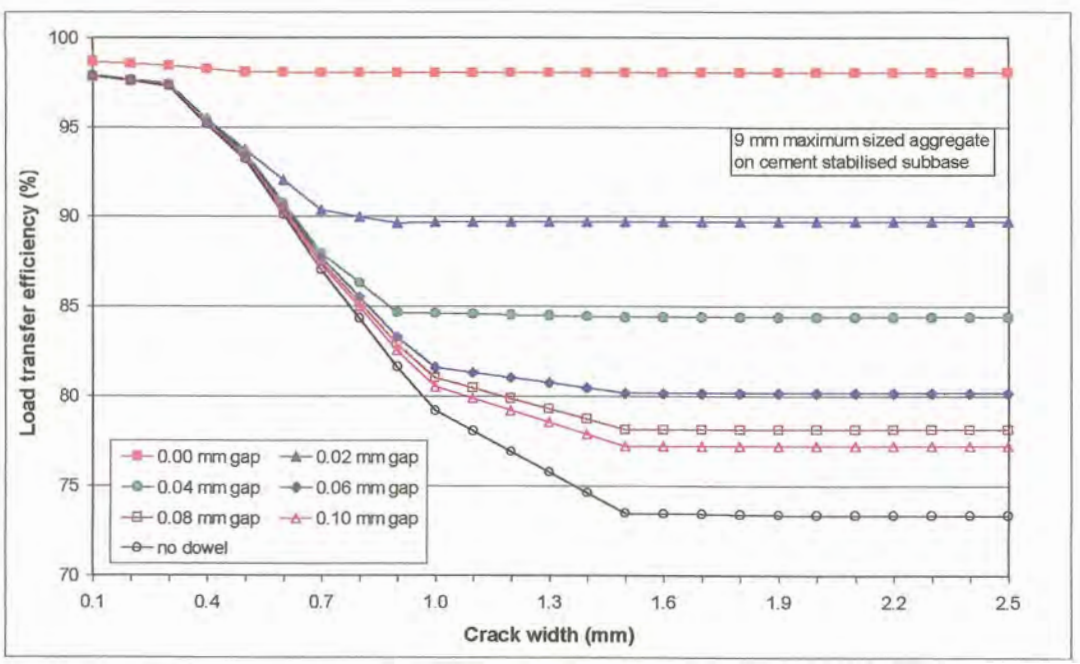

Figure D.64: Deflection load transfer efficiency in the wheel path – 9 mm maximum sized aggregate – combined affect of aggregate interlock and dowels (gap around dowel)

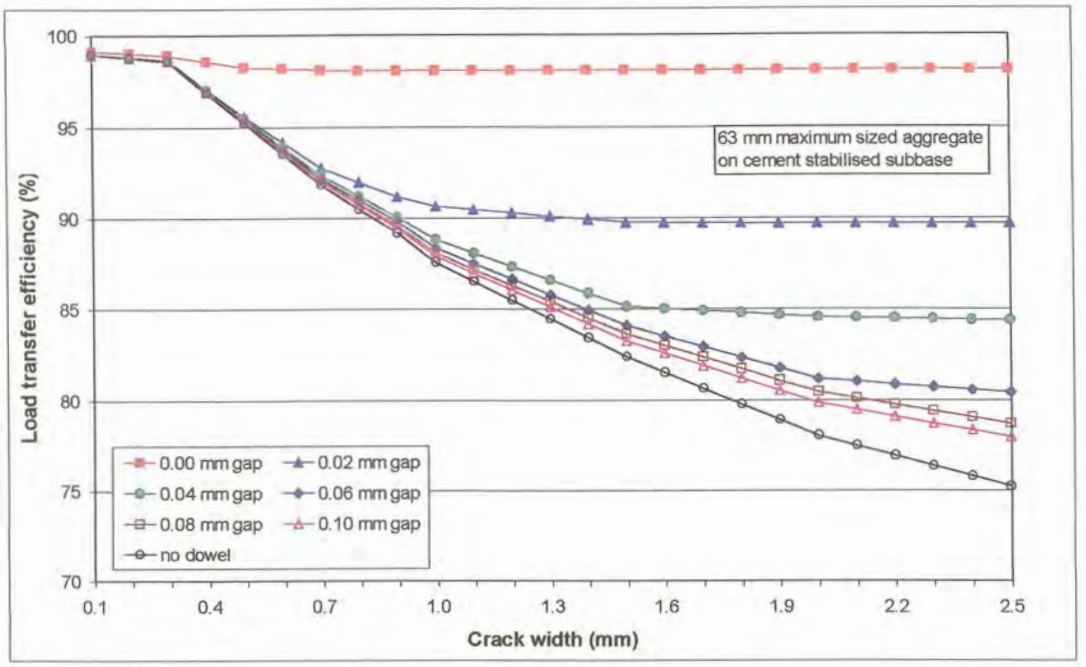

Figure D.65: Deflection load transfer efficiency in the wheel path – 63 mm maximum sized aggregate – combined affect of aggregate interlock and dowels (gap around dowel)

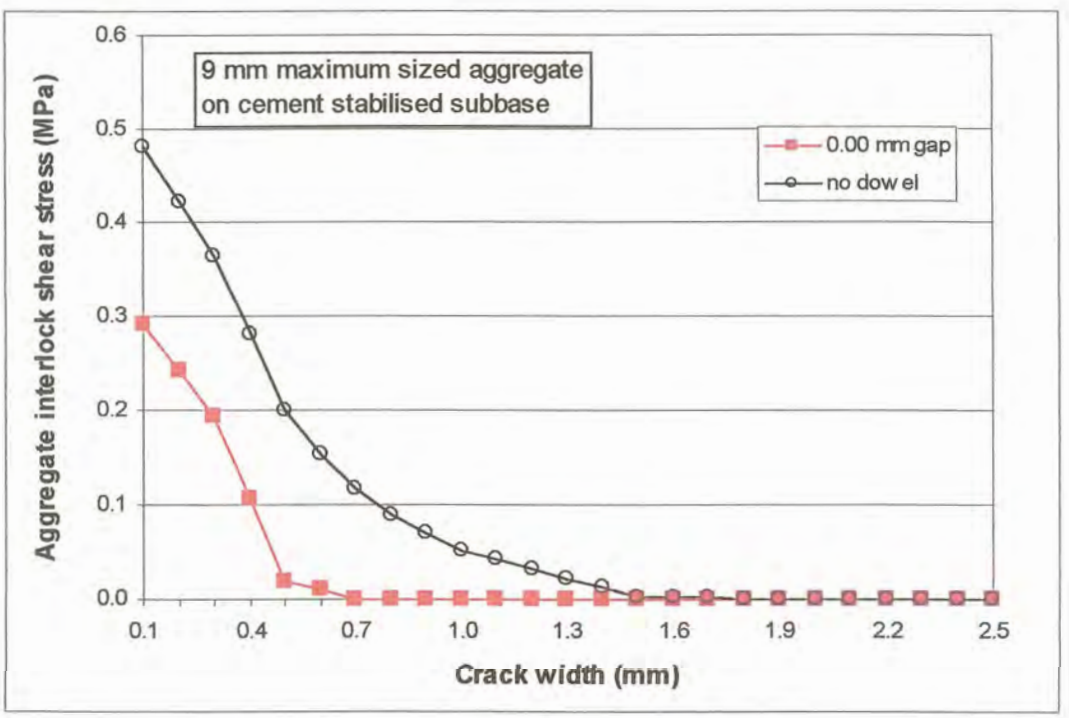

Figure D.66: Maximum aggregate interlock shear stress in the wheelpath – 9 mm maximum sized aggregate – combined affect of aggregate interlock and dowels (gap around dowel)

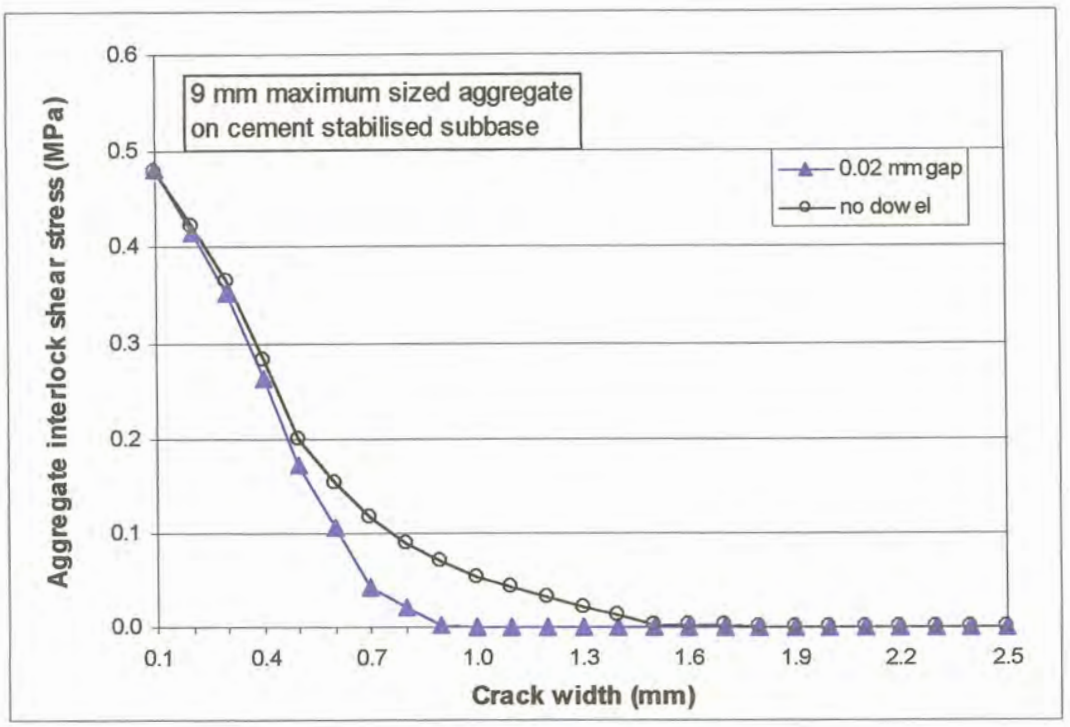

Figure D.67: Maximum aggregate interlock shear stress in the wheelpath – 9 mm maximum sized aggregate – combined affect of aggregate interlock and dowels (gap around dowel)

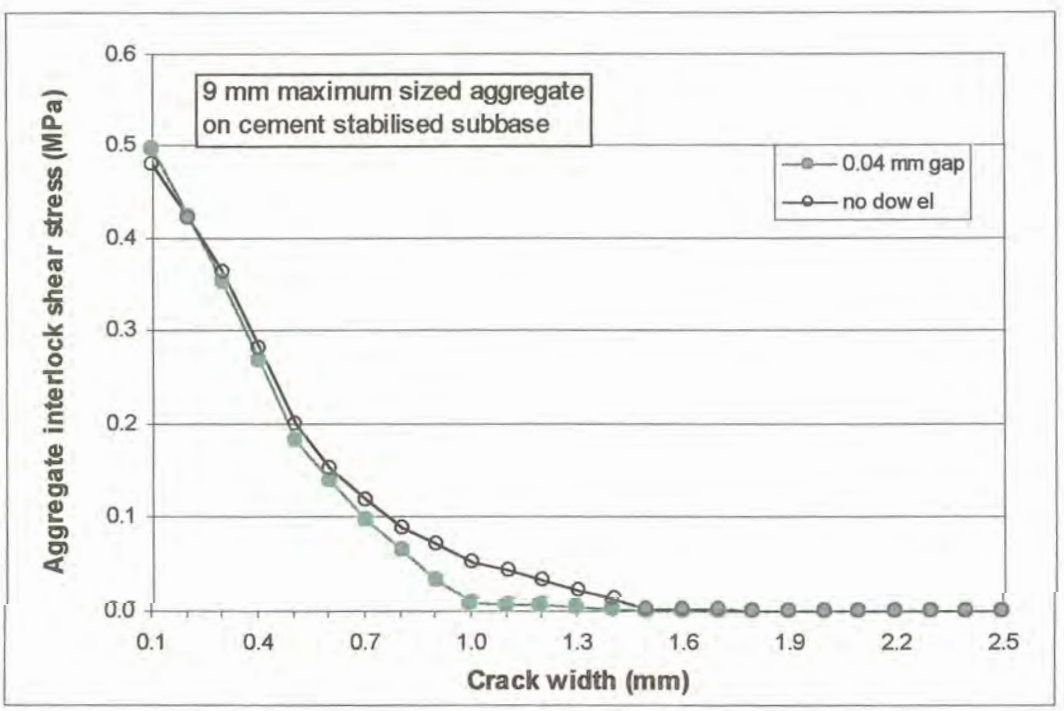

Figure D.68: Maximum aggregate interlock shear stress in the wheelpath – 9 mm maximum sized aggregate – combined affect of aggregate interlock and dowels (gap around dowel)

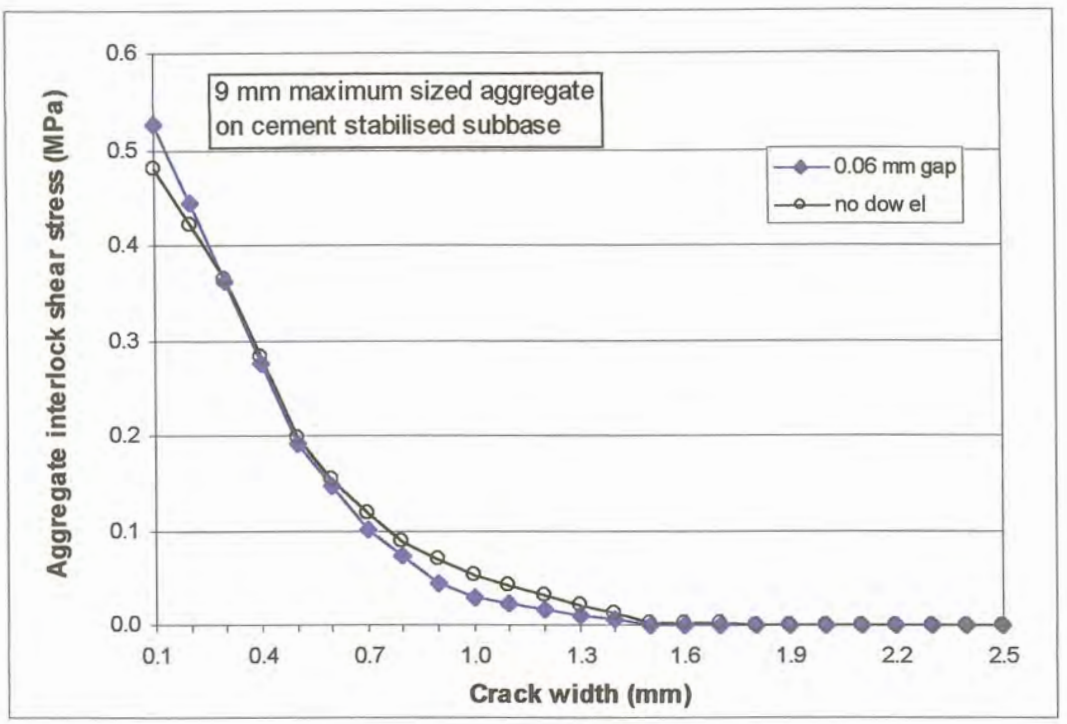

Figure D.69: Maximum aggregate interlock shear stress in the wheelpath – 9 mm maximum sized aggregate – combined affect of aggregate interlock and dowels (gap around dowel)

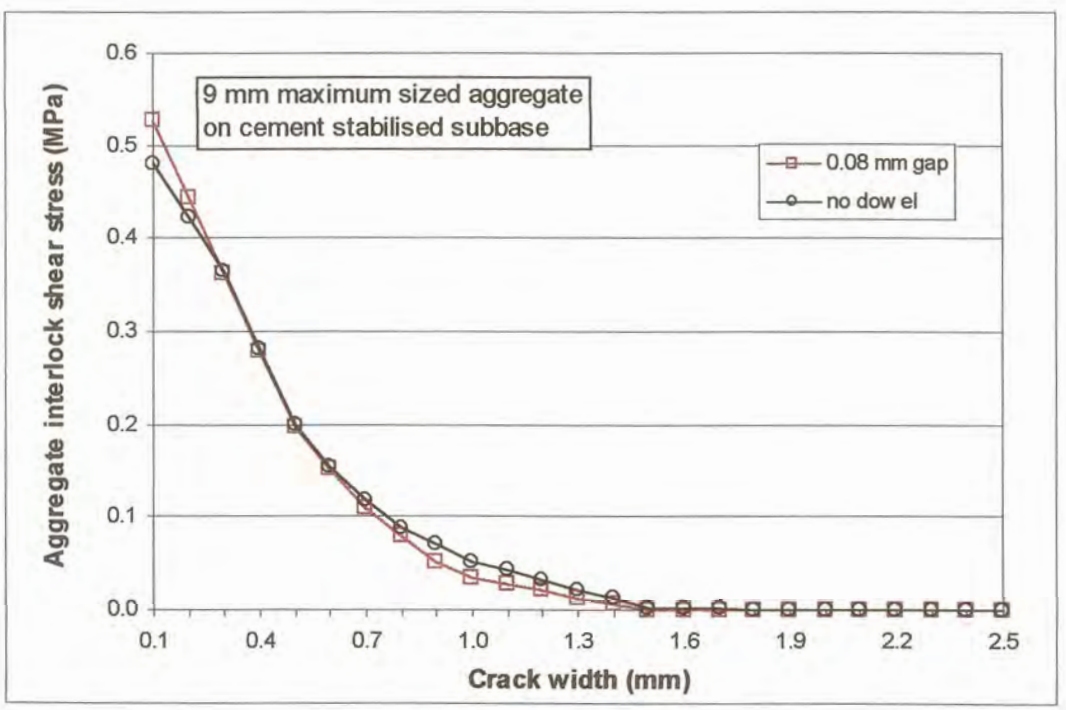

Figure D.70: Maximum aggregate interlock shear stress in the wheelpath – 9 mm maximum sized aggregate – combined affect of aggregate interlock and dowels (gap around dowel)

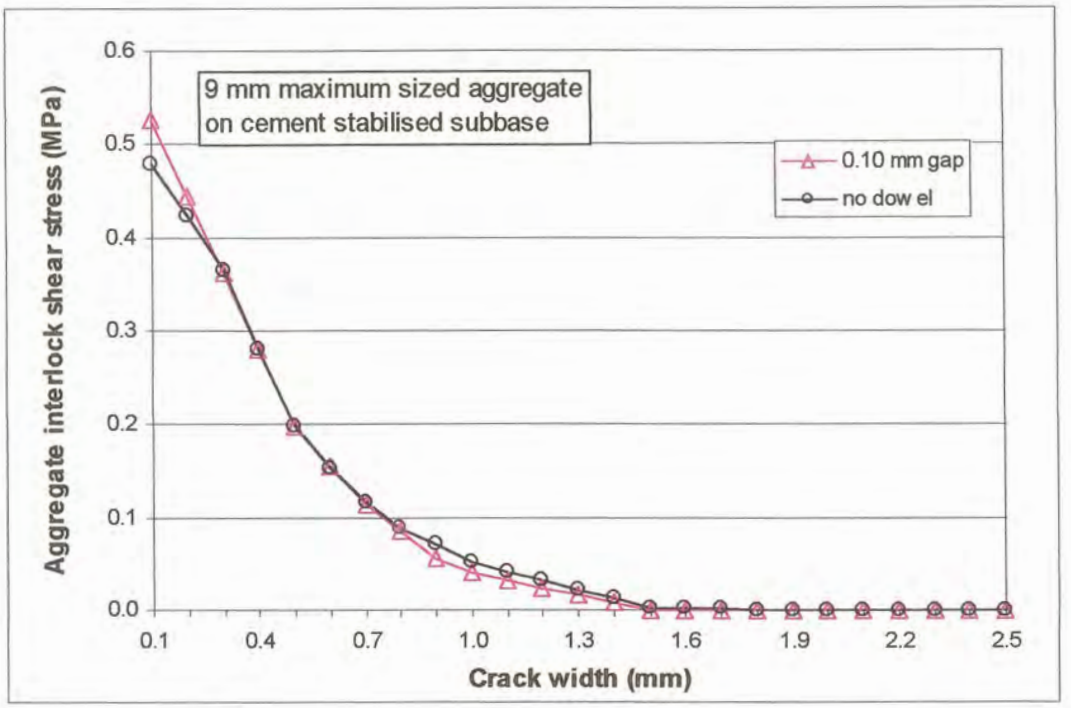

Figure D.71: Maximum aggregate interlock shear stress in the wheelpath – 9 mm maximum sized aggregate – combined affect of aggregate interlock and dowels (gap around dowel)

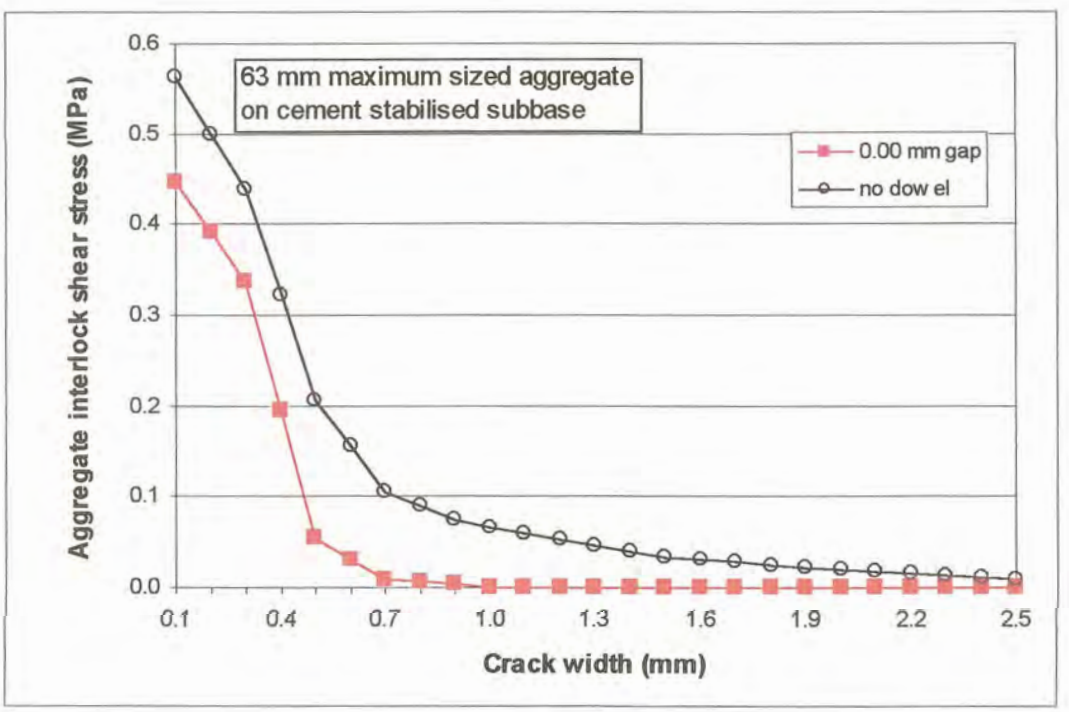

Figure D.72: Maximum aggregate interlock shear stress in the wheelpath – 63 mm maximum sized aggregate – combined affect of aggregate interlock and dowels (gap around dowel)

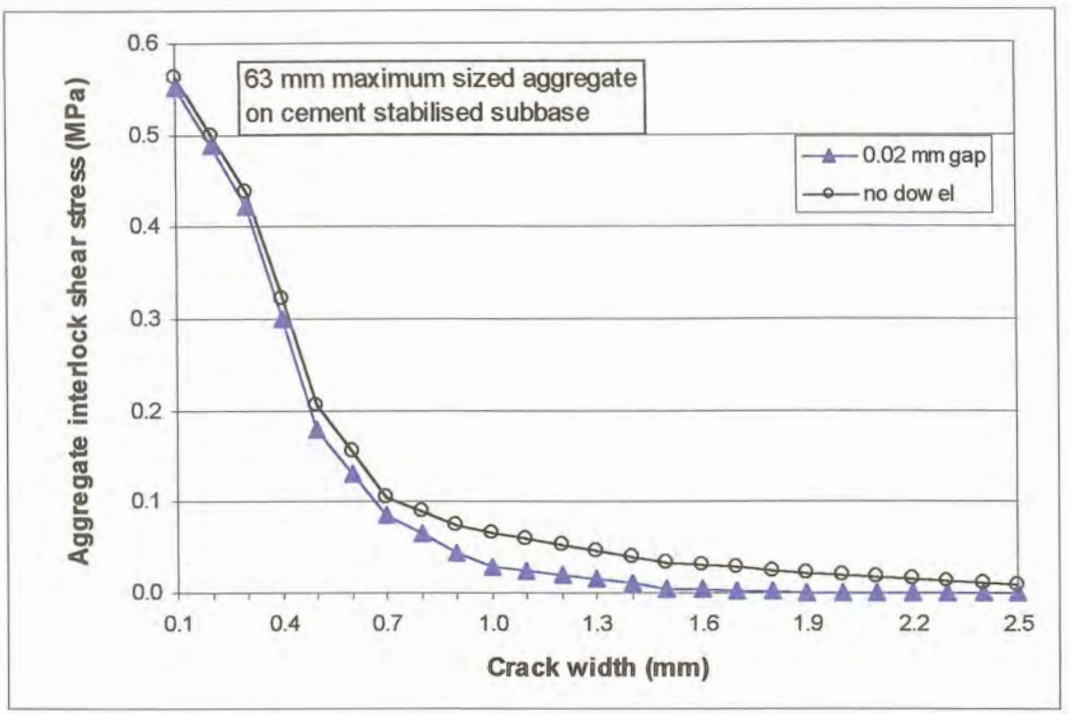

Figure D.73: Maximum aggregate interlock shear stress in the wheelpath – 63 mm maximum sized aggregate – combined affect of aggregate interlock and dowels (gap around dowel)

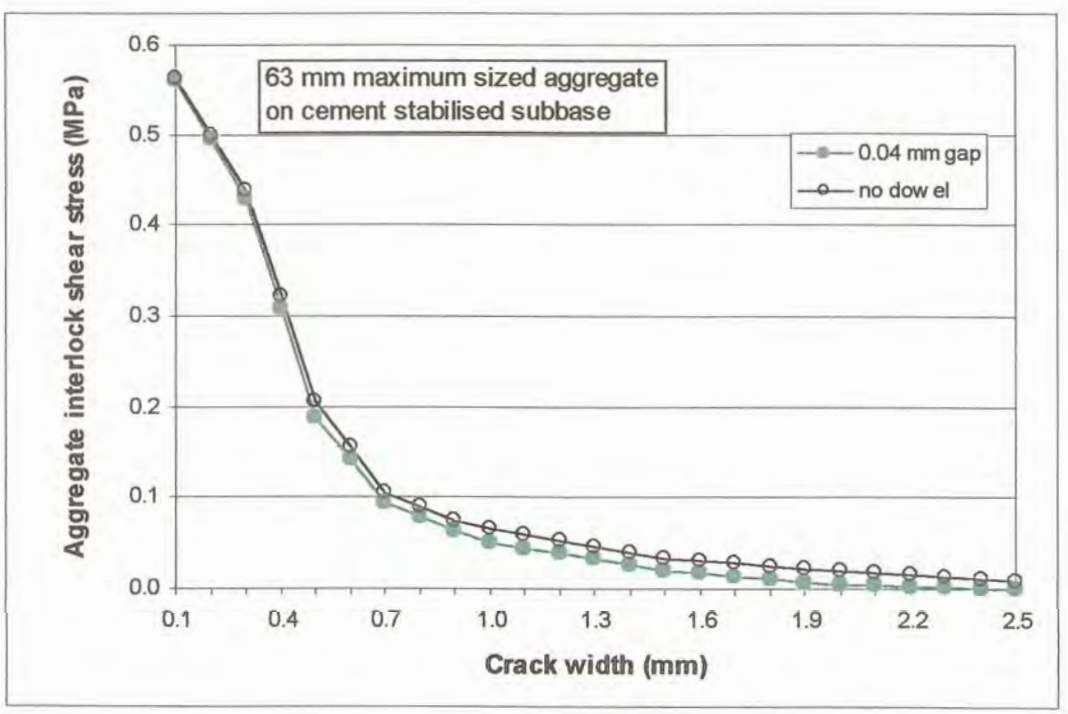

Figure D.74: Maximum aggregate interlock shear stress in the wheelpath – 63 mm maximum sized aggregate – combined affect of aggregate interlock and dowels (gap around dowel)

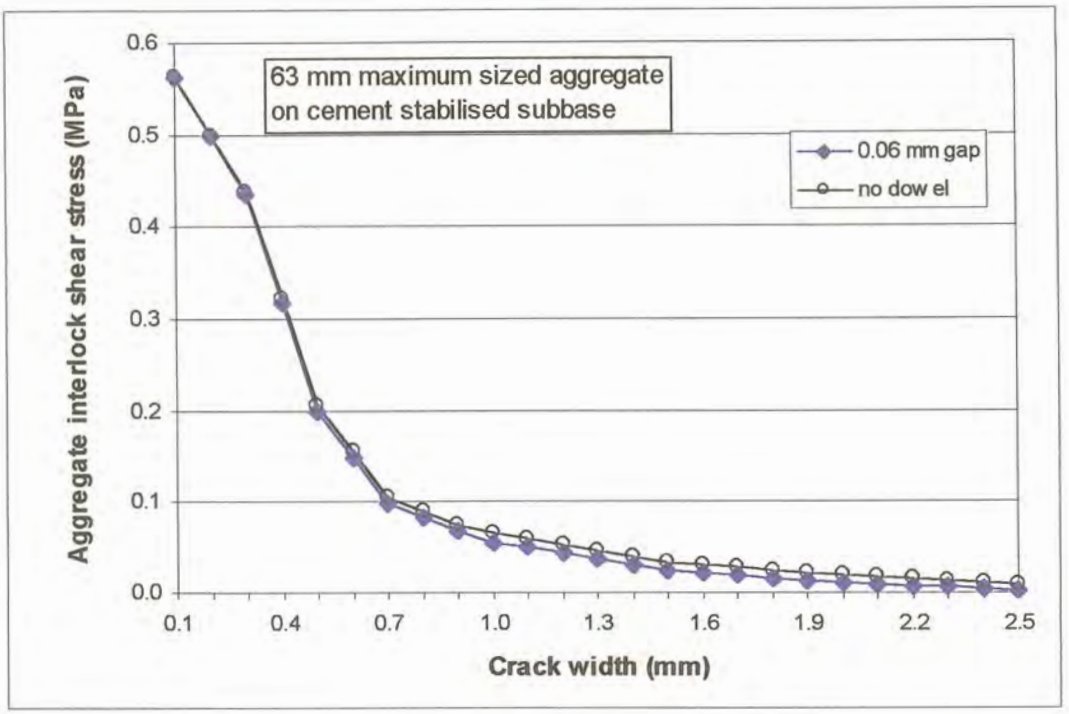

Figure D.75: Maximum aggregate interlock shear stress in the wheelpath – 63 mm maximum sized aggregate – combined affect of aggregate interlock and dowels (gap around dowel)

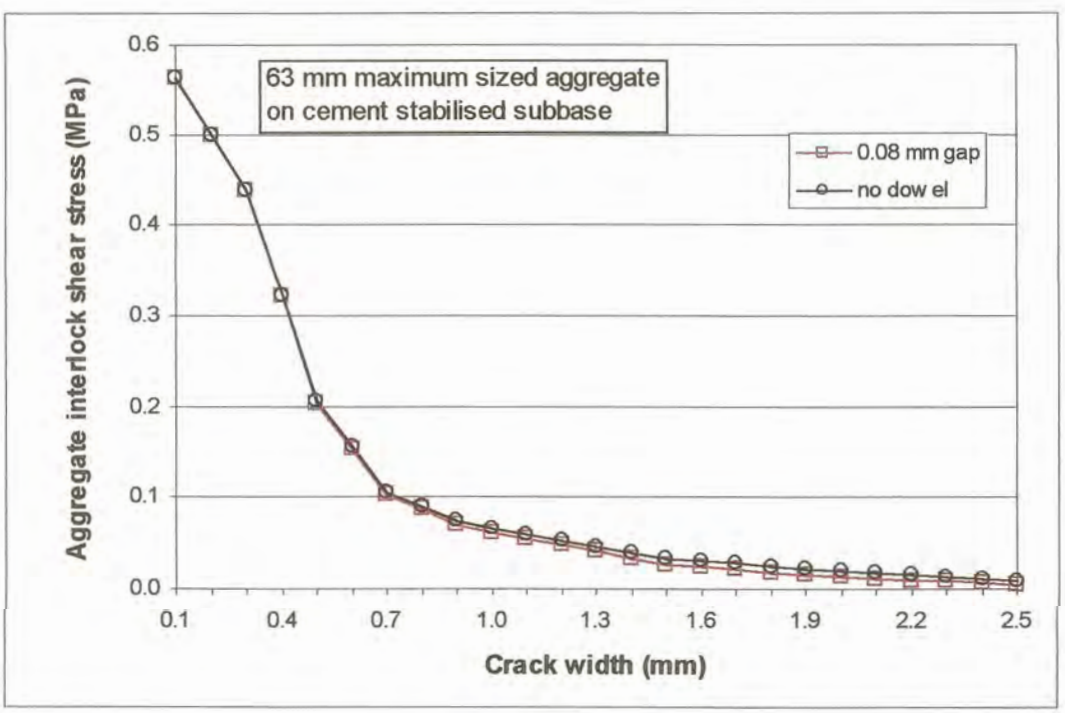

Figure D.76: Maximum aggregate interlock shear stress in the wheelpath – 63 mm maximum sized aggregate – combined affect of aggregate interlock and dowels (gap around dowel)

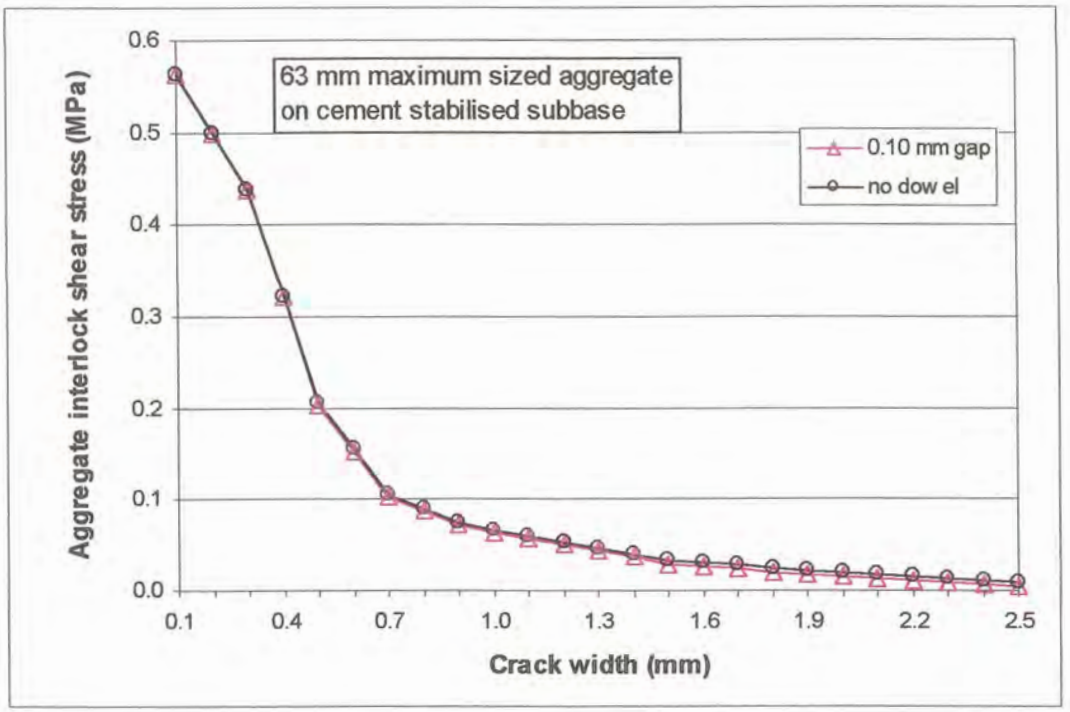

Figure D.77: Maximum aggregate interlock shear stress in the wheelpath – 63 mm maximum sized aggregate – combined affect of aggregate interlock and dowels (gap around dowel)

The development of the total shear force transferred across the joint through both aggregate interlock and dowel action, at increased gap width around the dowel, is presented in Figures D.78 to D.89. As for the deflection load transfer efficiency, as well as the maximum shear stress transferred across the joint in the wheel path, the relationships obtained approximated the "no dowel" case.

Where the total shear force transferred across the joint/crack by both aggregate interlock, and dowel action was calculated, aggregate interlock contributed the major component of the forces transferred at narrow crack widths. The aggregate interlock component then decreased to zero, with the influence of the 9 mm aggregate concrete reaching zero sooner, and at a smaller gap width than the 63 mm aggregate concrete. On the other hand, the dowels initially contributed between 44% and 17% of the force transferred for 9 mm and 63 mm aggregate, respectively at narrow crack and gap widths. The forces transferred through the dowels increased while the forces transferred through aggregate interlock decreased with increasing crack widths, at narrow gap widths. The dowels contributed the major portion of the total shear force transferred at narrow gap widths, but at large crack widths. However, as before, the larger the gap around the dowels, the less the contributions of the dowels in transferring shear forces across the joint/crack. According to these theoretical analyses conducted with EverFE, it seems as if even a relatively small gap width of 0,10 mm around the dowels, renders the dowels ineffective in transferring shear stresses across the joint/crack.

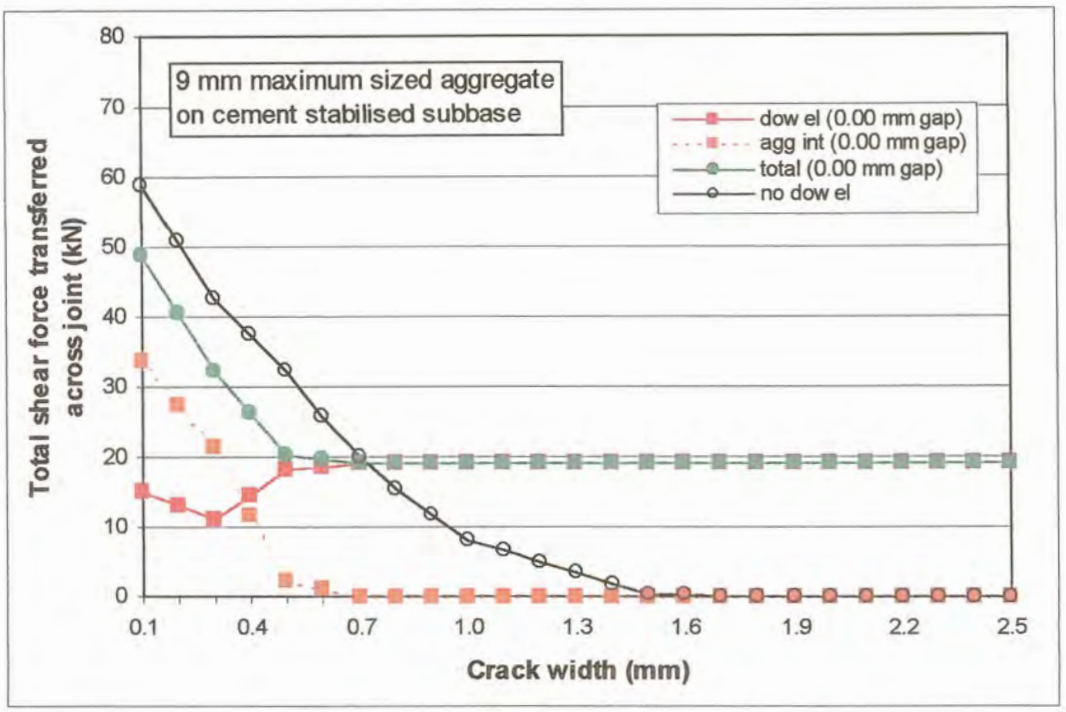

Figure D.78: Total shear force transferred across joint – 9 mm maximum sized aggregate – combined effect of aggregate interlock and dowel action (gap around dowel)

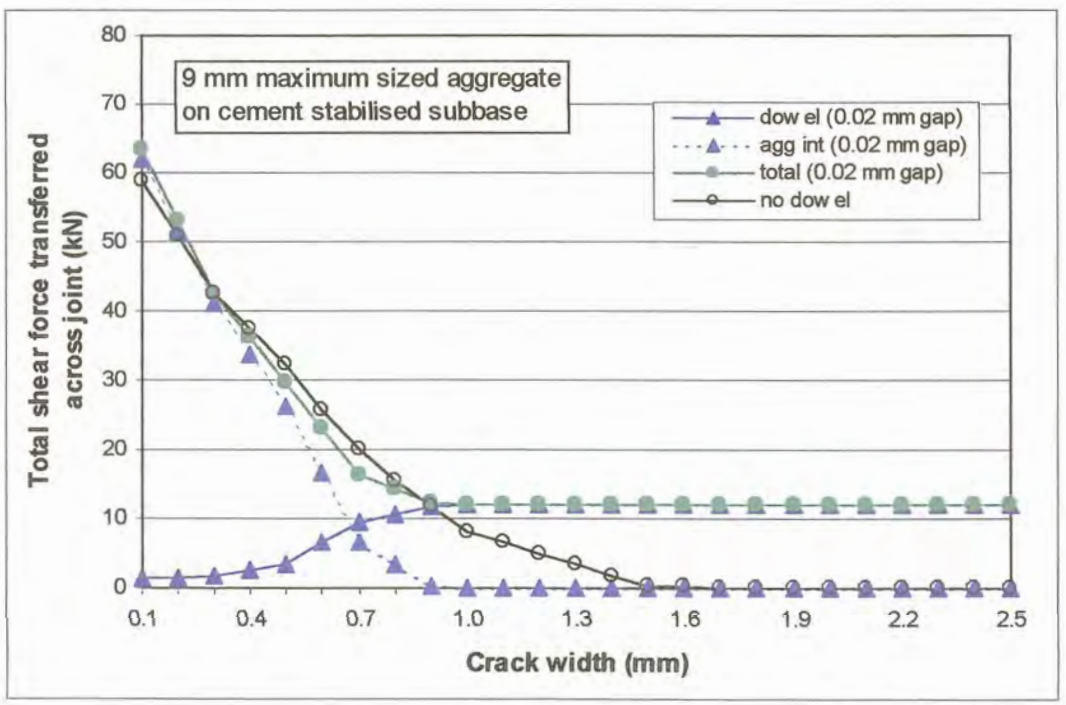

Figure D.79: Total shear force transferred across joint – 9 mm maximum sized aggregate – combined effect of aggregate interlock and dowel action (gap around dowel)

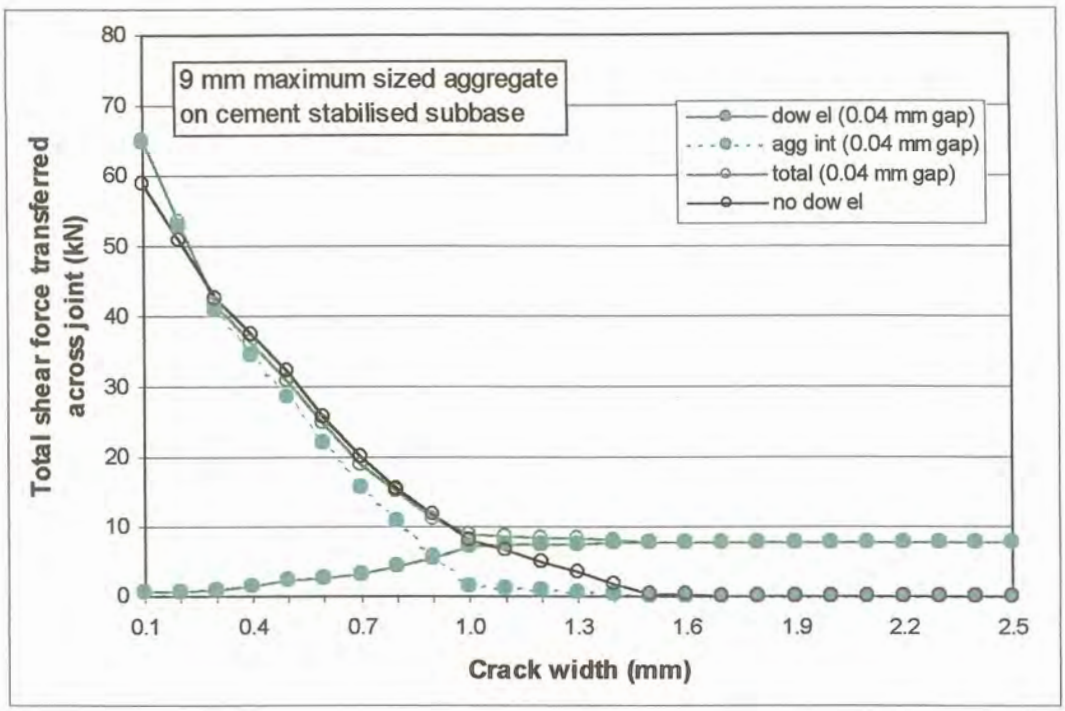

Figure D.80: Total shear force transferred across joint – 9 mm maximum sized aggregate – combined effect of aggregate interlock and dowel action (gap around dowel)

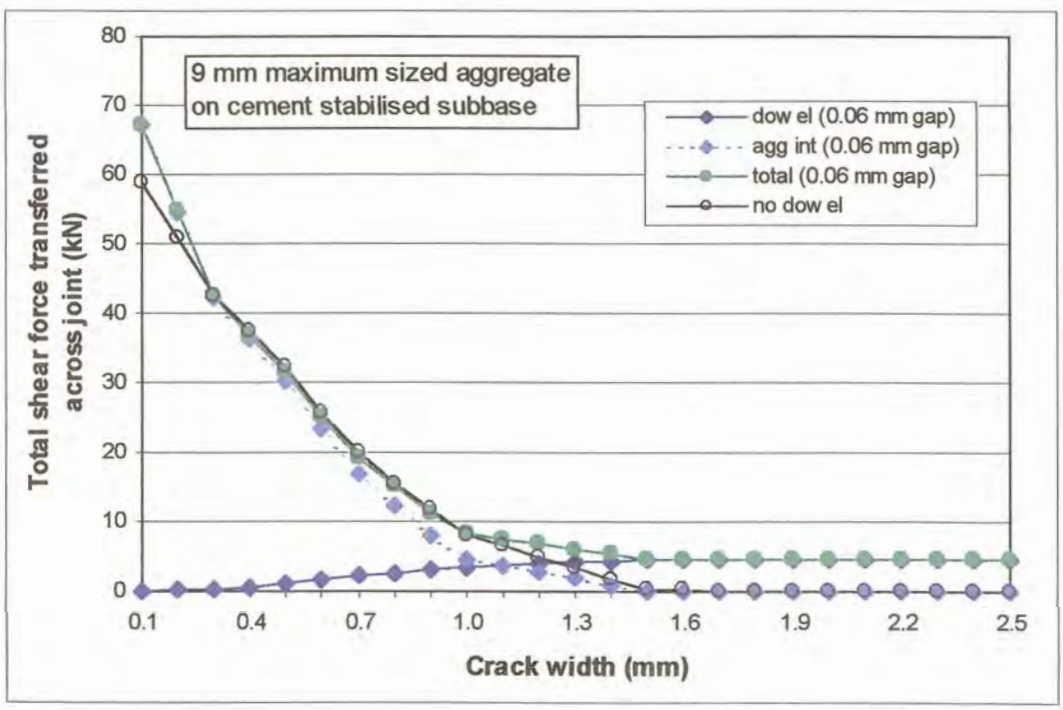

Figure D.81: Total shear force transferred across joint – 9 mm maximum sized aggregate – combined effect of aggregate interlock and dowel action (gap around dowel)

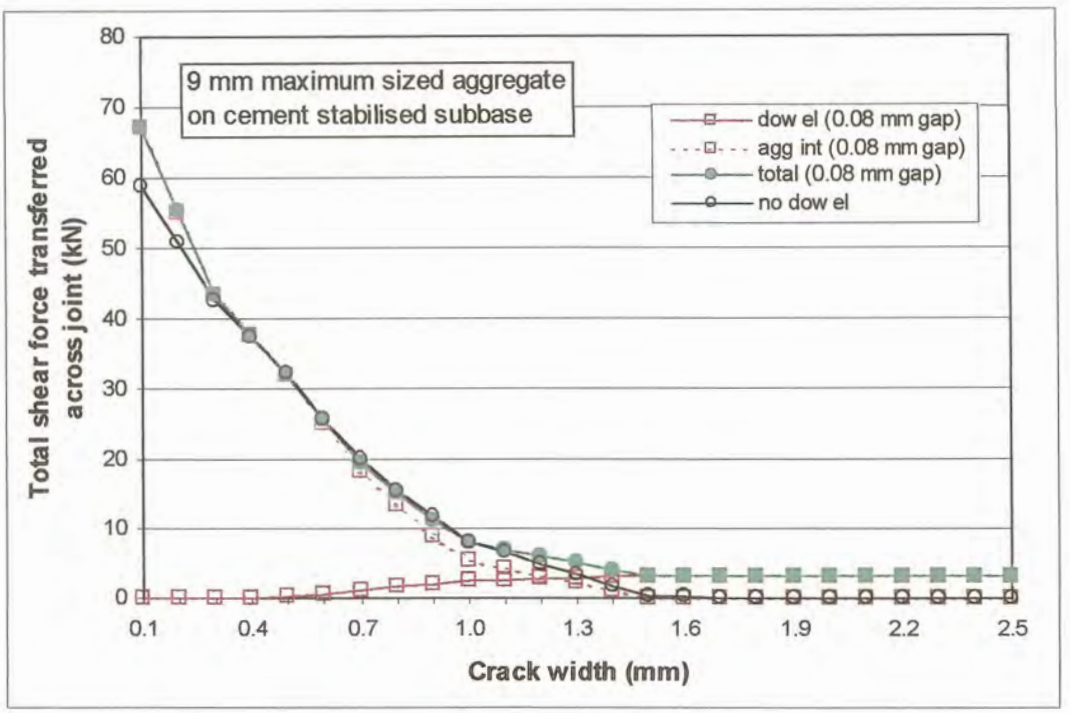

Figure D.82: Total shear force transferred across joint – 9 mm maximum sized aggregate – combined effect of aggregate interlock and dowel action (gap around dowel)

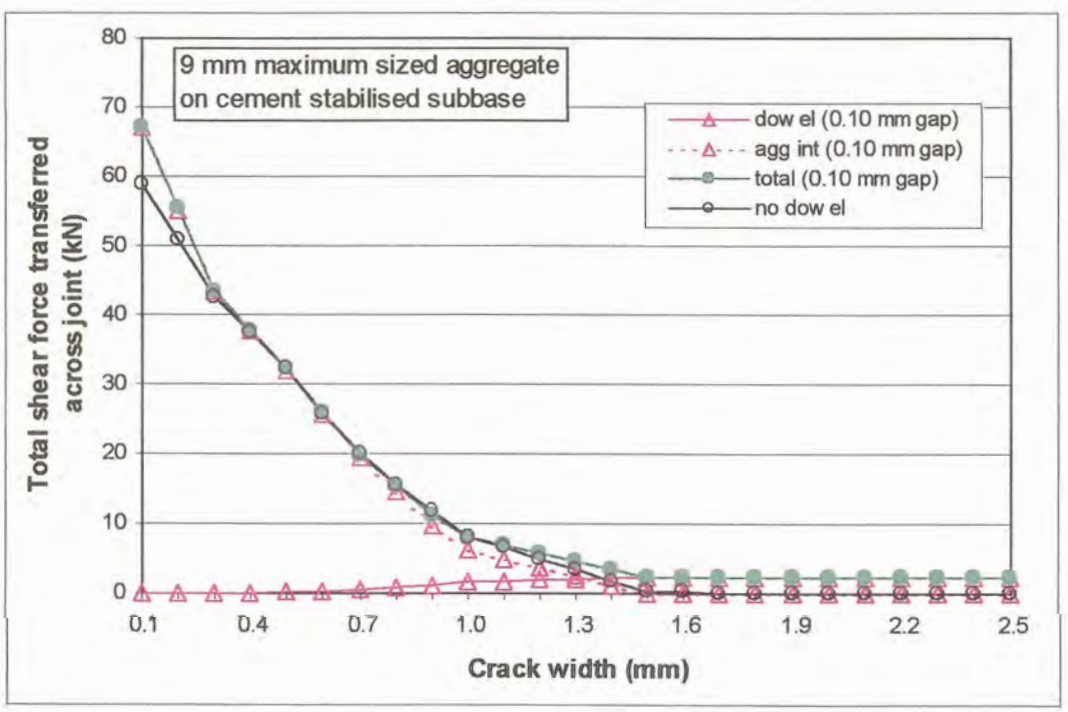

Figure D.83: Total shear force transferred across joint – 9 mm maximum sized aggregate – combined effect of aggregate interlock and dowel action (gap around dowel)

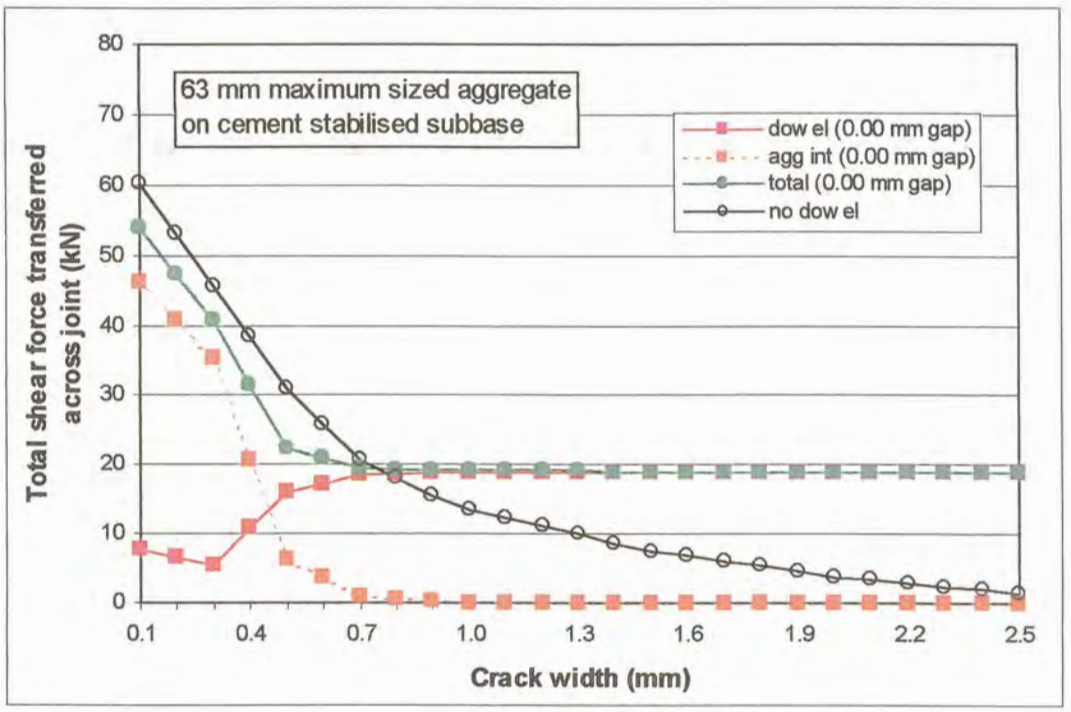

Figure D.84: Total shear force transferred across joint – 63 mm maximum sized aggregate – combined effect of aggregate interlock and dowel action (gap around dowel)

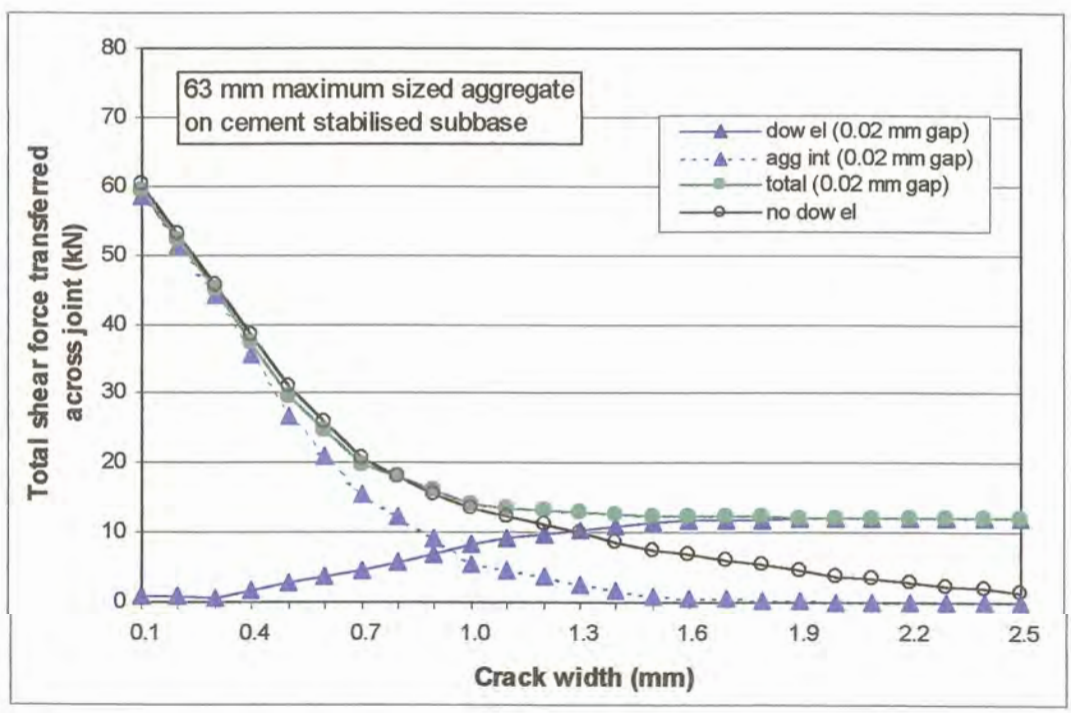

Figure D.85: Total shear force transferred across joint – 63 mm maximum sized aggregate – combined effect of aggregate interlock and dowel action (gap around dowel)

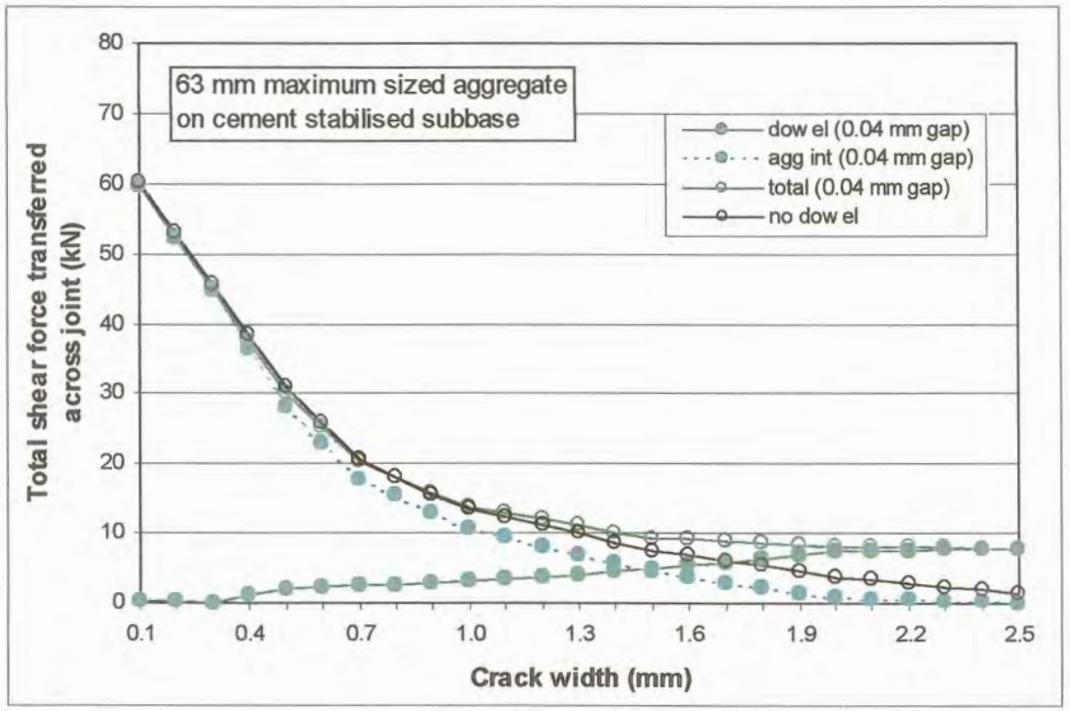

Figure D.86: Total shear force transferred across joint – 63 mm maximum sized aggregate – combined effect of aggregate interlock and dowel action (gap around dowel)

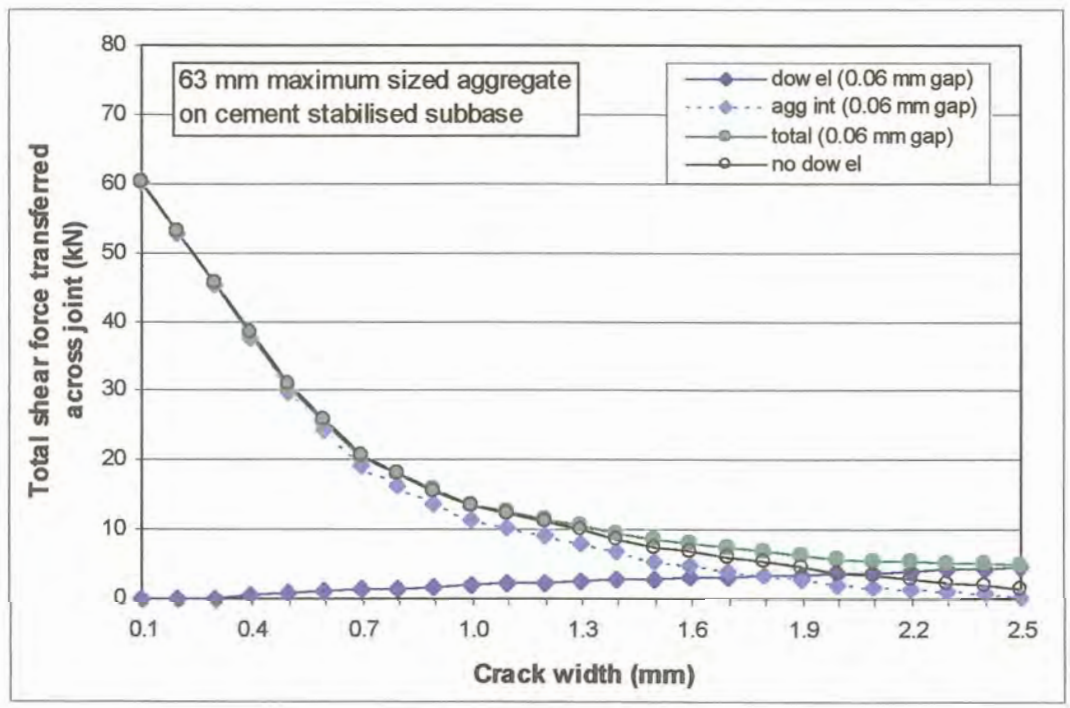

Figure D.87: Total shear force transferred across joint – 63 mm maximum sized aggregate – combined effect of aggregate interlock and dowel action (gap around dowel)

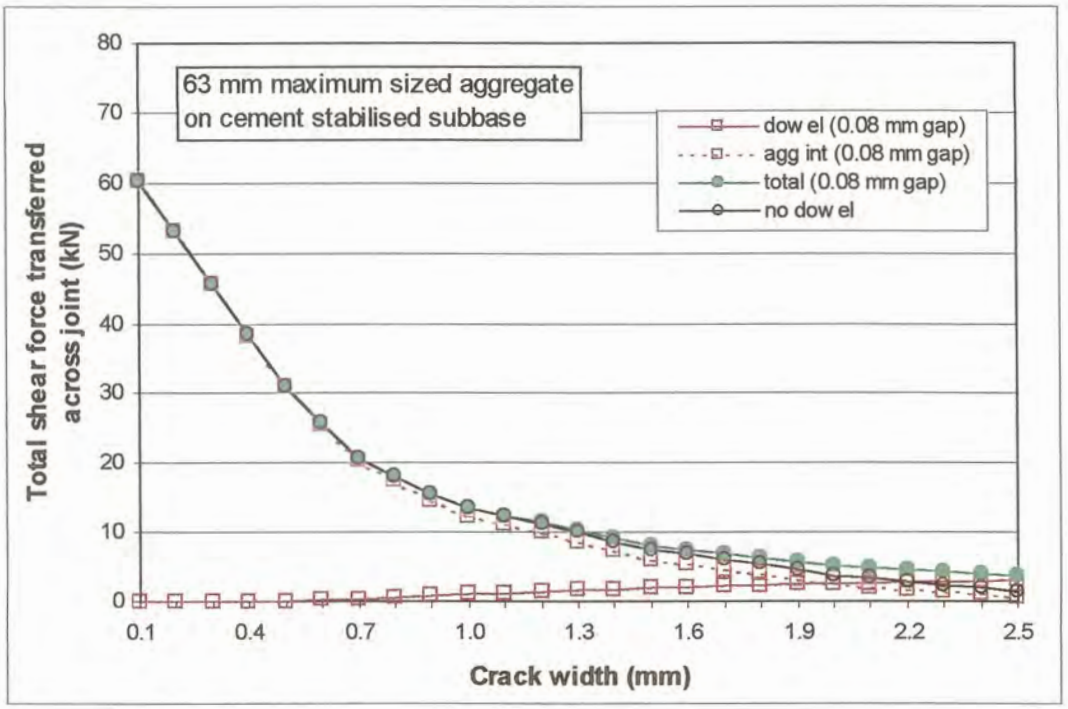

Figure D.88: Total shear force transferred across joint – 63 mm maximum sized aggregate – combined effect of aggregate interlock and dowel action (gap around dowel)

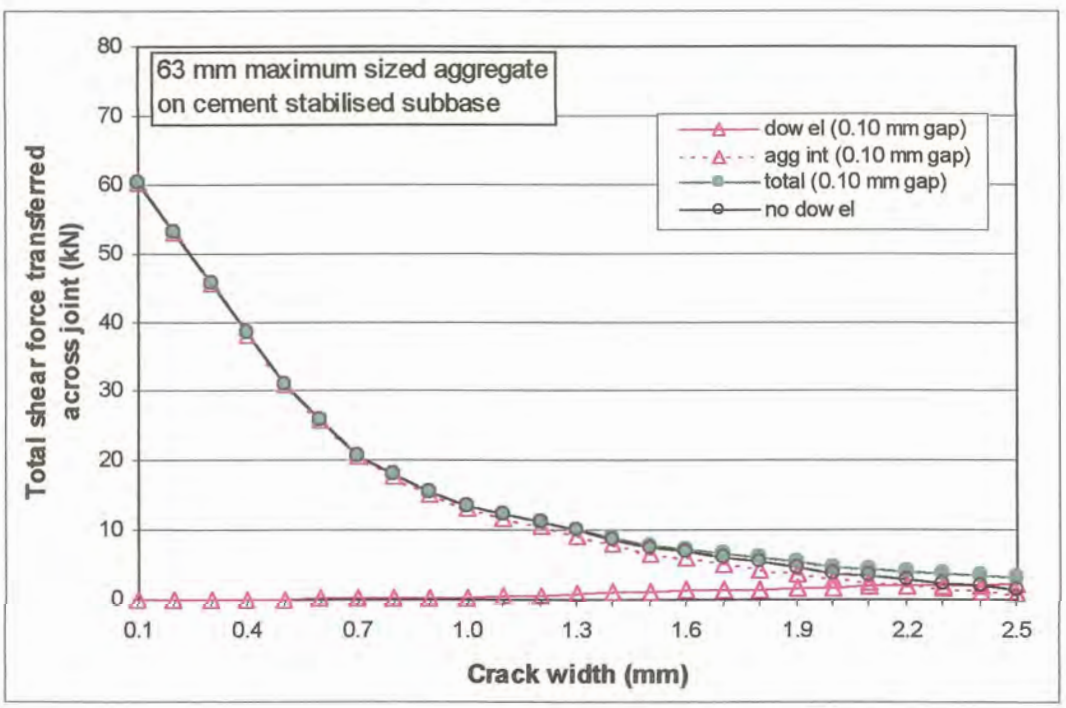

Figure D.89: Total shear force transferred across joint – 63 mm maximum sized aggregate – combined effect of aggregate interlock and dowel action (gap around dowel)

D.6 SUMMARY AND CONCLUSIONS

In order to determine the ranges for the different input variables that could be expected during modelling in the laboratory, theoretical analyses of the envisaged concrete pavement models were first conducted. The 3D FE computer software programme EverFE, specifically developed for the investigation of concrete pavement performance at a joint/crack in the pavement, was used to conduct the theoretical analyses.

The effect of aggregate interlock load transfer efficiency was determined using concrete containing 9 mm, 19 mm, 37,5 mm, and 63 mm maximum aggregate sizes. The effect of dowel looseness was further determined using 16 mm, 25 mm and 32 mm diameter bars (460 mm long) at 300 mm, 450 mm, and 600 mm spacing. Both the aggregate interlock and dowel looseness models were analysed using three different subbases beneath the concrete, namely crushed stone (G1), cement stabilised gravel (C2), and continuously graded asphalt (AC). The natural soil was modelled as an elastic solid foundation using rubber mats with a modulus of 80 MPa/m to simulate a uniform subgrade and provide continuous support.

Generally, the larger the aggregate, the greater the deflection load transfer efficiency calculated, and the stiffer the subbase, the greater the initial shear stresses and shear forces that were transferred across the joint/crack. In most of the aggregate interlock models the values converged at a crack width of about 2,5 mm which was then taken as the maximum crack width for analysis purposes.

During dowel looseness modelling, it was found that the larger the dowel bar diameter, the greater the deflection load transfer efficiency for the same dowel bar spacing. The initial shear force carried in the dowels at a zero gap width around the dowel was the least for the model supported on a cement stabilised subbase. This indicated that the stronger subbase support reduced the shear forces experienced in the dowel bars. The values converged at a gap width around the dowels of about 0,10 mm, which was then taken as the maximum for analysis purposes.

The combined effect of aggregate interlock and dowels was also investigated theoretically. The same model as the one used in aggregate interlock modelling (par. 7.2.1) with a cement stabilised subbase was used. To determine the effect of dowels in the model, 16 mm diameter dowels at 300 mm spacing were placed across the joint. For the first set of combined models, the crack width was varied, while the gap around the dowel was kept constant, and for the second set of combined models, both the crack width and the gap around the dowels were varied.

The combined deflection load transfer efficiency of aggregate interlock and dowels with no gap around the dowels was far greater than for aggregate interlock only. This efficiency, however, decreased gradually with increasing gap width around the dowel, and closely approximated the aggregate

interlock (no dowel) efficiency at a gap width of 0,10 mm. The maximum shear stress measured in the wheel path, as well as the total shear force transferred across the joint/crack, was initially less than the "no dowel" situation, but also approximated the values obtained for the "no dowel" case at a gap width of 0,10 mm.

According to the theoretical analyses conducted with EverFE, it seems as if even a relatively small gap width of 0,10 mm around the dowels, rendered the dowels ineffective in transferring shear stresses across the joint. The shear stress transferred across a joint through the dowels in a doweled joint, but with a gap around the dowels was therefore found to be equivalent to the stress transferred due to aggregate interlock only in an un-doweled joint.

The results of the analyses conducted, implied that the ultimate function of dowels are to prevent joint faulting, because as soon as a gap has developed around the dowel, the shear stress transfer efficiency through the dowels became negligible. This confirmed the conclusions already reached by inter alia Buch and Zollinger (1996) and Sargand (1999) who recognised the reduced effectiveness of dowel bars with an increase in dowel looseness, due to repeated applications of high bearing stresses during the life of the pavement.